AD-A260 724

2

Adaptive Liquid Crystal TV Based Joint Transform Correlator as Applied to Real-Time Pattern Recognition

Final Report

By:

F.T.S. Yu
Principal Investigator

Department of Electrical and Computer Engineering
The Pennsylvania State University
University Park, PA 16802

Prepared for:

Army Research Office
P.O. Box 12211
Research Triangle Park, NC 27709-2211

Attention: John S. Kruger

ARO Proposal Number 28502-PH

Period Covered: April 15, 1991 to December 14, 1992

Date: January 5, 1992

DISTRIBUTION STATEMENT A
Approved for public release;
Distribution Unlimited

93-03127

1728

93

MASTER COPY KEEP THIS COPY FOR REPRODUCTION PURPOSES

REPORT DOCUMENTATION PAGE

Form Approved
OMB No. 0704-0188

1. AGENCY USE ONLY *(Leave blank)*

2. REPORT DATE
January 5, 1993

3. REPORT TYPE AND DATES COVERED
Final Report - 4/15/91 - 12/14/92

4. TITLE AND SUBTITLE
Adaptive Liquid Crystal TV Based Joint Transform
Correlator as Applied to Real-Tim Pattern Recognition

5. FUNDING NUMBERS
DAAL03-91-G-0112

6. AUTHOR(S)
Francis T.S. Yu

7. PERFORMING ORGANIZATION NAME(S) AND ADDRESS(ES)
Department of Electrical and Computer Engineering
The Pennsylvania State University
University Park, PA 16802

8. PERFORMING ORGANIZATION REPORT NUMBER
NA

9. SPONSORING/MONITORING AGENCY NAME(S) AND ADDRESS(ES)
U. S. Army Research Office
P. O. Box 12211
Research Triangle Park, NC 27709-2211

10. SPONSORING/MONITORING AGENCY REPORT NUMBER
ARO 28502.1-PH

11. SUPPLEMENTARY NOTES
The view, opinions and/or findings contained in this report are those of the author(s) and should not be construed as an official Department of the Army position, policy, or decision, unless so designated by other documentation.

12a. DISTRIBUTION/AVAILABILITY STATEMENT
Approved for public release; distribution unlimited.

12b. DISTRIBUTION CODE

13. ABSTRACT *(Maximum 200 words)*

The primary goal of this research is to study a programmable joint-transform correlator (JTC) using liquid crystal television (LCTV) panels for adaptive real-time pattern recognition applications. The technique can improve the pattern recognition and identification technology that is of interest to the U.S. Army. The technique we studied is a real-time programmable electro-optical architecture. There are several reasons for selecting the optical technique over their digital and electronic counterparts, as follows: Optical technique is capable of handling a large space-bandwidth image; optical technique is capable of performing parallel operations; optics can perform massive interconnections; optical transformation can be operated at high speed, etc. By using the LCTV, the pattern under observation can be correlated with a large number of recallable image memories. In addition, the LCTV technique is rather simple and economical to operate. The LCTV-optical correlator, in principle, can be designed into a compact portable form for insitu application. Brief outlines of the major research findings and publications are provided in this report.

14. SUBJECT TERMS
Joint transform correlator, liquid crystal television correlator, optical pattern recognition

15. NUMBER OF PAGES
171

16. PRICE CODE

17. SECURITY CLASSIFICATION OF REPORT	**18. SECURITY CLASSIFICATION OF THIS PAGE**	**19. SECURITY CLASSIFICATION OF ABSTRACT**	**20. LIMITATION OF ABSTRACT**
UNCLASSIFIED	UNCLASSIFIED	UNCLASSIFIED	UL

28502-PH

FINAL REPORT

1. ARO PROPOSAL NUMBER: 28502-PH
2. PERIOD COVERED BY REPORT: April 15, 1991 - December 14, 1992
3. TITLE OF PROPOSAL: Adaptive Liquid Crystal TV Based Joint Transform Correlator as Applied to Real-Time Pattern Recognition
4. CONTRACT OR GRANT NUMBER: DAAL03-91-0012
5. NAME OF INSTITUTION: The Pennsylvania State University
6. AUTHORS OF REPORT: Francis T.S. Yu

CONTENTS Page

10. APPENDIX: Publications

7. LIST OF MANUSCRIPTS SUBMITTED OR PUBLISHED UNDER ARO SPONSORSHIP DURING THIS REPORTING PERIOD, INCLUDING JOURNAL REFERENCES:

F.T.S. Yu, T. Lu and X. Yang, "Optical Implementation of Hetero-Association Neural Network with Inter-Pattern Association Model," International Journal of Optical Computing, Vol. 1, pp. 129-140, December 1990.

F.T.S. Yu, S. Wu, A. Mayers, S. Rajan and D. A. Gregory, "Color Holographic Storage in $LiNbO_3$," Optics Communications, Vol. 81, pp. 348-352, March 1991.

F.T.S. Yu, S. Wu, A. Mayers, S. Rajan, "Wavelength Multiplexed Reflection Matched Spatial Filters using $LiNbO_3$," Optics Communications, Vol. 81, pp. 343-347, March 1991.

X. Yang, T. Lu, F.T.S. Yu, and D. A. Gregory, "Redundant Interconnection Interpattern Association Neural Network," Applied Optics, Vol. 30, pp. 5182-5187, December 1991.

F.T.S. Yu, "Optical Neural Networks: Architecture, Design and Models," Proceedings of SPIE on Wave Propagation and Scattering in Varied Media II," Vol. 1558, pp. 390-405, July 1991, keynote speaker.

F.T.S. Yu, X. Yang and Don A. Gregory, "Polychromatic Neural Network," Proceedings of SPIE on Wave Propagation and Scattering in Varied Media II, Vol. 1558, pp. 450-458, July 1991.

F.T.S. Yu, S. Wu, X. Y. Yang, S. Jutamulia and G. M. Storti, "Optical Neural Network using Novel Electron Trapping Materials," Optical Memory and Neural Networks, Vol. 1, pp. 49-54, July 1992.

F.T.S. Yu, S. Wu, S. Rajan, A. Mayers and D. A. Gregory, "Optical Novelty Filtering using Phase Carrier Frequency," Optics Communications, Vol. 92, pp. 205-208, September 1992.

F.T.S. Yu and X. Yang, "Polychromatic Optical Neuro-Computing," Proceedings of the Soviet-Chinese Joint Seminar on Holography and Optical Information Processing," pp. 19-21, Bishkek, Kirghizstan, USSR, September 21-25, 1991 (invited).

F.T.S. Yu, "Optical Neuro-Computing," Proceedings of AIAA Computing in Aerospace 8, Vol. II, pp. 489-495, Baltimore, MD, October 21-24, 1991.

F.T.S. Yu, "Optical Neural Network: Architecture, Design and Models," Proceedings of Intelligent Engineering Systems through Artificial Neural Networks, pp. 5-10, ASME Press, November 1991.

S. Wu, S. Yin and F.T.S. Yu, "Sensing with Fiber Speckle Holograms," Applied Optics, Vol. 30, pp. 4468-4470, November 1991.

F.T.S. Yu, X. Yin and D. A. Gregory, "Mirror-array Optical Interconnected Neural Network," Optics Letters, Vol. 16, pp. 1602-1604, October 1991.

F.T.S. Yu, Y. Li, X. Yang, T. Lu and D. A. Gregory, "Application of Moment Invariant Pattern Recognition to Optical Neural Net," Optik, Vol. 89, pp. 55-58, December 1991.

F.T.S. Yu, X. Yang and D. A. Gregory, "Polychromatic Neural Network," Optics Communications, Vol. 88, pp. 81-86, March 1992.

F.T.S. Yu, S. Wu, S. Rajan, and D. A. Gregory, "Compact Joint Transform Correlator using a Thick Photorefractive Crystal," Applied Optics, Vol. 31, pp. 2416-2418, May 1992.

X. Yang and F.T.S. Yu, "Optical Implementation of a Hemming Net," Applied Optics,Vol. 31, pp. 3999-4003, July 1992.

A. Tanone, C. M. Uang, F.T.S. Yu, E. C. Tam, and D. A. Gregory, "Effects of Thresholding in Joint Transform Correlation," Applied Optics, Vol. 31, pp. 4816-4822, August 1992.

F.T.S. Yu, X. Yang, and D. A. Gregory, "Polychromatic Neuro-Computing," Proceedings of the Topical Meeting on Optical Computing, SPIE, Vol. 1806, June 1992.

F.T.S. Yu, X. Yang, and D. A. Gregory, "Polychromatic Neuro-Computing," Proceedings on the ICO International Topical Meeting on Optical Computing, June 29-July 1, 1992, Minsk, Republic of Belarus.

F.T.S. Yu, C. M. Uang, and X. Yang, "Exemplar-based Optical Neural Net Classifier for Color Pattern Recognition," Proceedings of the SPIE Conference on Computers, Communications, and Control, Vol. 1812, December 1992.

K. Matsushita, C. Uang, W. Reeser and F.T.S. Yu, "Multicolor Neural Network using Cascaded Color LCTVs," Proceedings of the SPIE Conference on Computers, Communications, and Control, Vol. 1812, December 1992.

C. Uang, and F.T.S. Yu, "Application of Interpattern Association (IPA) to Gray-Level Neural Net," Proceedings of the SPIE Conference on Computers, Communications, and Control, Vol. 1812, December 1992.

F.T.S. Yu, C. M. Uang, and S. Yin, "Gray Level Discrete Associative Memory (GLDAM)," Applied Optics (In Press).

K. Matsushita, Y. Kajiki, Shimizu, and F.T.S. Yu, "Optical Symbolic Substitution using Lenslet Arrays," Optical Engineering (In Press).

F. Cheng, P. Andres, F.T.S. Yu, and D. A. Gregory, "Intensity Compensation Filter for Joint Transform Correlation Peak Enhancement," Applied Optics (In Press).

A. Tanone, Z. Zhang, C. M. Uang, F.T.S. Yu, and D. A. Gregory, "Phase Modulation Depth for Real-Time Kinoform Using Liquid Crystal Television," Optical Engineering (In Press).

D. A. Gregory, J. C. Kirsch, A. Tanone, S. Yin, P. Andres, F.T.S. Yu, and E. C. Tam, "Analysis of Phase Modulation in an LCTV Based Joint Transform Correlator," submitted to Microwave and Optical Technology Letters.

A. Tanone, Z. Zhang, C. M. Uang, F.T.S. Yu, and D. A. Gregory, "An Optical Beam Steering Device using a Liquid Crystal Television Panel," Applied Optics (In Press).

8. SCIENTIFIC PERSONNEL SUPPORTED BY THIS PROJECT AND DEGREES AWARDED DURING THIS REPORTING PERIOD:

8.1 Scientific Personnel

F.T.S. Yu - Principal Investigator
A. Mayers - Research Assistant
F. Hsu - Research Assistant
S. Yin - Research Assistant
F. Cheng - Research Assistant
A. Tanone - Research Assistant
Z. Zhang - Research Assistant
S. Rajan - Research Assistant
C. M. Uang- Research Assistant

8.2 Degrees Awarded

"Study of Phase Modulation Properties of Twisted-Nematic Liquid Crystal Television, as Applied to Computer Generated Holograms and Signal Processing," Aris Tanone, Ph.D. degree, completed in August 1992.

"Optical Disk-Based Joint Transform Correlators: Systems Analysis and Design," Fu Kuo Hsu, Ph.D., completed in August 1992.

9. BRIEF OUTLINE OF RESEARCH FINDINGS

In a conventional coherent optical signal processor [1], the processing operation is usually carried out at the spatial frequency or Fourier plane with a complex spatial filter [2]. This type of coherent optical processor offers a myriad of complicated processing operations [3]. Its success is primarily due to the profound diffraction phenomena. However, complex signal processing can also be achieved by the spatial impulse response using a joint transform processor. There are several inherent advantages of using the joint Fourier transform processor as compared with the conventional coherent processor: (1) spatial filter adjustment is not imposed; (2) a higher input space-bandwidth product; (3) generally, a higher modulation index of the joint transform hologram; (4) lower spatial carrier frequency, etc. In view of these advantages, a joint transform processor, in principle, is capable of performing optical signal processing more efficiently, particularly in the application of real-time pattern recognition. The purpose of this research program is to investigate an adaptive liquid crystal TV based correlator as applied to real-time pattern recognition and tracking.

In this period, from April 15, 1991 to December 14, 1992, we have accomplished several major tasks on the research of real-time pattern recognition with an LCTV based correlator for which various results have been reported in the refereed journals and conference proceedings; with the approval of the Department of the U.S. Army. Sample copies of these publications are included in this final technique report in the subsequent sections, to provide a concise documentation of our findings. In the following sections, we shall give an overview of our research work done during this program. We will highlight some of the accomplished works. A list of publications resulting from this support has been cited in the preceding section.

9.1 LCTV Hybrid Modulating Properties (Appendix 10.1)

During this research program, we have successfully investigated the phase modulating properties of a liquid crystal television (LCTV) panel, as applied to a joint transform correlator (JTC) for pattern recognition and identification. It was found that the LCTV under investigation can modulate close to 2π of phase under optimum brightness control (bias) conditions. It was also determined that this phase-mostly LCTV operation produced the best JTPS (more higher-order fringes) and the brightest correlation signals.

The overall light efficiency of the phase modulation operation produced the best JTPS (more higher-order fringes) and the brightest correlation signals.

The overall light efficiency of the phase modulation operation was also measured and compared to the normal amplitude operation. It was found that 82% less light is needed when the LCTVS are operated in the phase-mostly mode. This allows correlators to be built using much smaller coherent sources--saving space and expense. A paper of reporting this finding was published in Applied Optics [4].

9.2 Effects of Thresholding on JTC (APPENDIX 10.2)

In this period of research we have also investigated the effects of thresholding in joint-transform correlation. Some nonlinear effects in the joint-transform power spectrum (JTPS) have been analyzed, and using a linear piecewise model to represent the nonlinear characteristic of the spectrum, we have demonstrated that hard clipping or dc blocking the JTPS produces effects similar to the binarization scheme. Both hard clipping or dc blocking enhance the high-frequency content and increase the modulation depth of the fringes. Direct-current blocking is preferred, however, because this technique not only increases the width and the modulation of the sinusoidal grating, it also eliminates the noise energy content. A paper reporting this investigation has been published in Applied Optics [5].

9.3 LCTV Kinoform Generation (APPENDIX 10.3)

We have also, in this period of research, found that kinoform generation can be obtained by using the commercially available LCTV. We have demonstrated that the kinoform using the phase modulation depth is lower than 2π. However, this type of kinoform has a smaller space bandwidth product and a lower diffraction efficiency. Since most of the commercially available LCTV, the modulation index is relatively small, by using its π phase modulation, the π phase kinoform device is still a promising technique for many optical signal processing applications. A manuscript reporting these findings has been accepted for publication in Optical Engineering [6].

9.4 LCTV Beam Steering (APPENDIX 10.4)

We have, in this period of research, carried out a program of developing a beam steering device using a simple commercially available LCTV. In this experiment, we have shown that a tunable blazed grating can be used in beam steering application, particularly when small angular deflection is needed. Due to the lower modulation index of the current LCTV panel, and the imperfect mapping of the frame grabber, 50-80% diffraction efficiency of the LCTV beam steering is achievable. We have stressed that the higher order of the diffraction spot can be blocked out using a moving pinhole. As the LCTV technology improves, the obstacles can be avoided in the near future, particularly using an LCTV with a phase modulation depth of 2π and smaller pixel sizes. A paper of this nature has been submitted to the Microwave and Optical Technology Letters for publication [7].

9.5 Intensity Compensation JTC (APPENDIX 10.5)

Although the advances of real time joint transform correlator (JTC) has become a significant realtime entity, the correlation profiles are usually very broad, which reduces the accuracy of detection. We have, in this period of research, investigated an intensity compensation filter (ICF) technique to sharpen the correlation peak intensities. We have taken the benefit of the power spectrum of the reference function, by which an ICF can be constructed to improve the correlation performance and the diffraction efficiency in a JTC. Since the synthesis of the ICF is basically based on the reference function, the ICF can be regarded as an object independent filter. However, if some information is provided by the object function *a priori*, such as estimated SNR, an optimal ICF can then be synthesized. Although the advantage of the CJTC is its strong resistance to noise, yet it lacks the sensitivity to discriminate some high spatial frequency content. On the other hand, the ICF technique would provide an easy make-up for this drawback by balancing the system noise immunity and the discrimination sensitivity and accuracy, which can be achieved by adjusting the threshold (or bias) ratio. From the simulated results, we can see some significant improvements in terms of discrimination capability and diffraction efficiency for noisy input object, cluttered object, multi-target environment, etc. The technique can also be used in fringe binarization as a pre-binarization processing, which would ease the problem of determining the proper threshold level that decreases the risk of faulty correlation peaks. The detailed content of this work has been accepted for publication in Applied Optics [8].

9.6 Multi-Target Detection Spatial Synthesis JTC (APPENDIX 10.6)

Joint transform correlator offers the advantages of simplicity of alignment and suitable for hybrid-optical processing. However, due to heavy DC content of the input target, it also produces relatively broad correlation profiles, which hinders the application to multi-target detection. Although this problem can be solved by using an intensity compensation filter (ICF), it is generally limited for single reference problems. Nevertheless, this problem can be alleviated if a spatial function, whose Fourier transform (FT) is equivalent to the FT of the reference multiplied by the ICF can be synthesized. We have, in this period, investigated the applicability of this technique for multi-target recognition. We have shown that the spatial synthesis technique can be applied for multi-reference functions, since it synthesizes a finite sized spatial impulse response as a substitute for the reference pattern used for the conventional joint transform correlation. And the spatially synthesized reference functions can be easily implemented with a current state-of-the-art SLM, e.g., LCTV, by using a two-step sign decomposition technique. We have further demonstrated by choosing a proper threshold level, the spatial synthesis joint transform correlation can be fit for different input object conditions, e.g., noise, cluttering, etc. Comparison of the performance between the conventional and spatial synthesis techniques are provided. We have shown that the spatial synthesis technique offers a higher signal discrimination for noisy input, cluttering, and spectral fringe binarization. A paper of this study has been submitted to Applied Optics for publication [9].

9.7 Moment Invariant Neural Net (APPENDIX 107)

An image generally contains a large amount of information, for which patter recognition is usually loaded with heavy and time consuming computation. However, pattern recognition can be performed more efficiently by the biological neural net, which has led to intensive research on artificial neural network (ANN). Because of the massive parallel operation of the neural net, von Neumann digital computer is not suitable for its implemention. Since optics offers the advantage of three dimensional (3-D) interconnection and parallel processing, it has become a prime candidate for the implementation of ANN. Although neural network is robust to input noise, most of the neural network models are not distortion invariant (e.g., shift, rotation and scale variation), which severely limits the practical application. Since the distortion invariant pattern recognition is the ultimate goal that we would like to achieve. In this period of research, we have studied an invariant neural network using the principle of moment invariant. Application to a LCTV optical neural network is provided. We remark that to increase the discriminability and the processing capacity of the neurocomputing, higher order moment invariants should be also considered. However, it would require more pixels for the encoding. Furthermore, since the different bits in the binary code represent the values of different order of magnitude, it represents a nonuniformly weighted code. For instance, the first bit in the 10 digit bits represents a value of 512, but the last bit represents only a value of 1. Because all the bits will be equally processed in the optical neural network, to improve the overall performance, either a uniformly weighted code has to be developed, or the network should be trained to process nonuniformly (e.g., pay more attention to the neurons representing the exponent than those representing the lower digit bits). A paper reporting these findings has been published in Optik [10].

9.8 Mirror-Array Interconnection Neural Net (APPENDIX 10.8)

Optical implementations of neural nets have been burgeoning in recent years. One of the key reasons must be the massive interconnection capabilities of optics, in which either lenslet-array or holographic interconnections are employed. The basic distinction between these techniques is that the lenslet-array interconnection neural network is essentially an incoherent interconnection system, whereas the holographic interconnection is incoherent. Although the advantage of using incoherent light is the capability of suppressing coherent artificial noise, the lenslet-array interconnection suffers from low light efficiency, which limits large-scale operations. To alleviate this shortcoming, we have in this period of research, investigated a mirror-array interconnection method, for which high light efficiency can be achieved. By replacing the commonly used lenslet array with the mirror array, we increase the light efficiency by a factor of N_2. The overall performance of the system depends on the source size, the diffraction effects, and the focal length of the parabolic mirror-array substrate. In short, the synthesizing of a large-scale mirror array for optical interconnections is possible, for which experimental demonstrations are provided. A paper reporting the results have been published in Optics Letters [11].

9.9 Redundant-Interconnection Neural Net (APPENDIX 10.9)

We recently introduced an interpattern-association (IPA) algorithm in an optical neural network, in which the special and the common features among the reference patterns can be determined. However, the interconnection for an IPA network would be highly redundant. Although a more highly redundant interconnection would produce higher noise immunity, the discriminability would be reduced. We have in this period of research studied an optimum-redundant-interconnection network, for which the real performance can be improved. In this study, we have introduced a redundant R-IPA model to improve the performance of the neural network. Although redundant interconnection is more robust, it reduces the discriminability for pattern recognition. Nevertheless, under noisy-input and partial-input situations, the redundant-interconnection network performs better. We have shown that, compared with the Hopfield and the IPA models, the optimum redundant OR-IPA neural network improves the robustness and the pattern discriminability. A paper of the redundant interconnection neural net using LCTVs has been published in Applied Optics [12].

9.10 Polychromatic Neural Net (APPENDIX 10.10)

We have recently presented an optical neural network using inexpensive pocket-size liquid crystal televisions (LCTVs) where the IWM was displayed on the LCTV with a microcomputer. This LCTV neural network architecture is basically a hybrid optical-digital system where the parallelism and interconnectivity of optics is exploited. Currently available LCTVs are built with color liquid-crystal panels, which makes them particularly suitable for application to color neural nets. We have, in this period of research, developed a polychromatic LCTV neural network in which the training set can be decomposed into primary colors, the polychromatic IWM can be synthesized by simply combining the primary color IWMs of the training set. Computer simulated and experimental results show that a color neural net can most likely be constructed using color LCTVs. Furthermore, using the RGB pixel elements of the LCTVs, multichannel neural net operations should also be possible. A paper reporting this research has been published in Optics Communications [13].

9.11 Optical Implementation of Hamming Net (APPENDIX 10.11)

Because of all the features that a Hamming net is particularly suitable for large-scale optical implementation. We have, in this period, presented a modified Hamming net model that reduces the dynamic range requirement of the LCTV-SLM. In this study, we have shown that the Hamming net requires fewer interconnections than the fully interconnected Hopfield neural net. As a K-nearest-neighbor neural network model the Hamming net can be rapidly trained, which requires no analog detection during the training process. These features make Hamming net particularly suitable for large-scale optical implementation. We have also shown that the optical Hamming net can be used as a pattern classifier or an associative memory, if the convergent result is used to recall the exemplar. One of the important aspects of the modified Hamming net is enlarging the Hamming distance of the output patterns at the first layer. This modification relaxes the dynamic range requirement of the

SLM's and also reduces the number of iteration cycles in the maxnet. In order to realize the bipolar nature of the IWM the area-modulation scheme is utilized. Experimental demonstrations have shown that optical implementation of Hamming net has a larger processing capacity compared with the optical Hopfield net. A paper reporting these findings has been published in Applied Optics [14].

9.12 Optical Novelty Filter (APPENDIX 10.12)

In this period of research, we have presented a novelty filter implementation using a photorefractive BSO crystal in a four-wave mixing architecture in conjunction with an object phase carrier modulation. The four-wave mixing technique is advantageous as it does not require a high intensity laser. The novelty filter is simple to implement since it is recorded in the Fourier plane. In addition, a phase carrier modulation is used to separate the higher orders of the object spectrum from the noisy dc component. Using this modification, the output noise can be suppressed and the moving object observed at the output plane. In this investigation, we have found that our optical configuration has a lower laser power requirement than the two-wave mixing and beam fanning techniques. In addition, fast response speeds can be achieved using the BSO crystal. To reduce the effects of the output noise of the system, a phase carrier was used enabling movement in the input scene to be detected. Using an encoded carrier frequency, this technique can be used for tracking a moving object. A paper describing this investigation has been published in Optics Communications [15].

9.13 PR Compact JTC (APPENDIX 10.13)

In this period of research, we have also investigated applications of a thick photorefractive crystal (PR) to a compact JTC synthesis. We have shown that the Bragg diffraction limitation in a thick photorefractive crystal can be relaxed by using a Galilean telescope in a JTC. However, to preserve the space--bandwidth product of the system, an increase of the beam compression ratio M requires a larger transverse size of the crystal. Also the increased size of the Fourier spectrum may decrease the light intensity at the crystal and result in slower response times. Nevertheless, this beam compression can be used to design a compact real-time JTC with a photorefractive crystal. A technical note of reporting this investigation has been published in Applied Optics [16].

9.14 Remarks

The ability to process a large quantity of information at a high speed makes the optical correlator an attractive candidate for applications to machine vision, target tracking and detection, etc. Although conceptually simple, the Vander Lugt correlator, which employs a holographic spatial filtering technique, has inherent filter synthesis and alignment problems, that prevent its wide spread practical application. On the other hand, the Joint Transform Correlator (JTC) is a simple and practical processor that overcomes these two major disadvantages. In this report, we have performed the major tasks proposed in the study of the LCTV-JTC and other LCTV based system, as applied for pattern recognition. We are confident the aim of realizing a practical adaptive LCTV-JTC for practical application would happen in the near future.

References

1. L. J. Cutrona, E. N. Leith, C. J. Palermo, and L. J. Porcello, "Optical Data Processing and Filtering Systems," IRE Trans. Inform. Theory, IT-6, 386 (1960).
2. A. Vander Lugt, "Signal Detection by Complex Spatial Filtering," IEEE Trans. Inform. Theory, IT-10, 139 (1964).
3. F.T.S. Yu, Optical Information Processing, Wiley-Interscience, New York, 1983.
4. D. A. Gregory, J. A. Londin, J. C. Kirsch, E. C. Tam, and F.T.S. Yu, "Using the Hybrid Modulating Properties of Liquid Crystal Television," Appl. Opt., 30, 1374 (1991).
5. A. Tanone, C. Uang, F.T.S. Yu, E. C. Tam and D. A. Gregory, "Effects of Thresholding in Joint-Transform Correlation," Appl. Opt., 31, 4816 (1992).
6. A. Tanone, Z. Zheng, C. M. Uang, and F.T.S. Yu, "Phase Modulation Depth for Real-Time Kinoform Using Liquid Crystal Television," Optical Engineering (In Press).
7. A. Tanone, Z. Zhang, C. M. Uang, and F.T.S. Yu, "An Optical Beam Steering Device Using a Liquid Crystal Television Panel," submitted to Micro. Opt. Tech. Lett.
8. F. Cheng, P. Andres, F.T.S. Yu and D. A. Gregory, "Intensity Compensation for Joint Transform Correlation Peak Enhancement," Appl. Opt. (In Press).
9. F. Cheng, F.T.S. Yu and D. A. Gregory, "Multi-target Detection Using Spatial Synthesis Joint Transform Correlation," submitted to Appl. Opt.
10. F.T.S. Yu, Y. Li, X. Yang, T. Lu, and D. A. Gregory, "Application of

Moment Invariant Pattern Recognition to Optical Neural Net," Optik, 89, 55 (1991).

11. F.T.S. Yu, X. Yang, S. Yin and D. A. Gregory, "Mirror-array Optical Interconnected Neural Network," Opt. Lett., 16, 1602 (1991).

12. x. Yang, T. Lu, F.T.S. Yu, and D. A. Gregory, "Redundant-Interconnection Interpattern-Association Neural Network," Applied Optics, 30, 5182 (1991).

13. F.T.S. Yu, X. Yang, and D. A. Gregory, "Polychromatic Neural Networks," Opt. Commun., 88, 81 (1992).

14. X. Yang and F.T.S. Yu, "Optical Implementation of the Hamming Net," Appl. Opt., 31, 3999 (1992).

15. F.T.S. Yu, S. Wu, S. Rajan, A. Mayers, and D. A. Gregory, "Optical Novelty Filter with Phase Carrier," Opt. Commun., 92, 205 (1992).

16. F.T.S. Yu, S. Wu, S. Rajan, and D. A. Gregory, "Compact Joint Transform Correlator with a Thick Photorefractive Crystal," Applied Optics, 31, 2416 (1992).

APPENDIX 10.1

LCTV Hybrid Modulating Properties

a reprint from Applied Optics

Using the hybrid modulating properties of liquid crystal television

Don A. Gregory, Jeffrey A. Loudin, James C. Kirsch, Eddy C. Tam, and Francis T. S. Yu

The phase modulating capabilities of a commercially available liquid crystal television (LCTV) have been investigated and applied to the joint transform optical correlator architecture. Operating the LCTV in a phase modulating mode requires a much smaller coherent light source while still producing a good joint transform power spectrum and good correlation signals.

I. Introduction

The phase modulating properties of liquid crystal spatial light modulators have been investigated by several authors.[1,2] The phase modulating characteristics of liquid crystal televisions (LCTVs) have recently been reported also.[3] The results presented here are for the application of the phase modulating property to the well known joint transform correlator architecture.[4] The joint transform correlator, using two LCTVs, has been operating in the phase mostly mode at the U.S. Army Missile Command since 1985, but the phase modulating properties were not well studied.[5]

Early work with the LCTV always made reference to removing the attached film polarizers and using high quality external polarizers.[6] This approach worked quite well in the amplitude mode, but the polarizers made necessary the use of an intense (several milliwatt) laser source. This was due to the inherent absorption of the polarizers. Later it was found that neither of the usual polarizers was really necessary since phase mode operation can be used. This made for a much more efficient use of the input laser light (output power of 1.0 mW) and still gave an excellent joint transform power spectrum (JTPS).

The phase modulation has been measured during the course of this investigation, and it was found that more than 2π of continuous phase change is possible in normal circumstances. Previously, the method used to obtain a binary phase modulation from a nematic LC device is to orient the analyzer perpendicular to the bisector of the fully on and fully off states.[7] This will in effect produce a binary phase modulation of either 0 or π due to the polarization modulation in the liquid crystal layer. The continuous phase shift utilized in this experiment is due to the inherent birefringence of the liquid crystal. A standard Mach-Zehnder arrangement was used to measure the phase modulation of the Seiko LVD 202 LCTV.[8] This is shown in Fig. 1. Fringes were observed to shift when the LCTV was switched off and on and when the brightness control was changed. Details of the measurements are given later.

The joint transform optical correlator architecture is well known; thus detailed operation is not discussed here.[9] A sketch of the architecture is given in Fig. 2. Essentially the two input scenes are joint transformed by the lens L_1, and the transforms interfere in the Fourier transform plane. If the two scenes are exactly alike (Fig. 3), the JTPS produced is the transform (of either identical scene) modulated by a cosine factor (producing fringes). This fringe structure is then illuminated by coherent light (after being displayed on LCTV2), and the far field pattern is observed with the aid of lens L_2. The diffraction orders shown in Fig. 4 are the desired correlation signals.

II. Experimental Results

Experimental results are divided into two sections: those dealing with the actual measurement of the phase modulation and other properties of the LCTV and those that deal with the use of the phase modulating properties in a joint transform correlator.

The first experiment was designed to measure the light throughput of the LCTV as a function of the bias voltage. The original back analyzer glued onto the liquid crystal cell was removed and replaced with a rotatable polarizer. A video image which is bright (grey level of 255 on a scale of 0–255) to the left half of

---

Eddy Tam and F. T. S. Yu are with Pennsylvania State University, University Park, Pennsylvania 16802; the other authors are with U.S. Army Missile Command, Redstone Arsenal, Alabama 35898-5248.

Received 26 February 1990.

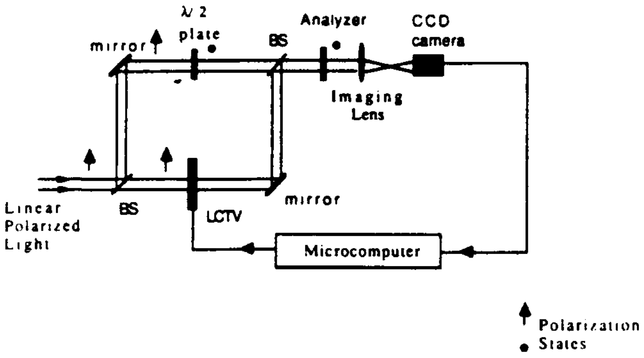

Fig. 1. Mach-Zehnder arrangement for measuring the phase modulation.

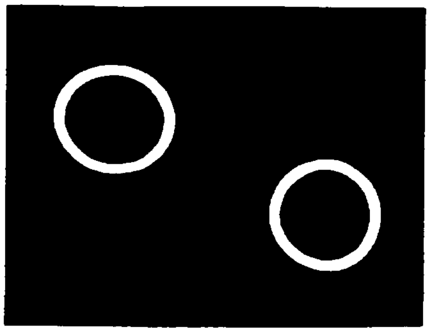

Fig. 3. Scene viewed by the input camera to LCTV 1.

the screen and dark (grey level 0) to the right half of the screen was fed to the LCTV. It was discovered that the LCTV under investigation utilizes a negative logic in the output signal, i.e., a full grey level in the input image results in a minimum voltage across the cell, while the minimum input grey level corresponds to the maximum voltage applied. In the discussion that follows, the ON state of the cell refers to the maximum output signal (minimum grey level) and the OFF state refers to the minimum output signal (maximum grey level). Figure 5 shows the output light intensity as a function of bias voltage with parallel polarizers. The maximum contrast ratio is ~34:1.

The next experiment was performed to measure the polarization modulation effect as a function of bias voltage. The output analyzer was oriented to achieve the maximum transmitted light intensity as the bias voltage was varied. The results of this experiment are shown in Fig. 6. Extremely good polarization modulation was obtained with the maximum modulated angle between the ON and OFF states measured to be 90°. This represents a significant improvement over the first generation LCTVs where the corresponding angle for a Radio Shack model was reported to be only 11°.[7]

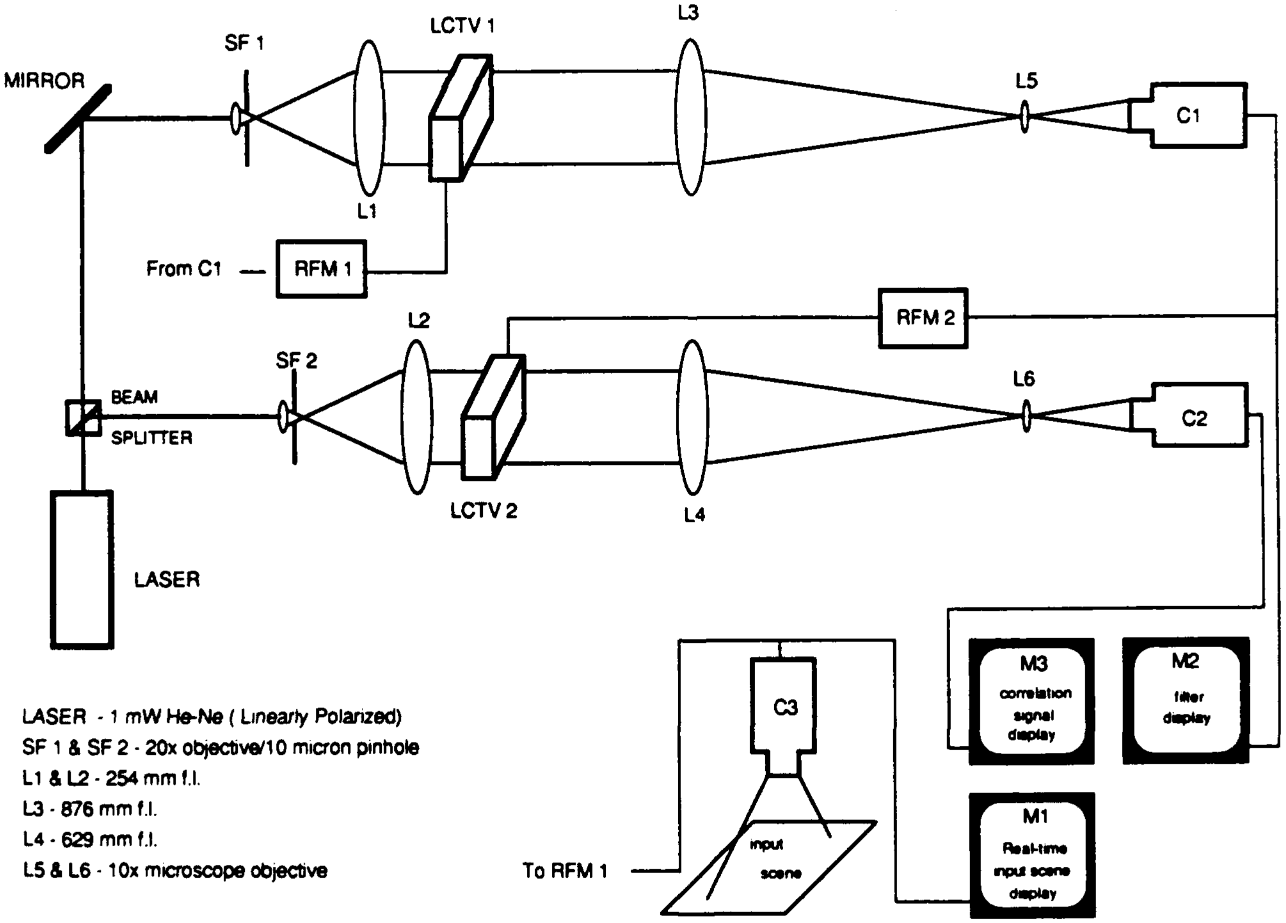

Fig. 2. Joint transform arrangement using two LCTVs.

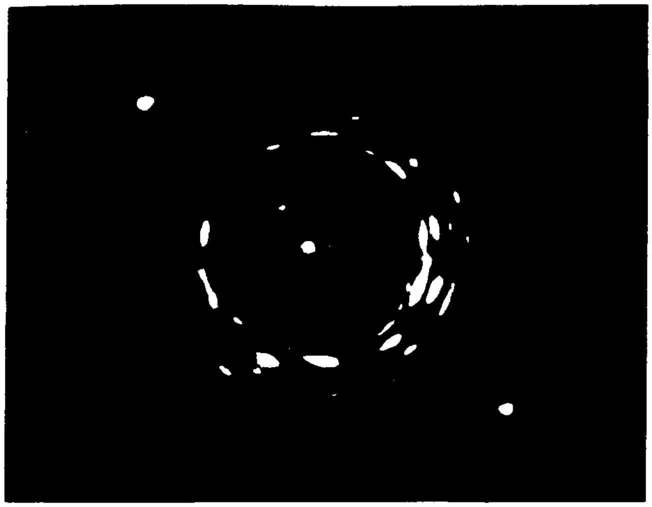

Fig. 4. Correlation signals detected by CCD camera 2.

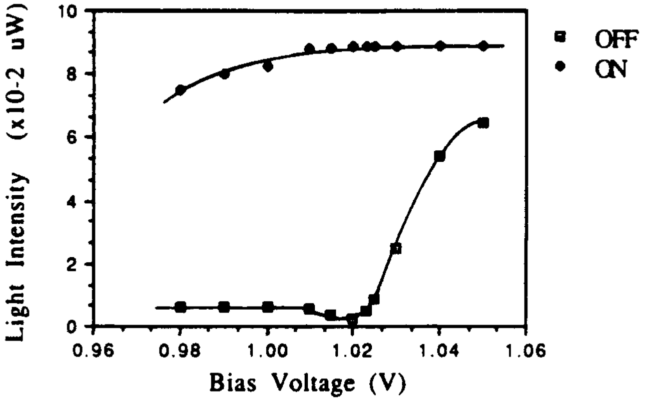

Fig. 5. Output light intensity as a function of bias voltage.

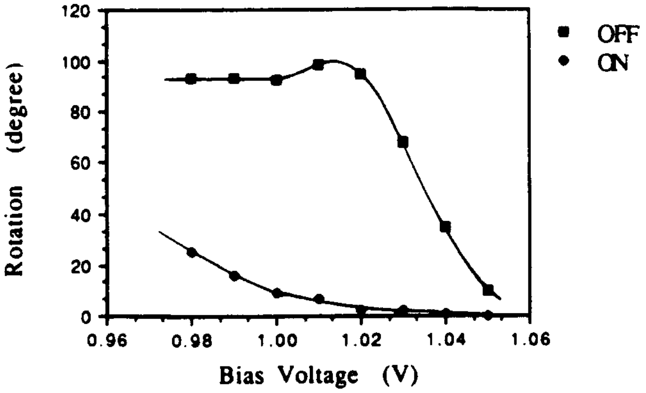

Fig. 6. Polarization rotation as a function of bias voltage.

The phase modulation property of the LCTV has also been investigated. The remaining original polarizer was removed, and, by using a halfwave plate, the polarization direction of the illuminating linear polarized light was aligned parallel to the molecular director on the front surface of the LCTV. The Mach-Zehnder interferometer shown in Fig. 1 was used to measure the fringe shift for both the ON and OFF state pixels as a function of the bias voltage. The results are shown in Figs. 7 and 8. The maximum phase difference between the two states was found to be ~340°. This experiment demonstrates the ability of the LCTV to provide effective modulation in addition to the well known polarization modulation effect. Phase-only modulation can be achieved by setting the bias at the proper value below the optical threshold (bias voltage equal to 1.02 V from Fig. 5) and then limiting the usable grey scale range. However, if the operating range is not limited, the LCTV is operated in a hybrid mode; at higher grey scale values it is phase mostly, and at lower grey scale levels it is a mixture of phase and polarization modulation. One other feature mentioned in earlier publications was also verified here.[2,3] Phase modulation was observed only when the incident polarization direction is aligned parallel to the molecular director on the LCTV's front surface. No phase modulation is observed when the polarization direction is perpendicular to the molecular director.[10]

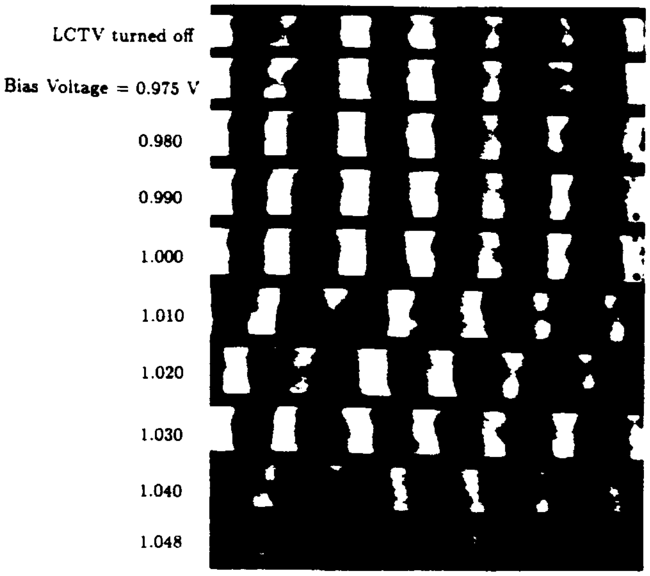

Fig. 7. Fringes produced by the Mach-Zehnder interferometer with LCTV pixels in the OFF state.

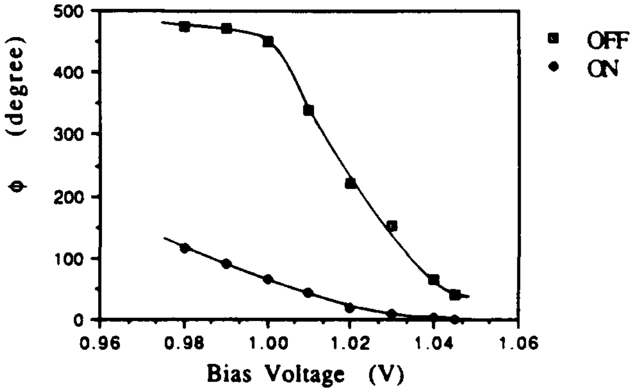

Fig. 8. Phase shift as a function of pixel state and bias voltage.

To judge whether the interferometrically observed

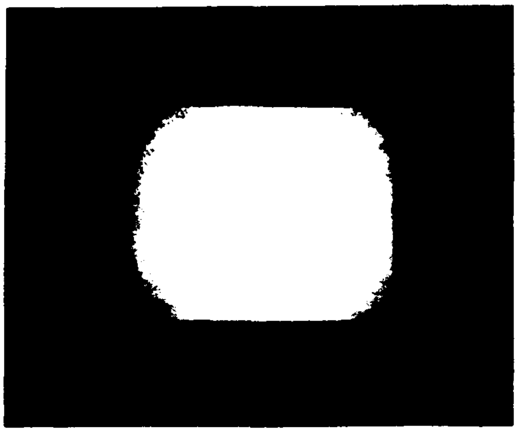

Fig. 9. Scene of Fig. 3 displayed by the LCTV (with He-Ne illumination). This illustrates the lack of amplitude modulation.

phase modulation was actually useful for optical correlator application, the arrangement of Fig. 2 was employed. It is not correct to assume that just because the LCTV modulates the phase, the amplitude modulation is not present or important. The photo of Fig. 9 illustrates the amplitude present in the scene as displayed in He–Ne laser light. The photo was made just after LCTV1 in Fig. 2. Very little amplitude information is present in the scene, but it is not exclusively phase either. The amplitude modulation effect is probably due to the weak dichroism of the liquid crystal. Light is absorbed more when the plane of polarization of incident light is either perpendicular or parallel to the liquid crystal molecules. (It is important to state that the scene as shown in Fig. 9 was produced by adjusting the bias voltage on each LCTV to achieve the best joint transform power spectrum and the best correlation signals as observed by the eye.) Changing the brightness control on the LCTV changed the relative amounts of amplitude and phase contributions. The relative importance of amplitude and phase has been investigated theoretically and should be studied in detail experimentally for application to optical correlator architectures.[11] The scene of Fig. 9 contained mostly phase information. This fact was illustrated by displaying a series of alternating bright and dark bars on the LCTV. An intensity profile was taken through the resulting image in He–Ne light. The ratio of average bright intensity to average dark intensity was only 1.4:1. Compared to the original scene (Fig. 3), there is practically no amplitude information present.

The JTPS of the scene of Fig. 3 as detected by CCD camera 1 is shown in Fig. 10. This scene is often used for alignment purposes and because the Fourier transform is easily recognized. The scene in Fig. 8 was then routed to a second LCTV (same model as the first) and illuminated with an expanded and collimated He–Ne light (see Fig. 2). The resulting image in He–Ne light is shown in Fig. 11. The camera was placed directly behind LCTV2. Again, the LCTV exhibits the behavior observed with LCTV1. The JTPS television was adjusted as before to produce the best phase-mostly

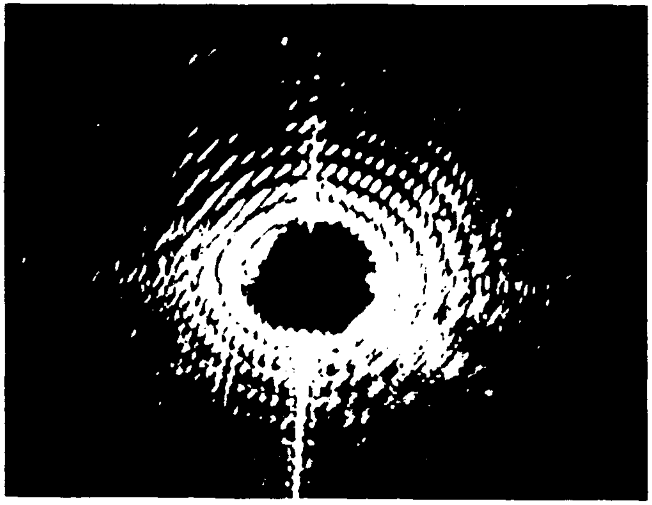

Fig. 10. Joint transform power spectrum of Fig. 3 as detected by CCD camera 1 and displayed on a TV monitor.

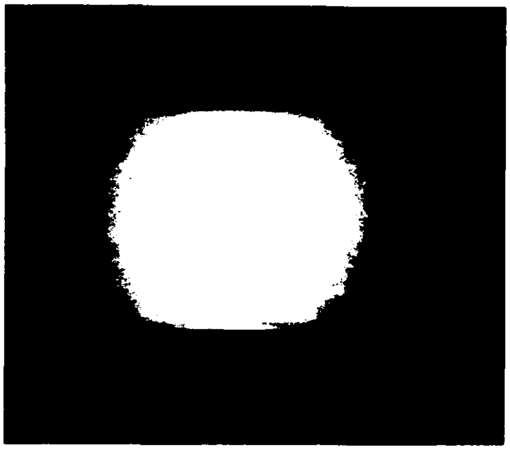

Fig. 11. Joint transform power spectrum of Fig. 8 as displayed on LCTV 2 and illuminated with He–Ne light.

image, and as before this scene still contained some amplitude information. This JTPS produced the brightest correlation signals. An example is given in Fig. 4. The light utilization efficiency of this phase-mostly operation was also measured. In this phase-mostly mode, a transmission efficiency of 28% was measured for a single LCTV. The transmission efficiency was determined by measuring the intensity incident on the LCTV and the intensity transmitted by the LCTV. A transmission efficiency of only 5% was measured for a single LCTV operated in the amplitude mode. This transmission efficiency was determined by measuring the intensity prior to the LCTV and after the output analyzer. This technique assumes a linearly polarized laser output.

III. Conclusions

The phase modulating property of a LCTV has been measured and utilized in a joint transform optical correlator. It was found that the LCTV under investigation can modulate close to 2π of phase under optimum brightness control (bias) conditions. It was also determined that this phase-mostly LCTV operation produced the best JTPS (more higher-order fringes) and the brightest correlation signals.

The overall light efficiency of the phase modulation operation was also measured and compared to the normal amplitude operation. It was found that 82% less light is needed when the LCTVs are operated in the phase-mostly mode. This allows correlators to be built using much smaller coherent sources—saving space and expense.

References

1. W. Bleha *et al.*, Opt. Eng. **17**, 371 (1978).
2. N. Konforti, E. Marom, and S.-T. Wu, "Phase-Only Modulation with Twisted Nematic Liquid-Crystal Spatial Light Modulator," Opt. Lett. **13**, 251–253 (1988).
3. T. H. Barnes, T. Eiju, K. Matsuda, and N. Ooyawa, "Phase-Only Modulation Using a Twisted Nematic Liquid Crystal Television," Appl. Opt. **28**, 4845–4852 (1989).
4. C. S. Weaver and J. W. Goodman, "A Technique for Optically Convolving Two Functions," Appl. Opt. **5**, 1248–1249 (1966).
5. D. Gregory and J. Loudin, "Joint Transform Correlator Limitations," Proc. Soc. Photo-Opt. Instrum. Eng. **1053**, 198 (1989).
6. D. A. Gregory, "Real-Time Pattern Recognition Using a Modified Liquid Crystal Television in a Coherent Optical Correlator," Appl. Opt. **25**, 467–469 (1986).
7. H.-K. Liu, J. A. Davis, and R. A. Lilly, "Optical-Data-Processing Properties of a Liquid-Crystal Television Spatial Light Modulator," Opt. Lett. **10**, 635–637 (1985).
8. E. Hecht and A. Zajac, *Optics* (Addison-Wesley, Reading, MA, 1974), pp. 290–292.
9. F. T. S. Yu, S. Jutamulia, T. W. Lin, and D. A. Gregory, "Adaptive Real-Time Pattern Recognition Using a Liquid Crystal TV Based Joint Transform Correlator," Appl. Opt. **26**, 1370–1372 (1987).
10. B. Bahadur, *Liquid Crystal Displays* (Gordon & Breach, New York, 1984), p. 11.
11. M. Kaura and W. Rhodes, "Phase-With-Quantized Magnitude Complex Spatial Filters Using a Single Spatial Light Modulator," in *Proceedings, 1988 Conference on Pattern Recognition for Advanced Missile Systems* (Redstone Arsenal, AL, 1988), pp. 347–350.

APPENDIX 10.2

Effects of Thresholding on JTC

a reprint from Applied Optics

Effects of thresholding in joint-transform correlation

Aris Tanone, C.-M. Uang, Francis T. S. Yu, Eddy C. Tam, and Don A. Gregory

The joint-transform power spectrum of two identical objects can be represented as a one-dimensional sinusoidal grating modulated by a Fourier transform, and the correlation peaks can be regarded as the first-order diffraction of the grating. The peak intensity and the width are then determined by the aperture and the modulation of the grating. Based on this analysis, it is shown that dc blocking, hard clipping, or binarization of the power spectrum results in higher correlation peak intensity and a narrower peak width. Direct-current blocking is also found to be preferable if the input pattern to the correlator is corrupted by noise.

Introduction

The use of joint-Fourier-transform correlation in optical signal processing was first proposed by Weaver and Goodman[1] and independently by Rau[2] in the 1960's. Recently, because of the availability of real-time spatial light modulators and recording devices, there has been much research effort in implementing the joint-transform correlation process in various architectures and algorithms. Different techniques to increase the efficiency and output-plane signal-to-noise ratio (SNR) have been proposed, including binarizing the joint-transform power spectrum (JTPS). This became popular after binary-type spatial light modulators became available.[3–15]

We analyze the effect of some commonly used nonlinear recording processes on the quality of the correlation functions. The input functions are assumed to be two identical functions $f(x, y)$ separated by a distance $2b$ on the input plane. The power spectrum becomes a sinusoidal grating-type function of spatial frequency $2b/\lambda f$, which is modulated by the power spectrum of $f(x, y)$. The correlation peaks can then be considered as the first-order diffraction orders of the sinusoidal grating. Subsequently the width of the correlation peak is determined by the width of the sinusoidal grating, and the height of the correlation peak is determined by the contrast and the extent of the grating.[16] We show that by applying hard clipping, dc blocking, or binarization on the JTPS, we increase the contrast and the extent of the grating. As a result, the correlation peak intensity increases and the peak width decreases.

In the following a review of the basic joint-transform correlation process is given, and the difficulties of linear recording are discussed. A piecewise linear model is presented to describe various nonlinear recording processes and to give an analytical insight into how the power spectrum is affected. To verify the discussions, we give both computer simulations and experimental results.

Linear Recording of the Joint-Transform Power Spectrum

First, assume that two identical functions, separated by a distance $2b$, are displayed on the input plane of a joint-transform correlator. The amplitude transmittance at the input plane is

$$t(x, y) = f(x - b, y) + f(x + b, y). \tag{1}$$

If recorded on a square-law detector, the JTPS becomes

$$H(f_x, f_y) = 2|F(f_x, f_y)|^2[1 + \cos(4\pi b f_x)], \tag{2}$$

where $F(f_x, f_y)$ is the Fourier transform of the input function $f(x, y)$ and $f_x = \xi/\lambda f$, $f_y = \eta/\lambda f$ are the frequency plane coordinates. For simplicity f_x and f_y are normalized to λf. The final correlation is obtained by taking the Fourier transform of the above

---

A. Tanone, C.-M. Uang, and F. T. S. Yu are with the Department of Electrical and Computer Engineering, Pennsylvania State University, University Park, Pennsylvania 16802; E. D. Tam is with the Department of Physics, University of North Carolina at Charlotte, Charlotte, North Carolina 28223; D. A. Gregory is with the U.S. Army Missile Command, Redstone Arsenal, Alabama 35898.

Received 23 January 1992.
0003-6935/92/234816-07$05.00/0.

power spectrum:

$$g(x, y) = 2f(x, y) \bigstar f(x, y) + f(x, y) \bigstar f(x - 2b, y) + f(x, y) \bigstar f(x + 2b, y), \tag{3}$$

where ★ denotes the correlation operation.

Generally the dynamic range of the power spectrum $H(f_x, f_y)$ is much larger than that of virtually any recording device or material currently available, including photographic film. Owing to the point-spread nature of the impulse response of the optical system, the power spectrum has a high-intensity component around $H(0, 0)$ and low-intensity components that die out rapidly as the spatial frequency increases. If the intense low-frequency component is to be recorded, the write light intensity has to be greatly reduced. The weak high-frequency components, in turn, are not recorded. Apparently this linear recording technique results in only a narrow sinusoidal grating aperture and subsequently in weak, broad correlation peaks.

The wide dynamic range of the JTPS is by no means a new subject to the optics community. At the inception of the joint-transform correlator, Weaver and Goodman[1] discussed an alternative system to establish a bias point of the H and D curve of the film, and Rau[17] preserved the dynamic range of the detector by using a dc block to filter out the low spatial frequencies.

Hard Clipping and dc Blocking

Direct-current blocking can be carried out by simply inserting an opaque aperture at the center of the power spectrum. The strong dc component is therefore blocked from the detector. The higher-frequency components can then be recorded linearly. This technique also protects the detector from overheating and other typical side effects of optoelectronic devices such as blooming, internal scattering, and multiple internal reflections.

Another practical approach to recording the power spectrum is to hard clip the power spectrum when the intensity of the spectrum is either higher or lower than the upper or lower recording threshold values of the detector, respectively. This can be done, for example, with a microchannel spatial light modulator,[5] for which the thresholding values can be adjusted. The clipping effect produces a binarylike power spectrum, depending on the levels of the thresholding. Mathematically, the hard-clipping effect of the JTPS in Eq. (2) can be represented by

$$H'(f_x, f_y) = \begin{cases} \alpha H(0, 0) & \text{for } H(f_x, f_y) \geq \alpha H(0, 0) \\ H(f_x, f_y) & \text{for } H_l \leq H(f_x, f_y) < \alpha H(0, 0) \\ 0 & \text{otherwise} \end{cases} \tag{4}$$

where $0 \leq \alpha \leq 1$ is a scaling factor and H_l is the lower detection limit of the detector. Here, a linear piecewise model is presented for the transfer characteristic of the detector. The spectrum is clipped in some of the high-intensity regions, and the rest of the spectrum that falls inside the linear region of the detector is recorded linearly. This transfer characteristic can be described by Eq. (4) if we set $H_l = 0$.

Owing to the circular-symmetry nature of the optical system, the circularly shaped region around the optical axis would be affected the most by this hard-clipped effect. Subsequently we can incorporate a filter function term in Eq. (4) and write the modified spectrum as

$$H_m(f_x, f_y) = H(f_x, f_y) - [H(f_x, f_y) - \alpha H(0, 0)]\mathrm{circ}\left(\frac{r}{r_0}\right). \tag{5}$$

The circular function is

$$\mathrm{circ}\left(\frac{r}{r_0}\right) = \begin{cases} 1 & \text{for } r \leq r_0 \\ 0 & \text{otherwise} \end{cases}, \tag{6}$$

where $r = (f_x^2 + f_y^2)^{1/2}$, $r_0 = d/2$ is the radius of the aperture block, and d is the diameter. By writing Eq. (5), we assume that the circular function is large enough to cover all parts of the power spectrum whose intensities are higher than the threshold values. The value of α determines the thresholding scheme: it is dc blocking when $\alpha = 0$ and hard clipping at various levels when $\alpha \neq 0$. It is interesting to note that the second term of $H_m(f_x, f_y)$ resembles the filter used in a phase-contrast microscope.

Under unity illumination, the complex amplitude of light at the output plane is the Fourier transform of Eq. (5):

$$g_r(x, y) = g(x, y) - g(x, y) \otimes \left(\frac{\pi d^2}{4}\right) \times \left\{\frac{2J_1[\pi d(x^2 + y^2)^{1/2}]}{\pi d(x^2 + y^2)^{1/2}}\right\} + \alpha H(0, 0)\left(\frac{\pi d^2}{4}\right)\left\{\frac{2J_1[\pi d(x^2 + y^2)^{1/2}]}{\pi d(x^2 + y^2)^{1/2}}\right\}, \tag{7}$$

where ⊗ denotes the convolution operation and J_1 is the first-order Bessel function of the first kind. Quantitatively the period of the sinusoidal function in Eq. (2) is proportional to $1/2b$, while the Airy disk radius in Eq. (7) is obtained by $\rho = (x^2 + y^2)^{1/2} = 1.22/d$, where ρ is also normalized to λf. Therefore if the opaque aperture covers more than four fringes, that is, if $d > 2/b$, then $\rho = 1.22/d < b/2$, or the main lobe of $2J_1(\pi d\rho)/\pi d\rho$ is smaller than $b/2$. Physically this implies that the second term in Eq. (7) would only subtract a pedestal background term from $g(x, y)$, owing to the presence of this function J_1 term; likewise, the third term would introduce a pedestal background term to the dc component of $g(x, y)$. If the block radius is reduced further, this Bessel-function sombrero-shape pedestal term spreads away from the center with diminishing intensity. This fact was confirmed in a computer simulation. Furthermore, once the high-intensity light around the dc region is blocked out, the input light intensity can be increased to enhance the modulation depth of the fringes, and this will subsequently increase the output correlation peak height and reduce the peak width.

When the input is embedded in white additive Gaussian noise $n(x, y)$, the amplitude transmittance at the input plane becomes

$$t_n(x, y) = t(x, y) + n(x - b, y). \tag{8}$$

The JTPS is then given as

$$\begin{aligned} H_n(f_x, f_y) = {} & 2|F_1|^2 + |N|^2 + F_1N^* + NF_1^* \\ & + (F_1F_1^* + NF_1^*)\exp(-4\pi bf_x) \\ & + (F_1F_1^* + F_1N^*)\exp(4\pi bf_x). \end{aligned} \tag{9}$$

The complex light field at the output plane becomes

$$g_n(x, y) = g(x, y) + n(x, y) \otimes n^*(x, y). \tag{10}$$

In reality, since there is no negative intensity, additive Gaussian noise is only an approximation. Thus the cross product of the image transformation F_1 and the noise transformation term N is always present. Physically these additional terms represent noise that deteriorates the fringe structure of the JTPS. This noise appears as additional cross-correlation terms in Eq. (10) that further deteriorate the correlation output.

In addition to hard clipping and dc blocking of the JTPS, the JTPS can also be binarized according to

$$H(f_x, f_y) = \begin{cases} 1 & \text{for } H(f_x, f_y) \geq H_{\text{th}} \\ 0 & \text{otherwise} \end{cases}, \tag{11}$$

where H_{th} is a threshold level. As we show below, owing to the point-spread nature of the JTPS, the binarization must be imposed on the high-frequency components of the JTPS, which typically carry relatively low light intensity. If we do not block the high-intensity components, these low-intensity components are vulnerable to noise that is represented by the autocorrelation term of noise in Eq. (10), in addition to contributions from internal scattering, internal reflection, and noise that can come from the CCD camera.

Computer Simulations and Experimental Results

Computer simulations were carried out with the input patterns shown in Fig. 1. The fast Fourier transform of the input pattern was computed first, and power-spectrum hard clipping was carried out according to Eq. (4). The fast Fourier transform of the modified power spectrum was then computed, and the correlation results were obtained. The peak-to-sidelobe standard deviation ratio (PSD) is defined as the peak height divided by the standard deviation of the intensity distribution outside the full width at half-maximum (FWHM) of the peak. (This ratio for the amplitude distribution case has also been called a SNR.[18]) The peak-to-sidelobe ratio (PSR), defined as the peak height divided by the average value of the intensity distribution outside the FWHM region, is also calculated. Figure 2 plots the correlation peak heights, the PSD, and the PSR as a function of the input-image noise level (measured in terms of the

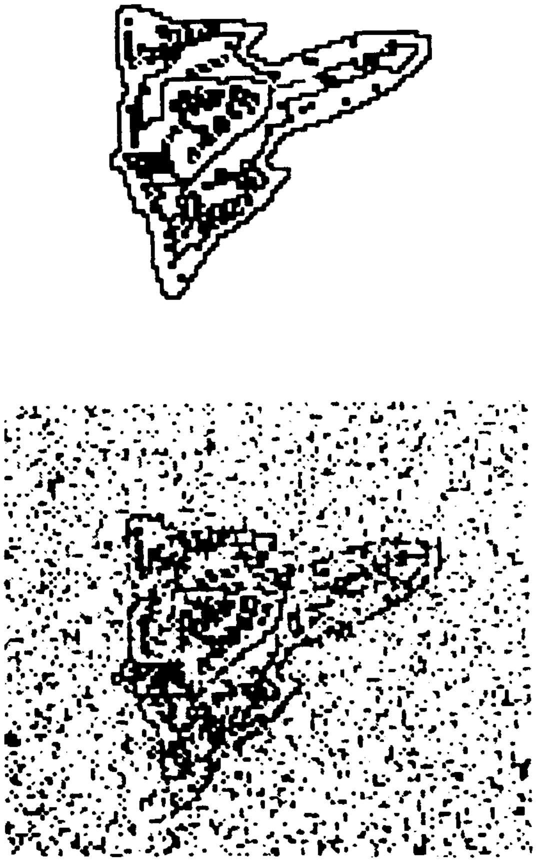

Fig. 1. Input images used: noise-free reference (upper), noisy target (lower); SNR = 4.91 dB.

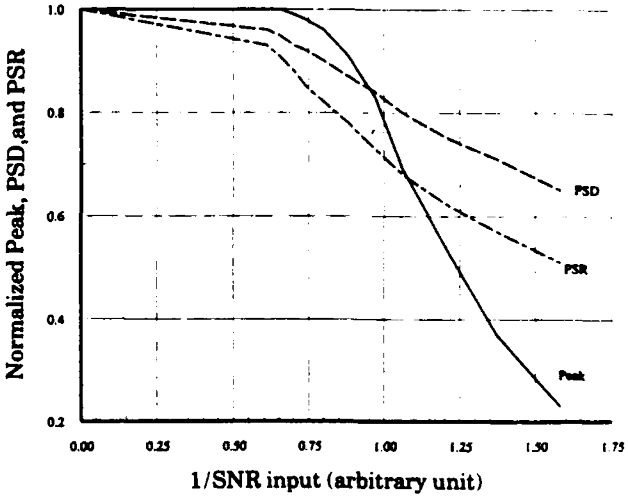

Fig. 2. Variation of the correlation peak heights, the PSD, and the PSR for the hard-clipping case under various noise levels normalized to their values in the noise-free case and α = 0.01.

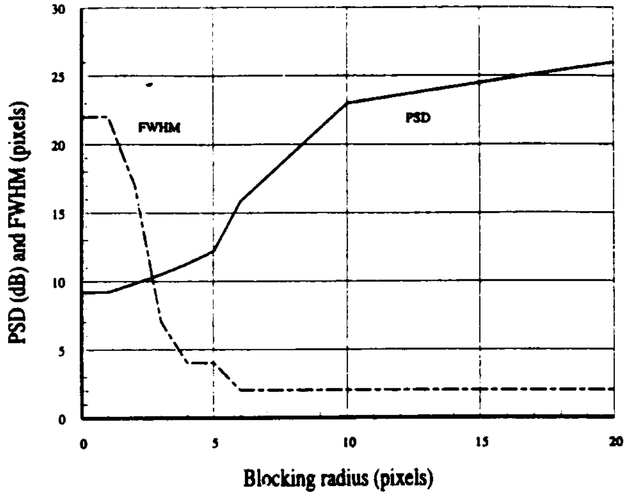

Fig. 3. Variation of the PSD and the FWHM as a function of the blocking radius.

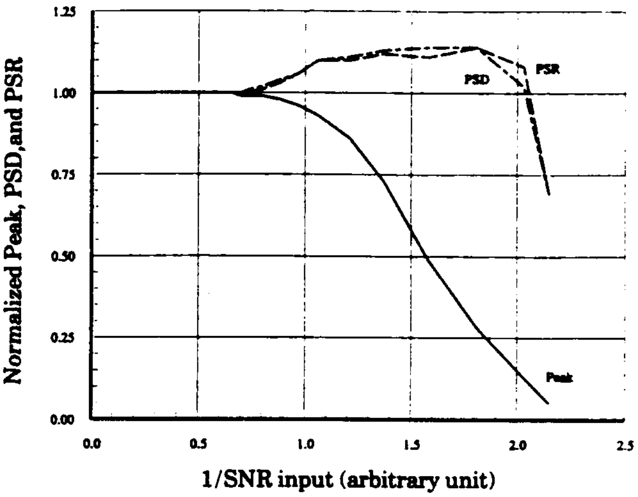

Fig. 4. Variation of the correlation peak heights, the PSD, and the PSR for a blocking radius of 8 pixels under various noise levels normalized to their values in the noise-free case.

reciprocal of the log of the input-image SNR). The threshold level is set at $\alpha = 0.01$ throughout this plot. As predicted, the peak height, the PSD, and the PSR of the correlation decrease when the input noise level increases.

Computer simulations of dc blocking were performed similarly by setting α to zero in Eq. (5). The PSD and the FWHM of the peaks were first calculated as functions of the dc block radius r_0. The results are shown in Fig. 3. It can be seen that as the radius increases, the quality of the correlation signal improves. This is because the JTPS is normalized to the highest intensity in the spectrum. Consequently the modulation of the fringes and the effective aperture of the spectrum are both increased. Lowering the normalization in a computer simulation is equivalent to increasing the write light intensity or to reducing the light sensitivity of the square-law detector. Subsequently the intensity of the correlation peaks increases, and the FWHM decreases.

The effects of additive-input white Gaussian noise on the correlation output were also studied. The variation of the correlation peak amplitude, the PSD, and the PSR as a function of the input noise level are plotted in Fig. 4 with the same notation as in Fig. 2. In contrast to the hard-clipping case, in which the normalized PSD and PSR values gradually decreased after a certain noise level, the values for this case showed some anomaly. First they both increased slightly, ~10% above their values for noise-free and low-noise conditions, and then they fell off rapidly. This anomaly can be explained by referring to the definitions of the PSD and the PSR: the ratio of the peak height to the standard deviation and the ratio of the peak height to the mean of the intensity variation, respectively. Since the numerator for these two quantities, i.e., the peak height in Fig. 4, decreases gradually as the noise level increases, then the only possible explanation is that the denominators decrease faster than the numerator. This is in agreement with both the computer simulation and the experiment. By blocking the dc term of the power spectrum, we also reduce the diffracted light intensity. This in turn produces a low standard deviation and a low mean value at the observation window. As the noise level increases, the fringe structure deteriorates further; less and less light is being diffracted away, thus the correlation peaks start to disappear. Then both the PSD and the PSR decrease rapidly, as shown in Fig. 4. Other images were tried, and the same basically decreasing trends were observed.

Experimental demonstrations were also performed based on the architecture shown in Fig. 5. For simplicity, only the reading stage of the joint-transform correlation is shown. Input patterns were recorded on 35-mm film, and the JTPS was recorded by a CCD camera and subsequently displayed on a liquid-crystal television that operated in an amplitude modulation mode.[4] Finally, correlation output was recorded by a second CCD camera. Figure 6 shows that JTPS for an increasing light-intensity level. The correlation outputs of the corresponding power spectra are given in Fig. 7. In recording the power spectrum of Fig. 6(a), care was taken so that even the strongest light would not exceed the recording dynamic range of the detector. Because of this,

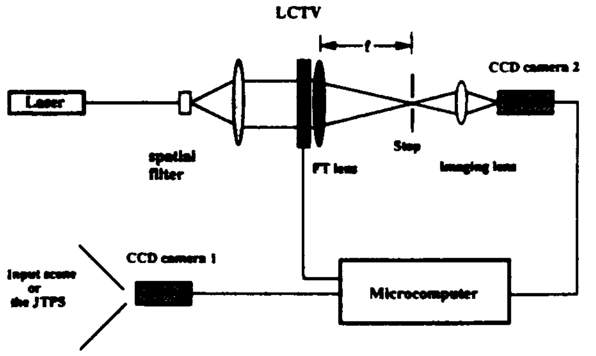

Fig. 5. Experimental setup: LCTV, liquid-crystal television; FT lens, Fourier-transform lens.

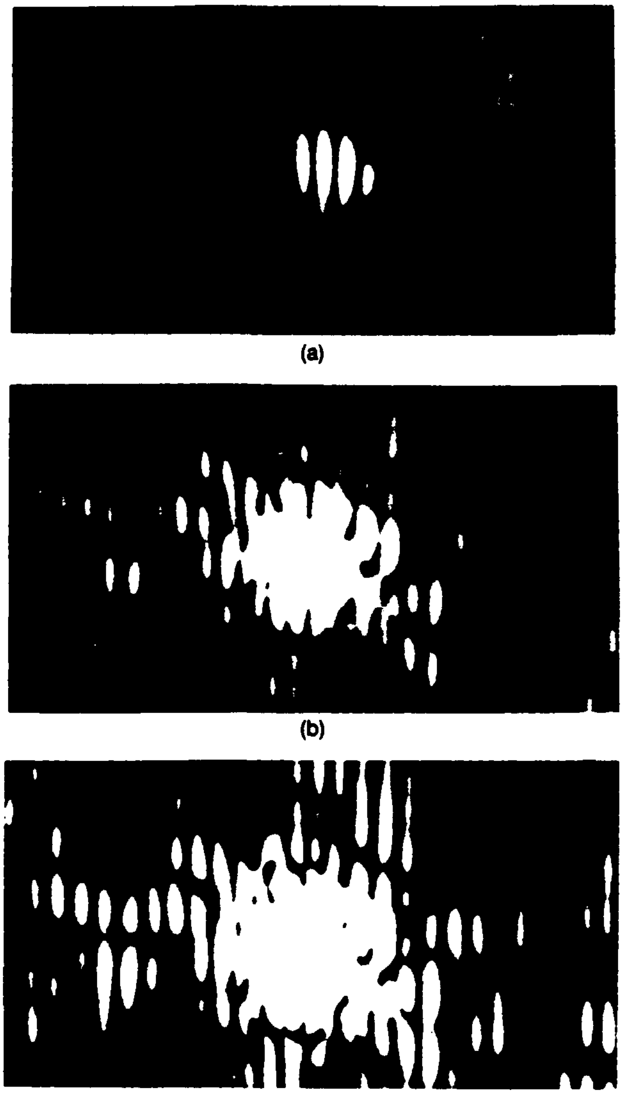
(a)

(b)

(c)

Fig. 6. Experimentally recorded joint-transform power spectrum with increasing writing intensity from (a) to (c).

the higher-frequency components were too weak to be recorded. Consequently there are no observable correlation peaks generated or shown in Fig. 7(a). As the writing light intensity increased, the low-frequency components became clipped; however, more fringes in the higher frequencies were recorded. This in turn diffracted more light to the correlation peaks. Moreover, as the aperture of the sinusoidal grating became larger, the diffraction orders became narrower. This is easily observed in Figs. 7(b) and 7(c).

A dc-blocked and a binarized JTPS for noise-free inputs are shown in Figs. 8(a) and 8(b), respectively, and their corresponding correlation peaks are depicted in Figs. 8(c) and 8(d), respectively. The binarization is carried out according to the scheme of Eq. (11), and after subtracting a dc background level of 20 units in a 0–255 range, we obtain a threshold level of 28. It should be noted that, experimentally, the 8-bit analog-to-digital converter we used also imposes

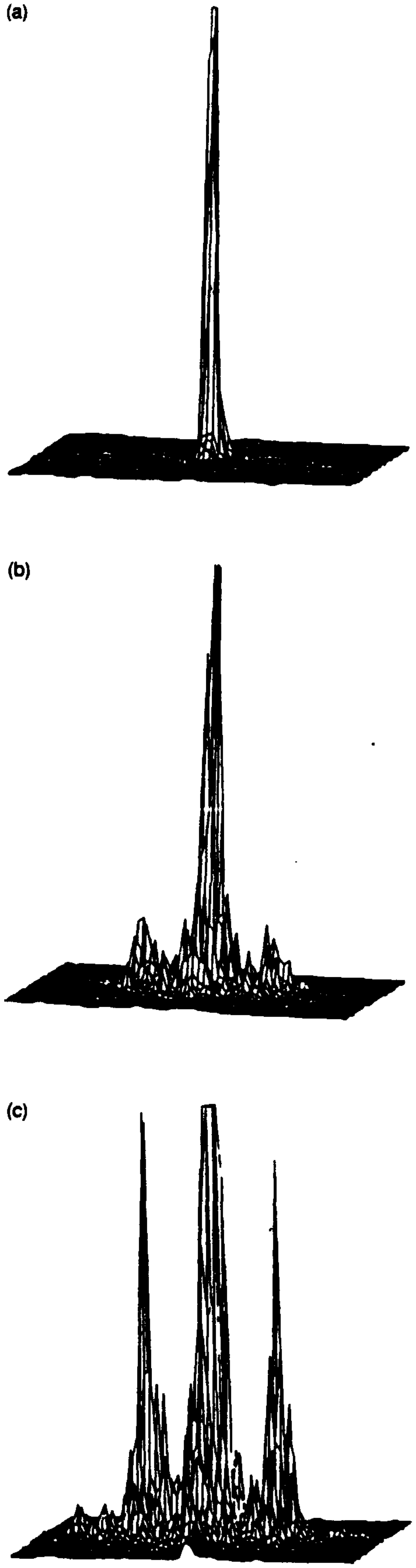

Fig. 7. Three-dimensional plots of the correlation peaks [(a)–(c)] for the JTPS shown in Figs. 6(a)–6(c).

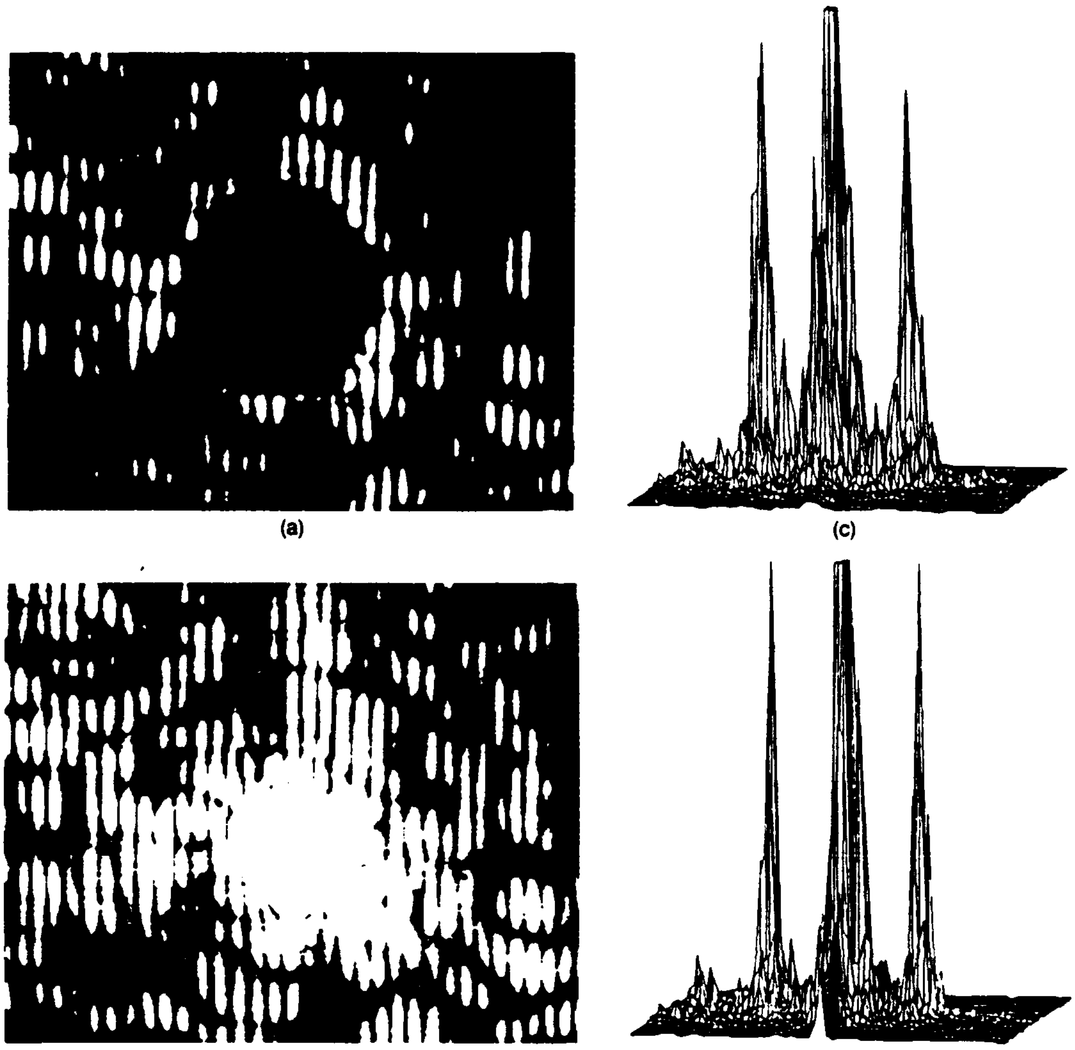
(a) (c)

(b) (d)

Fig. 8. JTPS of noise-free input cases: (a) blocking radius of ~40 pixels and (b) binarized JTPS with a threshold level of 28; their corresponding correlation outputs are shown in (c) and (d).

a limit on the range of thresholding. When the threshold level is low, then beyond the level selected there are no discernible peaks, and below that level only noisy intensity distributions result. This was considered in our computer simulation, and the image intensities were always scaled into a 0–255 gray scale.

Figures 9(a), 9(b), and 9(c) give the output correlation peaks when the input noise is ~7.26 dB for the hard-clipped, the dc-blocked, and the binarized JTPS, respectively. The peak height shown in Fig. 9(b) is 145, while the peak height for the noise-free case, shown in Fig. 8(a), is 255. Both have the same dc background level (20 units) as the other output pictures. When the experimentally measured peak-height value for the dc-blocking case of Fig. 9(b) is normalized to the peak height without noise, shown in Fig. 8(a), we obtain a value of ~53%. This is in accordance with the computer simulation results shown in Fig. 4, in which for this specific noise level, the normalized peak height is ~0.6. Needless to say, the result for the dc-blocking case shown in Fig. 9(b) is much better than the results from the hard-clipping and the binarized cases shown in Figs. 9(a) and 9(c).

From the above observations it is concluded that a properly clipped JTPS, such as the one shown in Fig. 7(c), results in the same correlation output as the binarized case. Furthermore, a certain degree of clipping is required prior to binarizing the JTPS, but once a certain threshold clipping level is exceeded, further processing has no effect on the correlation output. When input noise is considered, we see that both the binarization and the hard-clipping schemes provide similar correlation outputs. However, the correlation peaks shown in Figs. 9(a) and 9(c) for the binarization and the hard-clipping schemes deteriorate faster than the peaks for the dc-blocking scheme shown in Fig. 9(b). All these conclusions support the fact that enlarging the aperture and enhancing the modulation index should produce sharper and higher correlation peaks, but care must be taken when dealing with noisy input images.

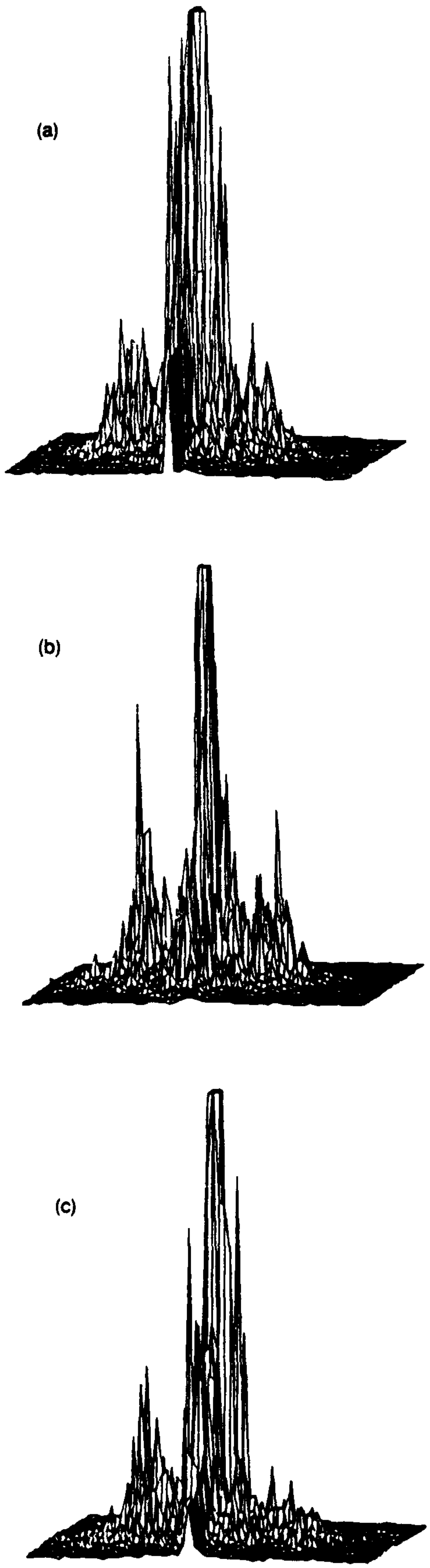

Fig. 9. Correlation peaks for noisy input cases (SNR = 7.26 dB): (a) hard-clipped, (b) dc-blocking, and (c) binarized JTPS. The binarized JTPS is obtained by binarizing the JTPS of (a).

Summary

In summary, some nonlinear effects in the JTPS have been analyzed, and using a linear piecewise model to represent the nonlinear characteristic of the spectrum, we have demonstrated that hard clipping or dc blocking the JTPS produces effects similar to the binarization scheme. Both hard clipping or dc blocking enhance the high-frequency content and increase the modulation depth of the fringes. Direct-current blocking is preferred, however, because this technique not only increases the width and the modulation of the sinusoidal grating, it also eliminates the noise energy content.

Partial support of this research by the U.S. Army Missile Command through the U.S. Army Research Office under contract DAAL03-91-0112 is gratefully acknowledged.

References

1. C. S. Weaver and J. W. Goodman, "Techniques for optically convolving two functions," Appl. Opt. **5**, 1248–1249 (1966).
2. J. E. Rau, "Detection of difference in real distributions," J. Opt. Soc. Am. **56**, 1490–1494 (1966).
3. F. T. S. Yu and X. J. Lu, "A realtime programmable joint transform correlator," Opt. Commun. **52**, 10–20 (1984).
4. F. T. S. Yu, S. Jutamulia, T. W. Lin, and D. A. Gregory, "Adaptive real-time pattern recognition using a liquid crystal TV based joint transform correlator," Appl. Opt. **26**, 1370–1372 (1987).
5. F. T. S. Yu, Q. W. Song, Y. Suzuki, and M. Wu, "Hard-clipping joint transform correlator using a microchannel spatial light modulator," Microwave Opt. Tech. Lett. **1**, 323–326 (1988).
6. B. Javidi and S. F. Odeh, "Multiple object identification by bipolar joint transform correlation," Opt. Eng. **27**, 295–300 (1988).
7. F. T. S. Yu, E. C. Tam, and D. A. Gregory, "High-efficiency joint-transform correlator," Opt. Lett. **15**, 1029–1031 (1990).
8. F. T. S. Yu, S. Wu, and A. W. Mayers, "Applications of phase conjugation to a joint transform correlator," Opt. Commun. **71**, 156–160 (1989).
9. D. A. Jared, K. M. Johnson, and G. Moddel, "Joint transform correlator using an amorphous silicon ferroelectric liquid crystal spatial light modulator," Opt. Commun. **76**, 97–102 (1990).
10. T. Iwaki and Y. Mitsuoka, "Optical pattern recognition of letters by a joint-transform correlator using a ferroelectric liquid-crystal spatial light modulator," Opt. Lett. **15**, 1218–1220 (1990).
11. F. T. S. Yu and T. Nagata, "Binary phase only joint transform correlator," Microwave Opt. Tech. Lett. **2**, 15–19 (1989).
12. F. T. S. Yu, F. Cheng, T. Nagata, and D. A. Gregory, "Effects of fringe binarization of multiobject joint transform correlation," Appl. Opt. **28**, 2988–2990 (1989).
13. J. A. Davis, E. A. Merrill, D. M. Cotrell, and R. M. Bunch, "Effects of sampling and binarization in the output of the joint Fourier transform correlator," Opt. Eng. **29**, 1094–1100 (1990).
14. K. H. Fielding and J. L. Horner, "1-*f* binary joint transform correlator," Opt. Eng. **29**, 1081–1087 (1990).
15. S. K. Rogers, J. D. Cline, M. Kabrisky, and J. P. Mills, "New binarization techniques for joint transform correlation," Opt. Eng. **29**, 1088–1093 (1990).
16. A. Tanone and Y. Ohtsuka, "Acoustic parameter measurement by acousto-optic diffraction techniques using a light-beam of one acoustic wavelength width," Ultrasonics **20**(9), 206–210 (1982).
17. J. E. Rau, "Real-time complex spatial modulation," J. Opt. Soc. Am. **57**, 798–802 (1967).
18. H. Bartlet and J. Horner, "Improving binary phase correlation filters using iterative techniques," Appl. Opt. **24**, 2894–2897 (1985).

APPENDIX 10.3

LCTV Kinoform Generation

Phase modulation depth for real-time kinoform using liquid crystal television.

Aris Tanone, Z. Zhang, C. -M. Uang, and F. T. S. Yu

Electrical and Computer Engineering Department

The Pennsylvania State University, University Park, PA 16802

D. A. Gregory

U.S. Army Missile Command, Redstone Arsenal, Alabama 35898

ABSTRACT

The interest of LCTV kinoform has been reported recently by several investigators. The technique requires modulation depth about 2π, for which most of the commercially available LCTV unable to attain. In this paper, we will discuss an experimental study of generating an LCTV kinoform, in which the modulation depth is limited by π. The major drawbacks of the π phase variation is that, it reduces the diffraction efficiency as well as the space bandwidth product to some what degree about one-fourth as compared with 2π variation. Verification of this findings are reported in this paper.

1. Introduction

Most of the applications of liquid crystal television (LCTV) as a spatial light modulator have utilized the amplitude and polarization modulations of the liquid crystal panel, in which the comprehensive reference of these effects have been reported by Liu and Chao. [1] When incident light is transversely polarized parallel to the front director of a twisted nematic liquid crystal cell, assuming the cell is operated below its optical threshold voltage, it is well known that a phase modulation would occurs. [2,3] Recently, investigators have utilized the effect of the phase modulation of the LCTV's liquid crystal panel, by which Gregory et al[4] have reported the implementation of the phase modulation LCTV on a joint transform correlator, and others have used the LCTV to synthesize real-time holograms as well as and kinoforms. [5-8] By using a tailor-made liquid crystal panel, where the liquid crystal at the input and at the output panel are parallel aligned, instead of 90° apart of the conventional twisted nematic mode, the kinoform can be generated as reported by Amako and Sonehara. [8] However, the phase modulation in the twisted nematic mode is subject to certain constraints using different LCTVs. For instance, to obtain a π phase modulation depth using double passed scheme has been reported by Barnes et al [6]. Recently, Ogiwara et al [9] have also experimentally measured the phase modulation depth of a Seiko-Epson VPJ-700 projection TV, in which they obtained a modulation depth of π. In this paper we shall using the π phase modulation to generate real-time kinoform, which is very convenient to achieve using the commercially available LCTV.

2. Statement of the problem

Kinoform is a computer generated phase hologram, [10-12] unlike most of the computer generated holograms that rely on diffraction effect to reconstruct a complex wave field. In other words, kinoform acts as a Fresnel lens that changes the phase of the illuminating wave by its thickness variation. When the kinoform is displayed on an LCTV that operates in phase modulation mode, the thickness variation of conventional kinoform is substituted by the birefringent effect of the liquid crystal molecules, which varies as a function of applied voltage and the input polarized light.

Since the kinoform algorithm is well established, we simply wrote a program that allowed us to select either an error reduction or an input-output [12] algorithms to generate a 128 × 128 pixel phase distribution from a real object function. A pseudorandom phase array is used with the original object to reduce the effect of losing the amplitude information in the kinoform. The calculated phase values are then converted into gray scale intensities, which are saved in a file for later use. In the simulation, the resulting gray scales are converted back to phase variations, for which a short FFT routine is added to the program for the simulation of the reconstruction process. A mismatch factor α is then introduced, by which if $\alpha = 1$, there is a perfect match, and if $0 < \alpha < 1$, there is a phase mismatch. Physically speaking, a perfect match represents the liquid crystal panel that has a modulation depth of 2π, whereas a phase mismatch represents a phase modulation depth less than 2π.

A 3D-plot of computer simulated results of the reconstructed images, when the modulation depth is 2π and π, are shown in Fig. 1(a) and 1(b), respectively. Notice that the output images have been thresholded to show the surface profile of the reconstructed letter B. However, for unthresholded image, the reconstructed letter is displayed with some intensity variation shown in Fig. 1 (d). Thus it is trivial that the noisy effect at the left-hand letter in Fig. 1(b) is the non thresholded mirror image, whereas for perfect match cases shown in Fig. 1(a) or 1(c), the noise structure are clearly suppressed.

Mention must be made that the presence of false images for phase mismatch, have been advocated by Kermisch and others [13−16] follows the publications of the kinoform by Lesem et al. [10] Since the modulation phase for the kinoform is a 2π-modulo of the phase distribution $\varphi(x,y)$, it can be represented by a non-linear limiter input-output model [11] as shown in Fig. 2 (a). The dashed line has been added in the figure to facilitate the Fourier series expansion of the phase distribution. If the phase variation of the original wavefront is Z, the reconstructed wavefront from the kinoform would be equal to $exp(jZ')$, where we assume that Z' is a periodic function, for which $exp(jZ')$ can be expanded into a Fourier series, such as [11]

$$exp(jZ') = \frac{1}{2\pi}\sum_{m} c_m exp(jmZ), \tag{1}$$

where

$$c_m = \frac{sin[m\pi/N_a]}{m\pi/N_a}\sum_{k}(1/N_a)exp\{j2\pi k(1-m)/N_a\}, \tag{2}$$

and N_a is the total number of the discrete levels. If we introduce a parameter β to take the account of the phase mismatch for the kinoform reconstruction, then by substituting the phase function $\varphi(x,y)$ for Z, Eq. (1) can be written as

$$exp\{jZ'\} = \frac{1}{2\pi}\sum_{m} C'_m exp\{jm\varphi(x,y)\}, \tag{3}$$

with

$$\begin{aligned} c'_m &= \frac{1}{N_a} exp\{j\pi(1+\beta-m)(1-1/N_a)\} \\ &\times \frac{sin(m\pi/N_a)}{m\pi/N_a}\,\frac{sin\{\pi(1+\beta-m)\}}{sin\{\pi(1+\beta-m)/N_a\}}. \end{aligned} \tag{4}$$

If N_a becomes infinitely large, Eq. (4) reduces to

$$c_m^{'} = exp\{j\pi(1+\beta-m)\} \quad \frac{sin\{\pi(1+\beta-m)\}}{\pi(1+\beta-m)}. \tag{5}$$

Further more for $\beta = 0$, we have

$$c_n = \frac{sin\{\pi(n-1/N_a)\}}{\pi(n-1/N_a)}, \tag{6}$$

where $n = (1-m/N_a)$. Note that if $\beta = 0$, the only nonzero term in Eq. (4) is c_1, for which we see that $exp(jZ') = exp[j\varphi(x,y)]$. If β is an integer, the nonzero term in Eq. (1) will be shifted to $n = 1+\beta$, in which the reconstructed wavefront would have n times phase variations. On the other, if β is not an integer value, there will be several nonzero terms in Eq. (1). Needless to say that the $n = 0$ term represents zero-order (i.e., DC) term.

The effect of the liquid crystal panel for phase modulation depth lower than 2π can be represented by the mismatch factor β, for $-1 < \beta \leq 0$. The physical meaning of $\beta = -0.5$ represents that the kinoform generated by the liquid crystal panel has a phase modulation depth of π. In that case, we would observed a pair of terms that contain the original phase function $exp[j\varphi(x,y)]$ and its conjugate as predicted from Eq. (3). These two-terms would eventually responsible for the real and the virtual images reconstruction from the kinoform. Thus it predicts the presence of false (conjugate) image, and the intensity of the false image is inversely proportional to the number of quantization levels N_a. For a conventional process, the phase mismatch mainly depends upon some physical factors in the formation of the kinoform, such as exposure time, illuminating wavelength, and others. For real time implementation, the mismatch is dependent on the phase modulation depth of the device, which is limited by the physical nature of the LCTV. [1-3,7] To avoid the the overlapping as in the case of on-axis hologram, it required to shift the object from the optical axis of the kinoform. [14]. Thus it is important to know that when we would use a phase modulation depth that is smaller than 2π, beside the smaller phase modulation, it also suffer the low diffraction efficiency, and smaller space-bandwidth product compared with the 2π modulation case.

3. Experimental results

The experimental set-up consists of a standard optical Fourier transform architecture. The calculated kinoform is sent as gray scale intensity distribution using a Datacube AT-428 image board to display on the LCTV, which is used a phase modulator. After Fourier transformation, the magnified image is picked up by a CCD camera and displayed on a TV monitor.

The LCTV we used is a Seiko LVD-202 with the front and the back polarizers removed. The phase modulation depth of this LCTV is smaller than 2π if the liquid crystal panel is modulated by intensity level from 0 - 255. Figure 3 shows a set of fringes obtained when the LCTV is placed in one arm of a Mach-Zehnder interferometer, for which the gray-levels ranging from 0 - 255 are sequentially displayed on the LCTV panel. We see that the maximum phase shift is slightly higher than π. This result is also observed by the reduction of zero order intensity level to its minimum value, when a Ronchi grating pattern having a maximum gray level of 180 is displayed on the LCTV operating in the phase modulation mode. [18]

Figure 4 depicts a set of reconstructed images, with different number of quantization levels, i.e, 2, 4, 8 and 16 using the error reduction method. In order to avoid the bright DC spot when recording these reconstructed images, we have selected two adjacent pair of the images having the same image qualities in terms of brightness and similarity to its original object, for which the bright spots have been blocked. From the results we note that when the number of quantization level decrease to 2, the real and its conjugate images would have the same intensity levels.

Since the kinoform image quality has been well established previously, [12,17] we shall not attempt to evaluate other than from visual judgment. Figure 5 shows the typical LCTV kinoform used to reconstruct the images of Fig. 4. As for a quick comparison, the result from a 16 quantization level kinoform (using input-output method) is shown in Fig. 6. From the figure, we see that the false image intensity level is much lower than the error-reduction method, which is shown in the lower part in Fig. 4.

5. Conclusion

Using a non-linear limiter model described by Lee, [11] we have experimentally demonstrated the kinoform using the phase modulation depth of LCTV that is lower than 2π. However this type of kinoform has a smaller space bandwidth product and a lower diffraction efficiency. Since most of the commercially available LCTV, the modulation index is relatively small, by using its π phase modulation, the π phase kinoform device is still a promising technique for many optical signal processing applications.

The partial support of this research by the U.S. Army Missile Command through the

U.S. Army Research Office under contract DAAL03-87-0147 is also gratefully acknowledge. Aris Tanone also acknowledges many fruitful discussions with Eddy C. Tam of University of North Carolina at Charlotte.

References

1. H. -K. Liu and T. -H. Chao, "Liquid crystal television spatial light modulators," Appl. Opt. 28, 4774-4780 (1989).
2. N. Konforti, E. Marom and S.-T. Wu, "Phase-only modulation with twisted nematic liquid crystal spatial light modulators," Opt. Lett., 13, 251 - 253 (1988).
3. K. Lu, B. E. A. Saleh, "Theory and design of the liquid crystal TV as an optical spatial phase modulator," Opt. Eng., 29, 240 - 246,(1990).
4. D. A. Gregory, J. A. Loudin, J. C. Kirsch, E. C. Tam, and F. T. S. Yu, "Using the hybrid modulating properties of liquid crystal television," Appl. Opt., 30, 1374 - 1378, (1991).
5. E. C. Tam, F. T. S. Yu, S. Wu, A. Tanone, S. -D. Wu, John X. Li, and D. A. Gregory, "Implementation of kinoforms using a continuous-phase SLM," OSA 1990 Annual meeting, p. 259 (1990).
6. T. H. Barnes, T. Eiju, K. Matsuda and N. Ooyama, "Phase-only modulation using a twisted nematic liquid crystal television", Appl. Opt. 28, 4845 - 4852, (1989).
7. J. Amako and T. Sonehara, "Computer-generated hologram using TFT active matrix liquid crystal spatial light modulator (TFT-LCSLM)," Jpn. J. Appl. Phys. 29, L1533-L1535, (1990)
8. J. Amako and T. Sonehara, "Kinoform using an electrically controlled birefringent liquid-crystal spatial light modulator," Appl. Opt. 32, 4862-4628, (1990).
9. A. Ogiwara, H. Sakai and J. Ohtsubo, "Application of LCTV to non-linear speckle correlator," Opt. Commun., 86, 513-522, 1991.

10. L. B. Lesem, P. M. Hirsch, and J. A. Jordan, Jr., "The kinoform: A new wavefront reconstruction device," IBM J. Res., Develop. 13, 150-155, (1969).

11. Wai-Hon Lee, "Computer - generated holograms: Techniques and application," in *Progress in Optics*, vol 16, ed. E. Wolf, North-Holland, Amsterdam, (1978).

12. J. R. Fienup, "Iterative method applied to image reconstruction and to computer-generated holograms," Opt. Eng. 19, 297-305, (1980).

13. D. Kermisch, "Image reconstruction from phase information only," J. Opt. Soc. Am., 60, 15 - 17, (1970).

14. J. W. Goodman, and A. M. Silvestri, "Some effects of fourier-domain phase quantization," IBM J. Res. Develop. 14, 478-484, (1970).

15. W. J. Dallas, "Phase quantization - a compact derivation," Appl. Opt., 10, 673-674, (1971).

16. W. J. Dallas, "Phase quantization in holograms - a few illustrations," Appl. Opt., 10, 674-676, (1971).

17. S. Jacobsson, S. Hard, and A. Bolle, "Partially illuminated kinoforms: a computer study," Appl. Opt. 26, 2773-2781, (1987).

18. D. A. Gregory, J. C. Kirsch, A. Tanone, S. Yin, P. Andres, F. T. S. Yu, and E. C. Tam, " Analysis of phase modulation in LCTV based joint transform correlator," submitted to Opt. Lett.

Figure Captions

Fig. 1 Computer simulated result of kinoform reconstruction, (a) with an LCTV having 2π and (b) π, phase modulation depth. (c) and (d) are the 2-D representations of (a) and (b).

Fig. 2 A nonlinear limiter with the input-output relationship shown by the solid line convert the kinoform phase modulation into reconstructed image wavefront.

Fig. 3 The band of fringes obtained when the LCTV was put in one of the arm of a Mach Zehnder interferometer. The gray levels from top to bottom are 255, 180, 160, 154, 136, 70, 58, and 0, respectively.

Fig. 4 The experimental result of kinoform reconstruction using an LCTV having phase modulation depth slightly over π. The number of quantization levels are 2, 4, 8 and 16, respectively, and the kinoform was calculated using the error reduction algorithm.

Fig. 5 The kinoform used to reconstruct the image in Fig. 4 (d).

Fig. 6 Same as Fig. 4 with 16 quantization levels, but the kinoform was calculated using the input-output algorithm.

Aris Tanone received his BS degree and doctor candidate degrees in physics from Gadjah Mada University in 1974 and 1976, respectively. He got his MS degree in applied physics engineering from Hokkaido University in 1981. In 1982 he joined the graduate school of optoelectrotechniques and laser application at the University of Indonesia as a research associate, and then he spent around three years in the microcomputer industry. In 1986 he became the Vice Dean of Academic Affairs at the college of Engineering, Satya Wacana Christian University in Indonesia. He came to the Pennsylvania State University to pursue to pursue his Ph.D. degree in electrical Engineering in 1989. His current research interests include optical image processing, pattern recognition, holography, spatial light modulators, and fiber sensors. He is a member of OSA, SPIE, IEEE, Indonesian Physics Society,and Japan Society of Applied Physics.

Zheng Zhang received her BS degree in electronic engineering from Zhejiang University in China in 1984. Currently she is studying for her MS in the field of optical information processing in Department of Electrical Engineering at Pennsylvania State University. Her current research interest include optical image processing, computer generated hologram and spatial light modulator.

C. -M. Uang received his BS and MS degrees in Electrical Engineering from the National Cheng-Kung University in Taiwan, China, in 1987 and 1983, respectively. He is now a Ph.D. student in Electrical and Computer Engineering in Pennsylvania State University. His current research interests include Optical Neural Networks, Optical Computing, and Optical Information Processing.

Francis T. S. Yu received his BSEE from Mapua Institute of Technology, Manila, Philippines, and his MS and Ph.D. degrees in electrical engineering from the University of Michigan. From 1958 to 1965 he was a teaching fellow, instructor, and lecturer in the Electrical Engineering Department and a research associate with the Communication Sciences Laboratory at the University of Michigan. From 1965 to 1980 he was on the faculty of the Electrical and Computer Engineering Department at Wayne State University. He was a visiting professor in electrical and computer engineering at the University of Michigan during 1978-1979. Since 1980, Dr.Yu has been a professor in the Electrical Engineering Department at the Pennsylvania State University. He has been a consultant to several industrial and government laboratories. He is active in research in the fields of optical signal processing, holography, optics, and information theory and has published numerous technical papers in these areas. He was a recipient of the 1983 Faculty Scholar Medal for Outstanding Achievement in Physical Sciences and Engineering and the 1984 Outstanding Researcher in the College of Engineering at Penn State and was named Evan Pugh Professor of Electrical Engineering there in 1985. He is the author of Introduction to Diffraction, Information Processing and Holography; Optics and Information Theory; Optical Information Processing; White-Light Optical Processing; and Principles of Optical Engineering. Dr.Yu is a Fellow of OSA, SPIE, and IEEE.

Don A. Gregory was born in Alabama in 1953. He earned BS and Ms degrees in physics and a Ph.D. in physics in 1984 from the University of Alabama in Huntsville. Dr. Gregory is currently a research physicist at the U.S. Army Missile Command at Redstone Arsenal, Ala. His interests include optical computing, pattern recognition, and teaching.

He is an adjunct professor of physics at the University of Alabama in Huntsville and the University of Alabama in Birmingham. He is also and adjunct professor of electrical engineering at the Pennsylvania State University.

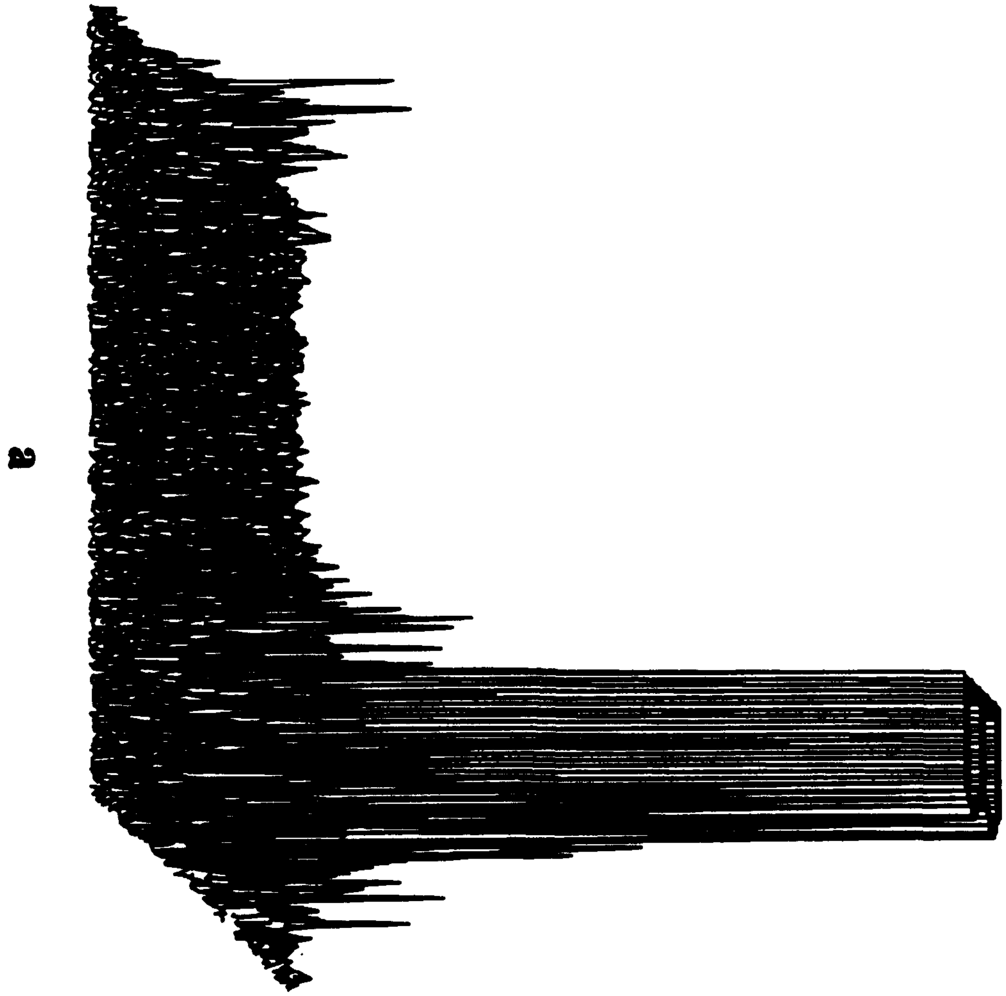

Opt Eng

Fig. 10. Taurine [illegible]

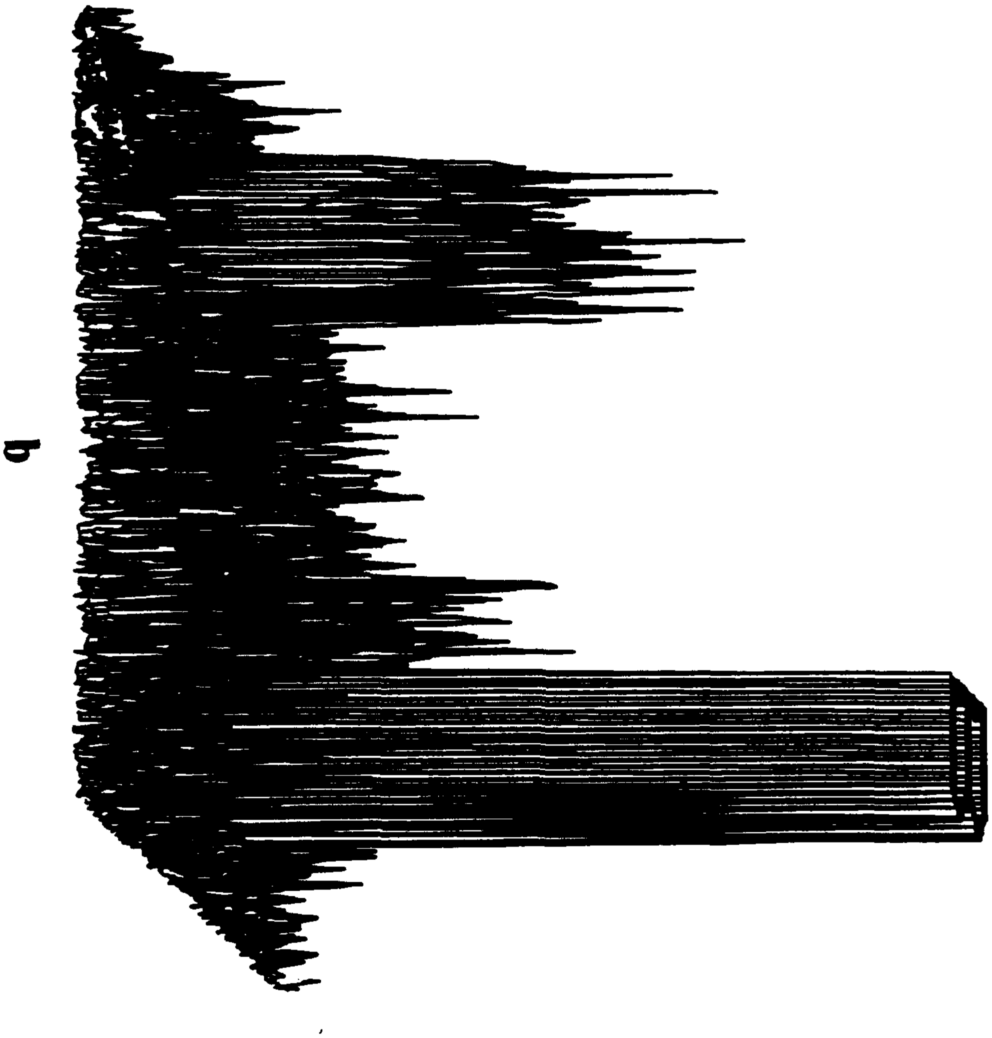

Opt. Eng

Fig 1b Tanone et al

c

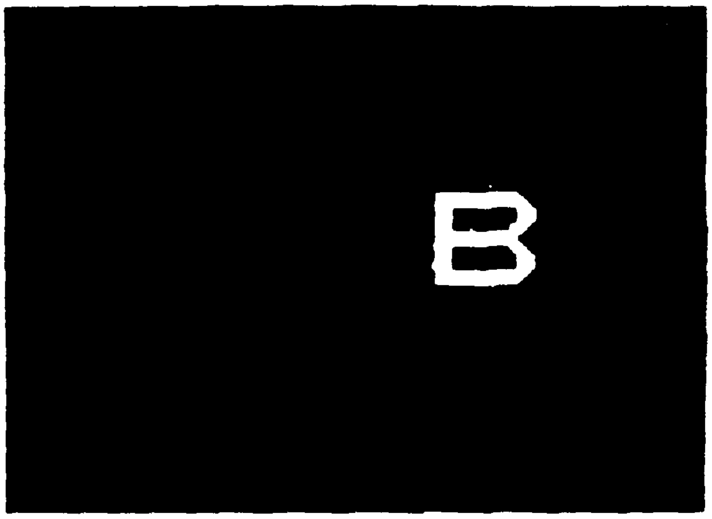

d

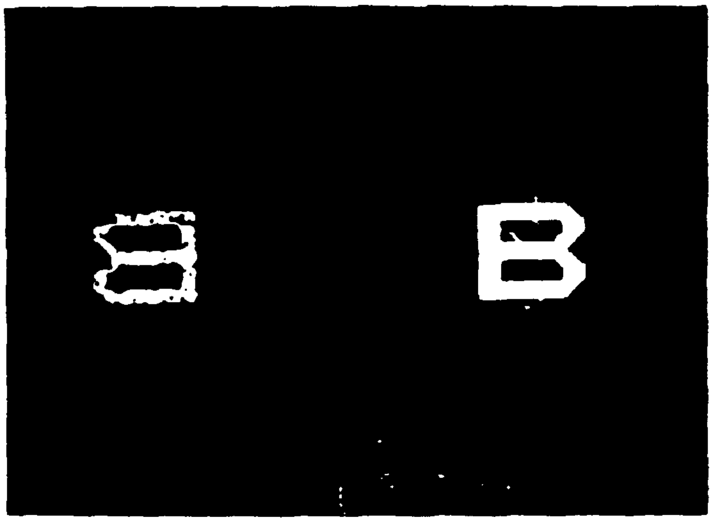

Ori. Eng

Fig [illegible]

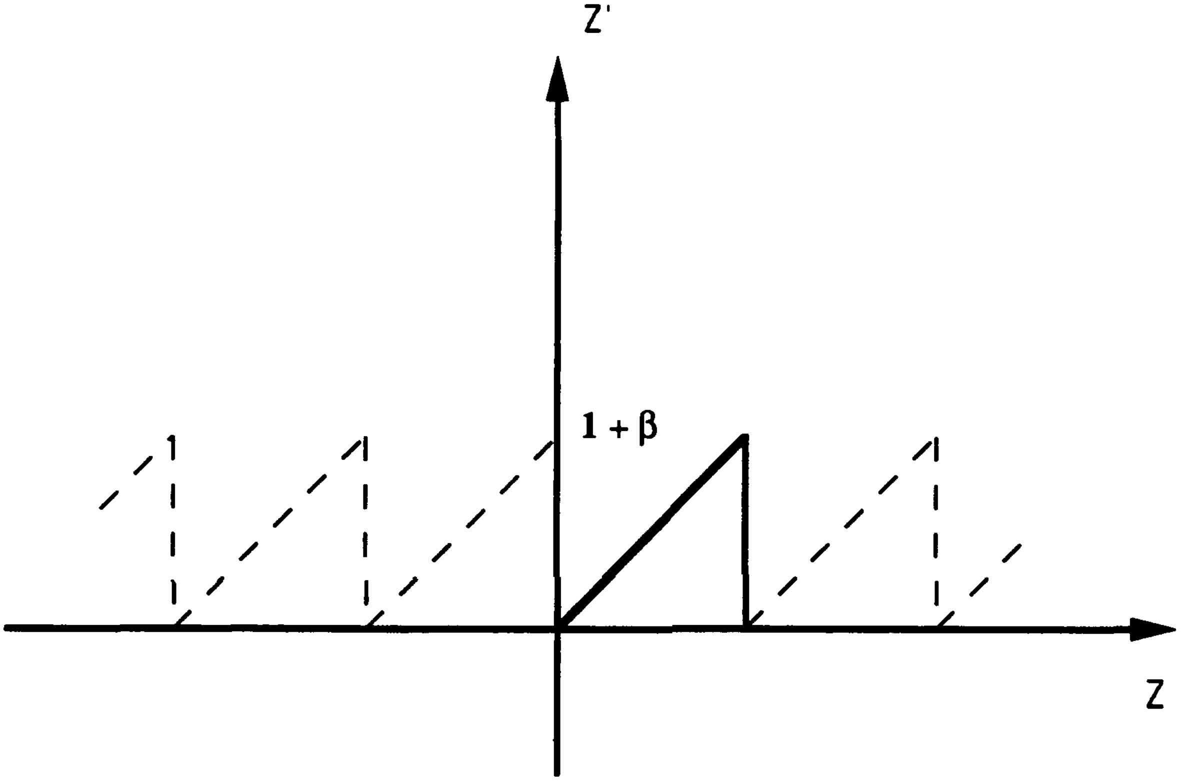
Z'
1 + β
Z

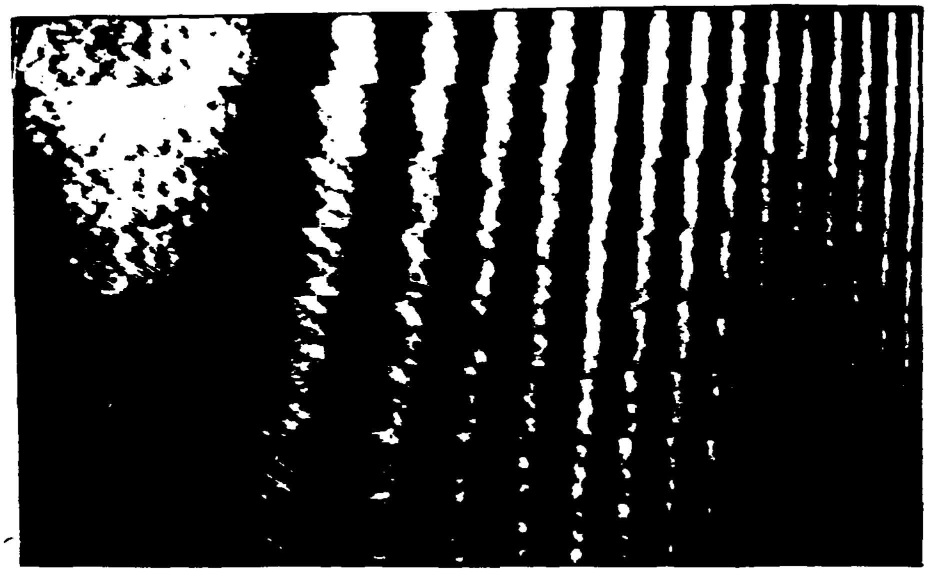

[illegible] Fig [illegible]

[illegible]

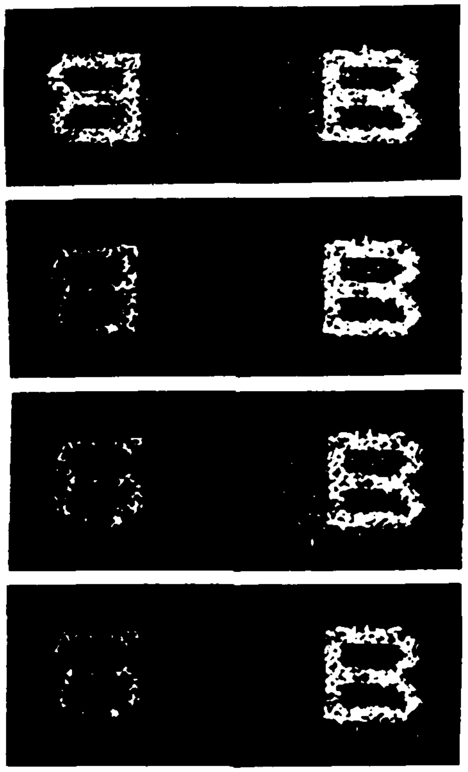

Eng

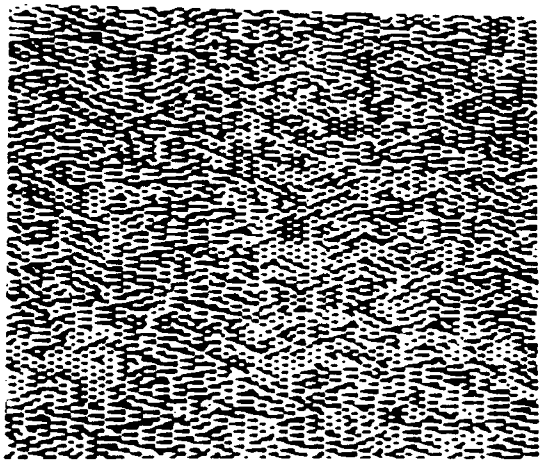

APPENDIX 10.4

LCTV Beam Steerer

An optical beam steering device using a liquid crystal television panel

Aris Tanone, Z. Zhang, C. -M. Uang, and Francis T. S. Yu

Electrical and Computer Engineering Department

The Pennsylvania State University, University Park, PA 16802

Don A. Gregory

U.S. Army Missile Command, Redstone Arsenal, Alabama 35898

ABSTRACT

A blazed grating can be generated using a programmable liquid crystal television (LCTV) panel. We have shown that LCTV panel can be used for optical beam steering, particularly for small angle deflection applications.

Blazed grating [1,2] is one of the conventional optical components to deflect a light beam from its original direction in an optical system. Generally speaking, the simplest form of a blazed grating is the sawtooth shape grating, in which the maximum height of the sawtooth (prism) provides an optical path length of one wavelength, which is equivalent to a 2π phase modulation depth. Following the recent advancement of lithography, there are score of papers report the fabrication of blazed grating. [3] However, a blazed grating is designed for a specific wavelength, and the angle of the prisms and the width of each groove are fixed. Thus if there is a need to change the deflection angle for the beam steering, either mechanical adjustment is required, or the structure of the blazed grating is adjustable. There is a need for small angle beam steering to write-in and read-out a multiplex crystal hologram for optical interconnection, [4] and a low-cost beam steering device is needed. On the other hand it has been known that the commercially available twisted-nematic type liquid crystal television (LCTV) panel can be used as a phase modulator [5–7]. The LCTV panels have been successfully used to generate kinoforms, [8–10] and electro-optics lenses, [11,12] for optical processing. [7,13,14] In this technical note, we provide some experimental demonstrations by which tunable blazed grating can be generated by an LCTV panel.

The experimental set-up is basically a Fourier transform system. The LCTV panel used is a Seiko LVD-202, with its front and back polarizers have been removed. [7,10] When the incident light is parallelly polarized to the front director of a twisted nematic liquid crystal cell and the cell is assumed to operate below the optical thresholded level, the LCTV panel will behave as a phase modulator, in which the phase modulation depth varies as a function of the applied voltage. In other words, the thickness variation that provides the phase variation in conventional components is replaced by the birefringent variation of the liquid crystal molecules, which varies as a function of the applied voltage. We note that the maximum phase modulation depth of this LCTV panel is slightly larger than π for a 633 *nm* light source, which can be shown by writing a Ronchi grating pattern in the LCTV panel or using Mach Zehnder interferometer technique.

The need for a 2π phase modulation depth in a blazed grating is trivial, which is due to the 2π-modulus of phase shift. As long as the maximum height is set to provide a 2π modulation index, the blazed grating is equivalent to the effect of a prism with the same apex angle. By setting the index modulation to 2π, the variation of the apex angle affects the width of the grating, which in turn deflect the direction of the incident beam. If we assumed that that the blazed grating is placed in an optical Fourier transform system, the focal spot at the Fourier plane along the axis is shifted, which is perpendicular to the grooves of the grating.

The experimental results of the beam shifting is shown in Fig. 1(a) to 1(c), where the original focal spot is depicted in Fig. 1(a), which has been isolated from the rest of the spots due to the pixelation of the LCTV screen. By reversing the structure of the grating, the spots have been shifted to the left and then to the right as shown in Fig. 1(b) and 1(c). The presence of high-order terms is due to the Fourier expansion of the saw-tooth grating, which is corresponds to the deviation of the modulation depth away from 2π. [15] However for a maximum phase modulation depth of 1.5π instead of 2π, the peak intensity for various diffraction orders can be obtained by the following equation: [16]

$$\alpha_n^2 = sinc^2(\frac{3-4n}{4}) \qquad (1)$$

where n̂ is the order of diffraction. Thus for n = 0, 1, 2 and 3, we have

$$\alpha_0^2 : \alpha_1^2 : \alpha_2^2 : \alpha_3^2 = 0.09 : 0.81 : 0.03 : 0.01 \tag{2}$$

The possible reason for the unsymmetric diffraction orders shown in Fig. 1 is attributed by the pixel structure for which the frame grabber can not map exactly onto the LCTV panel.

Diffraction efficiency as a function of maximum gray-level for various quantized levels are shown in Fig. 2, where the width of the grating is about 8 pixels. Noticed that the diffraction efficiency is defined as the intensity of the blazed-peak divided by the overall peak intensities. Experimentally, we have found that the diffraction efficiency varies from 50 - 80 % for LCTV blazed grating of various width, in which we assume that the maximum gray-level and the quantized levels are properly selected. Mention must be made that, in practice, the diffraction efficiency is always lower than 100 %, which is due to presence of the dead-zone on the LCTV panel.

Figure 3 depicts the results for the beam steering using the LCTV panel. From this figure we see that the brightest part of the characters (WACANA) is moved from left to right, for which the width of the grating and the number of quantization levels are adjusted. We note that the width of this set of characters is about 6 *mm* long. The result shown in the third row is illuminated by the spot of light under no grating structure is displayed on the LCTV panel. Thus this demonstration shows that the LCTV panel can be used as a tunable blazed grating for beam steering. Needless to say that, by properly tuning the modulation index of the LCTV panel, this characters can be read-out one at a time.

Furthermore, if one uses a 4f optical processing system, where the LCTV panel is placed at the focal plane, an input transparency (contain character G) can be steered at the output plane as shown in Fig. 5. The presence of the false images [15] is primarily due to different diffraction order as can be seen in Fig. 1(b) and 1(c). To block-out the false images, a moving pinhole can be inserted in front of the detector. For practical applications, such as reading or writing a multiplex holograms [4], the moveable pinhole is needed unless the modulation depth of the LCTV panel is tuned to 2π.

The steering angle of the LCTV panel is primarily determined by the grating width, which is being dictated by the pixel width of panel, and the modulation depth, which is being controlled by the crystal cell thickness, the wavelength of light, as well as the applied field. [6] Since the pixel width of current LCTV is about 330 lp/mm, it limits the deflection angle to about 10^{-2} degree using a focal length of 122 cm.

In summary, we have experimentally demonstrated that a tunable blazed grating can be used in beam steering application, particularly when small angular deflection is needed. Due to the lower modulation index of the current LCTV panel, and the imperfect mapping of the frame grabber, 50 - 80 % diffraction efficiency of the LCTV beam steering is achievable. We have stressed that the higher order of the diffraction spot can be blocked out using a moving pinhole. As the LCTV technology improves, the obstacles can be avoided in the near future, particularly using an LCTV with a phase modulation depth of 2π and smaller pixels size.

The partial support of this research by the U.S. Army Missile Command through the U.S. Army Research Office under contract DAAL03-91-0112 is also gratefully acknowledge.

Referênces

1. M. Francon, "*Optical Image Formation and Processing*", Academic Press, 1979, pp. 51 - 54.
2. H. Dammann, "Blazed synthetic phase-only holograms," Optik, 31, 95 - 104, 1970.
3. M. Ekberg, M. Larsson, S. Hard, J. Turunen, M. R. Taghizadeh, J. Westerholm and A. Vàsara, "Multilevel grating array illuminators manufactured by electron-beam lithography," Opt. Commun., 88, 37 - 41, 1992.
4. Shu-dong Wu, Q. Song, A. Mayers, Don A. Gregory and F. T. S. Yu, "Reconfigurable interconnections using photorefractive holograms," Appl. Opt., 29, 1118 - 1125, 1990.
5. N. Konforti, E. Marom and S.-T. Wu, "Phase-only modulation with twisted nematic liquid crystal spatial light modulators," Opt. Lett., 13, 251 - 253 (1988).
6. K. Lu, B. E. A. Saleh, "Theory and design of the liquid crystal TV as an optical spatial phase modulator," Opt. Eng., 29, 240 - 246,(1990).
7. D. A. Gregory, J. A. Loudin, J. C. Kirsch, E. C. Tam, and F. T. S. Yu, "Using the hybrid modulating properties of liquid crystal television," Appl. Opt., 30, 1374 - 1378, (1991).
8. E. C. Tam, F. T. S. Yu, S. Wu, A. Tanone, S. -D. Wu, John X. Li, and D. A. Gregory, "Implementation of kinoforms using a continuous-phase SLM," OSA 1990 Annual meeting, p. 259 (1990).
9. J. Amako and T. Sonehara, "Kinoform using an electrically controlled birefringent liquid-crystal spatial light modulator," Appl. Opt. 32, 4862-4628, (1990).
10. A. Tanone, Z. Zhang, C. M-. Uang, F. T. S. Yu, and Don A. Gregory, "Phase modu-

lation for real-time kinoform generation using a liquid crystal television," submitted to Opt. Eng.

11. E. C. Tam, S. Zhou and M. R. Feldman, "Spatial-light-modulator-based electro-optical imaging system," Appl. Opt., 31, 578 - 580, 1992.
12. E. C. Tam, "Smart electro-optical zoom lens," Opt. Lett., 17, 369 - 371, 1992.
13. T. H. Barnes, T. Eiju, K. Matsuda and N. Ooyama, "Phase-only modulation using a twisted nematic liquid crystal television", Appl. Opt. 28, 4845 - 4852, (1989).
14. D. A. Gregory, J. C. Kirsch, A. Tanone, S. Yin, P. Andres, F. T. S. Yu, and E. C. Tam, " Analysis of phase modulation in LCTV based joint transform correlator," submitted to Opt. Lett.
15. Wai-Hon Lee, "Computer - generated holograms: Techniques and application," in *Progress in Optics*, vol 16, ed. E. Wolf, North-Holland, Amsterdam, (1978).
16. J. R. Fienup, "Improved synthesis and computational methods for computer-generated holograms," Ph. D. thesis, Stanford University, May 1975, (University Microfilms No 75-25523), pp 47 - 49.

Figure Captions

Fig. 1 The experimental results obtained from a tunable LCTV blazed grating (a) Intensity spectrum from the LCTV panel without grating, (b) and (c) show the shifted diffraction spot due to the reverse grating slopes.

Fig. 2 Diffraction efficiency as a function of maximum gray-level of the grating. The grating width is 8 pixels. Curve a and c are obtained with a quantization level of 8 while curve c is obtained with a quantization level of 4.

Fig. 3 Beam steering demonstration. The focal spot is used to illuminate the characters 'WACANA', which about 6 mm wide. The brightest parts show the illumination of focal spot.

Fig. 4 An example of beam steering using a 4f optical processing system. The deflection angle varies from 0 to 0.08°.

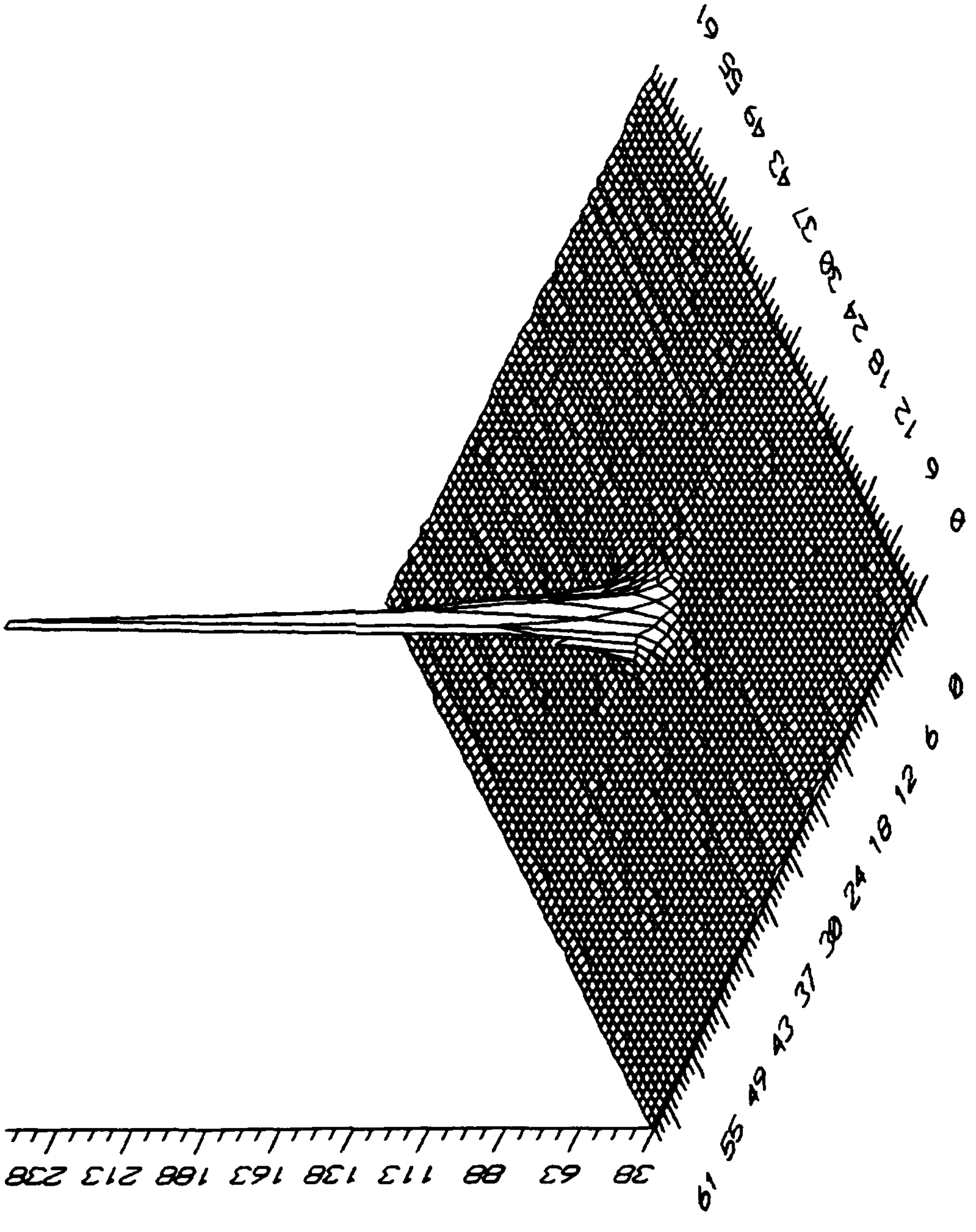
38
63
88
113
138
163
188
213
238
61
55
49
43
37
30
24
18
12
6
0
0
6
12
18
24
30
37
43
49
55
61

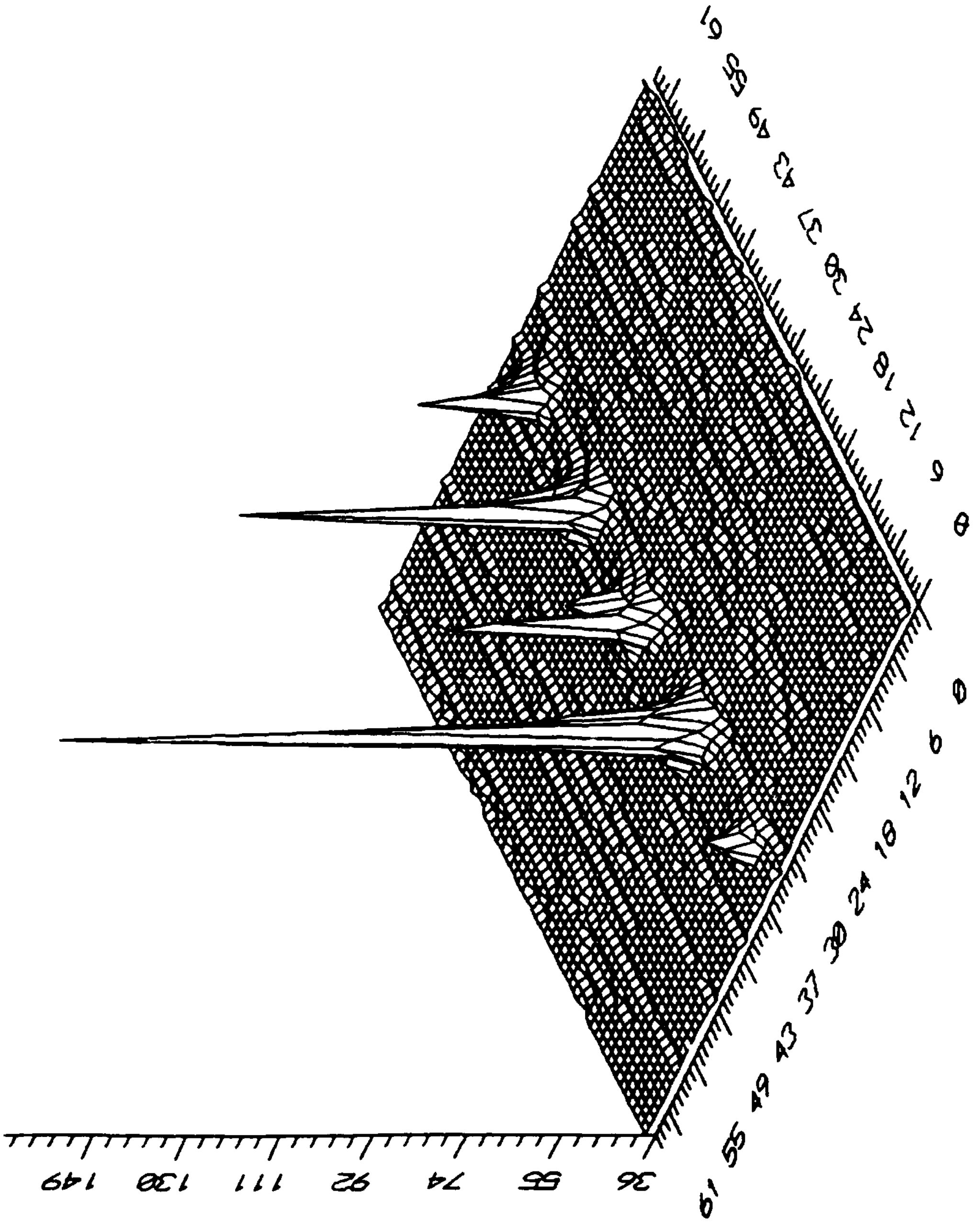
36
55
74
92
111
130
149
0
6
12
18
24
30
37
43
49
55
61
0
6
12
18
24
30
37
43
49
55
61

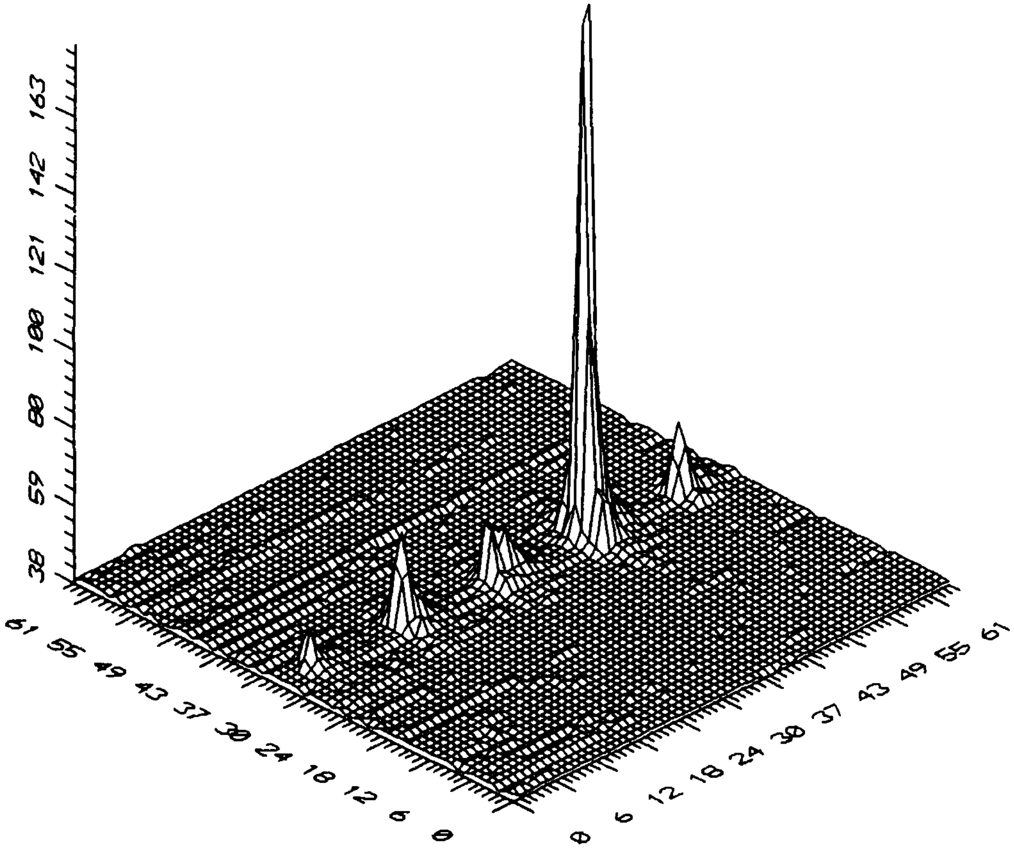
38
59
80
100
121
142
163
61 55 49 43 37 30 24 18 12 6 0
0 6 12 18 24 30 37 43 49 55 61

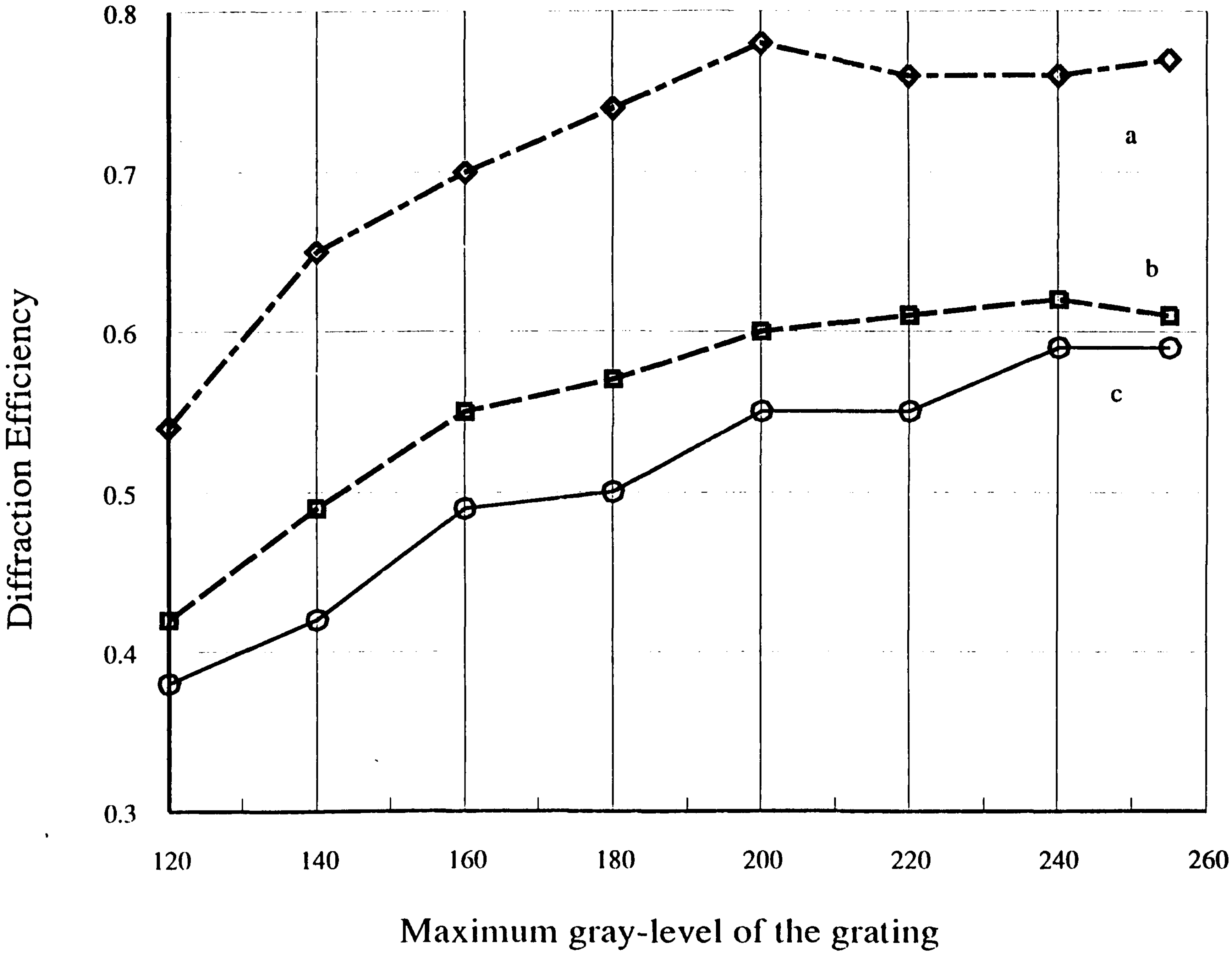
0.8
0.7
0.6
0.5
0.4
0.3
Diffraction Efficiency
120
140
160
180
200
220
240
260
Maximum gray-level of the grating
a
b
c

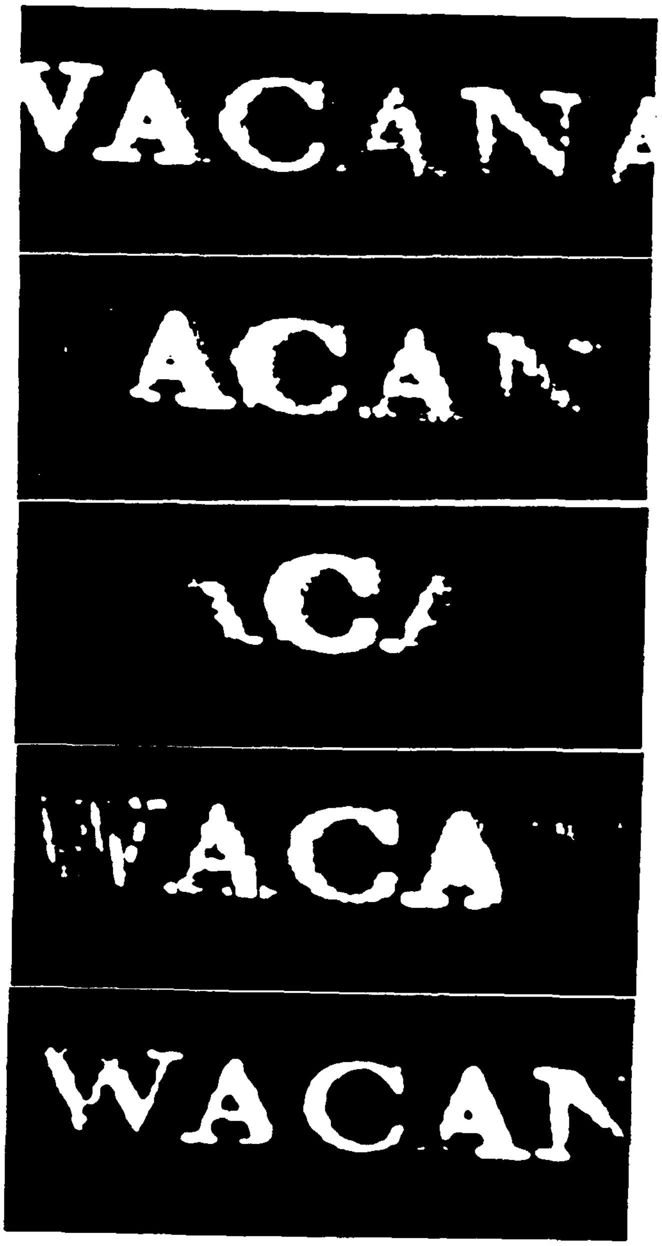
VACAN
ACA
CA
WACA
WACAN

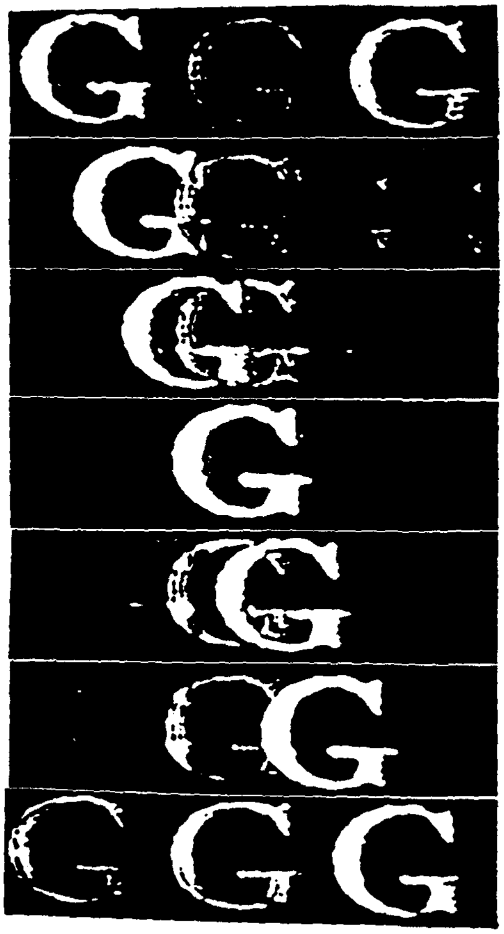

APPENDIX 10.5

Intensity Compensation JTC

Intensity Compensation Filter for Joint Transform Correlation Peak Enhancement

Feng Cheng, Pedro Andres*, and Francis T.S. Yu
Department of Electrical and Computer Engineering
The Pennsylvania State University
University Park, PA 16802

Don Gregory
US Army Missile Command
Redstone Arsenal, AL 35898-5248

Abstract

In this paper, a spatial filtering technique is proposed to sharpen the correlation peak for a joint transform correlator (JTC) by using the inverse reference power spectrum. Ways of handling the pole problems are discussed under various noise conditions. Minimum mean square error method is used to locate the optimum bias value and to estimate threshold level as applied to eradicate the poles. Applications to multi-target recognition and spectral fringe binarization are also studied. Computer simulated results show that the compensated JTC performs better as compared with the conventional JTC.

I. Introduction

The concept of joint transform under coherent illumination should be credited to the work by Weaver and Goodman [1]. Due to the advances of real time spatial light modulators (SLM's), joint transform correlator (JTC) has become a significant realtime entity [2]-[4]. However, the correlation profiles are usually very broad, which reduces the accuracy of detection.

We shall in this paper discuss a technique to enhance the correlation profiles which reduces spectral dynamic range without creating faulty or missing detection. Since the unambiguous correlation is an important issue in signal detection [5][6], avoidance of ambiguity is a major step toward practical implementation. We shall use linear filtering in this study. Our effort is to look at a broad range of frequency contents that could contribute to sharpening the correlation peak intensities. In this study, we shall use an intensity compensation filter (ICF) to suppress the strong frequency contents, by which the weaker components can be enhanced. The technique can be accomplished by using the inverse of the preprocessed reference spectrum, which is input object independent.

II. Sharpening Correlation Profiles

A JTC consists of a reference and an object functions at the input plane, as given by

$$t(x,y)= f(x-b,y) + f(x+b,y), \tag{1}$$

where 2b is the separation between the two functions. The corresponding joint Fourier transform is given by

$$T(p,q) =F(p,q) \exp(-jbp) + F(p,q) \exp(jbp), \tag{2}$$

where p, q are the angular frequency coordinates. And the joint transform power spectral distribution is given as

$$| T |^2 = (2| F |^2) + (| F |^2) \exp(-2jbp) + (| F |^2) \exp(2jbp). \tag{3}$$

By inverse transforming the above equation, a set of autocorrelation distributions can be obtained at the output domain. It is trivial that the joint transform correlation process can be realized by using a hybrid-optical JTC as shown in Fig.1.

Let us now assume a spatial filter, H(p,q) generated by the micro-computer, is used in Eq.(3) to sharpen the correlation profile. Then the filtered amplitude distribution to be displayed back to the SLM is given by

$$|T|^2 H = (2|F|^2 H) + (|F|^2 H)\exp(-2jbp) + (|F|^2 H)\exp(2jbp). \tag{4}$$

We note that if the filter compensated modulation amplitudes (i.e. the last two terms in the brackets) are constant, i.e.

$$|F|^2 H(p,q) = k, \text{ or equivalently } H(p,q) = k/|F|^2, \tag{5}$$

then ideal correlation profiles can be obtained at $x = +2b$ and $x = -2b$, at the output plane, respectively. We see that to achieve a sharp correlation profile, the spatial filter $H(p,q)$ should be proportional to the reciprocal of the reference power spectrum. Thus, the modulation amplitude (i.e. $|F|^2$) can be self-compensated by using the reference spectrum. However, if the input object is different from the reference function, the self-compensation effect is apparently not existing, in which dominant correlation peaks would not be produced. We emphasize that this self-compensating technique is somewhat similar to the amplitude compensation matched filtering, as proposed by Sun et al [7] using a 4-f system.

There are, however, several ways to handle the singularities in Eq.(5), for which the most commonly used technique in digital processing must be thresholding the lower end of $|F(p,q)|^2$ (called TICF). However, the analysis of the relationship between the output correlation and the threshold value is difficult to derive. The empirical range of the threshold values can be found through series of experimental trials. Our simulation results show that the thresholding values are directly proportional to noise variance (including cluttering and background object irradiance) and the proportionality constant (called threshold ratio) can be estimated by using an artificial noise. In the case of unknown noise distribution, the threshold value may be moderately chosen between .005% and 10% of the maximum value of $|F(p,q)|^2$. Over-thresholding (i.e. too small threshold value) makes the system vulnerable to noise, whereas under-thresholding would not produce any effective compensation.

Let us now look at the binary form of ICF (BICF), which is obtained by choosing a threshold value V_T for $|F(p,q)|^2$, such as

$$H(p,q) = \begin{cases} 1, & V_T \geq |F(p,q)|^2 \\ 0, & V_T > |F(p,q)|^2 \end{cases} \quad . \qquad (6)$$

We stress that by using the BICF, some frequency contents of the joint transform spectrum (JTS) are blocked. The technique has some drawbacks as compared with the TICF method. Since the modulation amplitude after compensation is not as uniform as the TICF, the dynamic range requirement for JTS is expected to be much higher than the TICF method. Nevertheless, a significant improvement of the output correlation peaks is still achievable by using BICF as will be shown in the simulated results in the next section. Note that the distinction between BICF and JTS binarization should be understood, in which the binarization on the JTS could produce undesirable effects, as subsequently illustrated by Yu et al [5] and Davis et al [6], respectively.

The optimization of filtering scheme can be formulated according to the minimum mean square error criterion (MMSE) as

$$\min \| \, |F|^2 H - k \, \|^2 . \tag{7}$$

One trivial form of the solution to this equation is

$$H = k / (|F|^2 + a), \tag{8}$$

where "a" is a positive bias to avoid the zeros in $|F(p,q)|^2$. The bias value should be sufficiently high to reduce the error and the noise effects. Thus, the problem of Eq.(7) can be reduced to finding the optimum bias given *a priori* input noise condition. If we assume that the noise is additive white Gaussian distributed with zero mean, the MMSE of Eq.(7) can be written as

$$\min \| \, |F^* (F + N) H - k \|^2 , \tag{9}$$

where superscript * denotes complex conjugate and N(p,q) is the noise spectrum. By combining Eqs.(8) and (9), we have

$$\min_a \left\| \frac{k F^* (F + N)}{|F|^2 + a} - k \right\|^2 = \min_a \left\| k \frac{F^* N - a}{|F|^2 + a} \right\|^2 . \tag{10}$$

which can be written as

$$\min_a \int_{-\infty}^{+\infty} \int_{-\infty}^{+\infty} \frac{|F^* N - a|^2}{(|F|^2 + a)^2} \, dp \, dq = \min_a \int_{-\infty}^{+\infty} \int_{-\infty}^{+\infty} \frac{|F|^2 |N|^2 + a^2}{(|F|^2 + a)^2} \, dp \, dq . \tag{11}$$

It is apparent that by differentiating with respect to "a", an optimum bias level can be found, such as

$$\frac{d}{da} \int_{-\infty}^{+\infty} \int_{-\infty}^{+\infty} \frac{|F|^2 |N|^2 + a^2}{(|F|^2 + a)^2} \, dp \, dq = \int_{-\infty}^{+\infty} \int_{-\infty}^{+\infty} -2 \frac{|F|^2 (|N|^2 - a)}{(|F|^2 + a)^3} \, dp \, dq = 0. \tag{12}$$

Since the noise is assumed white Gaussian, its power spectrum is uniformly distributed, i.e. $|N(p,q)|^2 = |N(0,0)|^2$ which is proportional to the noise variance σ^2. Thus, the solution to Eq.(12) is

$$a = |N(0,0)|^2 = \gamma \sigma^2 . \qquad (13)$$

where γ is the proportionality constant (called bias ratio). In the first stage, we shall adjust the bias ratio γ by which an optimum correlation peak is found, assuming that a noisy object is used. We note that, the estimated noise variance is available *a priori*. The major advantage of using MMSE ICF must be the convenient implementation. From our simulated results, however, there is a similarity between the TICF threshold value and the MMSE ICF bias level, in which the optimum bias is very close to the optimum threshold value. Thus the optimum threshold value for TICF can be calculated based on the result of Eq.(13). However, TICF produces better correlation profiles and has higher diffraction efficiency as compared to MMSE ICF.

Based on the preceding analysis, ICF can be modified to fit multi-reference functions (MRICF). For example, by using thresholding method, Eq.(5) can be extended to form a new filter as described by,

$$H(p,q) = \sum k_i / | F_i (p,q) |^2 , \qquad (14)$$

where $| F_i (p,q) |^2$ is the power spectrum of the ith reference function and k_i is the corresponding proportionality constant. In this case, we need to adjust the values of k_i's, the threshold values for F_i's and the intensity of f_i's, so that the output correlation peaks produced by each of the object-reference pairs can reach the same order of magnitude. The working mechanism for MRICF is shown by an example containing two-object and two-reference functions, in which each pair is separated by 2b along the x and the y axis, respectively. Assume that the pair of reference and object functions along the x axis are identical functions, and the same assumption for the pair of reference-object functions on y axis. Then the filtered joint transform spectral distribution would be

$$|T|^2 H = 4\,|F_1\cos(bp) + F_2\cos(bq)|^2 H\,. \tag{15}$$

Furthermore, the modulation terms corresponding to diffracted autocorrelation signals are given by

$$2\{\,|F_1|^2\cos(2bp) + |F_2|^2\cos(2bq)\,\}\,(\,k_1/|F_1|^2 + k_2/|F_2|^2) =$$

$$2\{(k_1 + k_2|F_2|^2/|F_1|^2)\cos(2bp) + (\,k_2 + k_1|F_1|^2/|F_2|^2)\cos(2bq)\,\}. \tag{16}$$

Thus, we can see that, each modulation term, after the compensation, is equal to a constant plus a residue. It is therefore trivial that the constant terms would produce a sharp correlation peak which is much higher than the unwanted irradiance resulted from the residue terms.

Another interesting aspect is to apply ICF method ahead of the nonlinear operation to reduce the possibility of detection error. A subject to study is the fringe binarization of the joint transform spectrum. As pointed out by Davis [6], the binarization threshold value is very crucial and it affects the correlation output. We stress that, the optimum threshold value for this operation is by no mean easy to determine. However, our simulation shows that, by applying ICF method before the fringe binarization (ICFFB), the optimum threshold value stays around the spectral mean for different noise levels, which is rather reasonable to our conjecture. In fact, this conjecture provides a way to simplify the process of determining a proper threshold value for fringe binarization.

III. Simulated Results

Various simulations were obtained by a VAX machine using a 256X256 pixel frame. Figure 2(a) shows a pair of input images, in which one is used as the reference function. The output correlation distributions obtained with the conventional JTC (CJTC) and the binary ICF JTC (BICF JTC) using threshold value of 0.1% off the maximum value of the joint power spectrum are shown in Figs. 2(b) and 2(c), respectively. In this figure, we see that there is a significant improvement in accuracy of detection for BICF JTC.

To investigate the effects due to cluttering, the input object is assumed cluttered by a shuttle object shown in Fig.3(a). The output correlation distributions by CJTC and TICF JTC are shown in Figs. 3(b) and 3(c), respectively. In this figure we see that the ambiguity of detection occurs using CJTC, whereas the TICF JTC provides a better detection for object cluttering, in which the accuracy of detection is also improved.

To investigate the effect due to noise contamination, we assume the input object is embedded in a white Gaussian noise, in which the SNR is about 5 db shown in Fig.4(a). The output correlation distributions obtained from the CJTC, TICF and MMSE ICF JTC are shown in Figs.4(b), 4(c), and 4(d), respectively. It is apparent that both ICF JTC's perform better. In these results, the threshold level and bias value were chosen to be the product of the threshold (or bias) ratio and noise strength, where the noise strength is defined as the product of the noise variance and the size of noisy area divided by the total image size. We have also noted that, the TICF JTC performs slightly better than the MMSE ICF JTC, since the TICF matches more closely with the object spectrum.

Multi-reference case is shown in Fig.5(a). The output correlation distributions for CJTC and TICF JTC are shown in Figs.5(b) and 5(c), respectively. We stress that, multi-target detection is always a difficult task using CJTC. As seen in Fig.5(b), it is not surprising to see the difficulty of discriminating the autocorrelation peaks from a bundle of other crosscorrelations. However, using the ICF JTC, all the autocorrelation peaks are remarkably sharper, in which the crosscorrelation distributions have been strongly suppressed.

To quantify the performance of the CJTC with respect to the compensated JTC, three simulated results are given in the following:

Firstly, it is a measure of the sharpness of correlation peaks, called peak-to-background ratio (PBR), which is defined as the ratio of the correlation peak intensity to the average intensity of the correlation signal inside the field of view but excluding the peak. Notice that, if the peak intensity is not excluded, PBR would be the same as peak-to-correlation energy (PCE) ratio used by Kumar [8][9]. In other words, the PBR is directly dealing with the ratio of the peak intensity to the unwanted background level, which has the same interpretation as the signal-to-noise ratio, while PCE measures the ratio between the peak intensity and the overall correlation intensity.

Secondly, it is a measure of diffraction efficiency of the correlation filter. For instance, we are usually interested in the peak intensity [9] instead of considering the overall correlation distribution, which is more generally used for the efficiency measurement of the system [10]. Thus we would define the percentage ratio of the correlation peak intensity to the overall spectral intensity as the efficiency measurement, i.e. peak diffraction efficiency (PDE). The major reason of using PDE is that, it directly measures the percentage of spectral intensity contributed to the peak. Although PCE can also be used as a light efficiency measure, yet it does not measure light efficiency between the Fourier plane and the correlation plane.

Thirdly, it is a measure of discrimination, in which we shall use the percent of discrimination defined by Ersoy et al [11] to examine the effectiveness of ICF, that is

$$\Delta\% = 100\,(P_{auto} - P_{cross})/\,P_{auto}\,, \tag{17}$$

where P_{auto} and P_{cross} are the peak intensities of the autocorrelation and the crosscorrelation, respectively. However, since the object for JTC crosscorrelation may have different intensity levels with respect to the reference, this definition is not easy to use in a JTC system. Let us run a test in which the chosen object is a noise free shuttle image having the same average intensity as the reference tank image. We have used the TICF technique to compare with the CJTC. In this simulation, we have shown that the percentages of discrimination for the CJTC the and TICF JTC are 36.2% and 70.3%, respectively. It is apparent that TICF JTC offers a high accuracy of detection.

To further illustrate the effect of the MMSE ICF and the TICF in terms of PBR, we have plotted the variation of PBR as a function of the bias and threshold ratios in Figs.6(a) and (b), respectively. The input object used for the tests is the same object in Fig.2(a) added with four different noise levels. From Fig.6(a), we see that, the optimum bias is very close to the calculated result derived in the preceding section. We have also seen that the variations of the PBR are surprisingly similar in these two techniques.

Figures 7(a) and (b) show the output correlation of PBR and PDE for the CJTC and the TICF JTC. The correlation peak intensities as a function of the input SNR are shown in Fig.7, in which we assume that the object noise strength runs from 0 db to 40 db. From these plots, we see that the effect of the ICF JTC is declining downward approaching the CJTC as the input SNR decreases. Because a large bias or a high threshold value tend to reduce the ICF's variation range and level the ICF toward a constant value. In other words, CJTC is an extreme case of ICF JTC, in which the noise level is assumed infinite, while ICF JTC is designed to achieve a balance of an acceptable noise immunity and the improvement of detection accuracy. In a normal noise level (e.g. 0-40 db), we have shown that the PBR of the TICF JTC is almost 30 to 60 times higher than the CJTC, and PDE is about 3 to 27 times higher.

We further use these two measures to investigate the effect of a JTC fringe binarization and to find out the attainable improvement by using TICF. Let us assume that the threshold value in binarization process is equal to the product of the joint spectral mean and the binarization threshold ratio. The variations for the PBR and the PDE as a function of the binarization threshold ratio are shown in Figs.8(a) and (b), in which the input object is the same as in Fig.6. From these figures, we see that, the optimum binarization threshold ratios shifted considerably, due to different noise distributions. Similar tests for the PBR and the PDE are also plotted in Figs.8(c) and 8(d), using a TICF before binarization. Both the PBR and the PDE are higher in comparison with the uncompensated fringe binarization. The significant improvement is that the optimum binarization threshold ratio for ICFFB is centralized around 1. In other words, the optimum threshold value is brought to the joint spectral mean regardless of the noise level.

In another test for ICFFB, the binarization threshold value is fixed at the joint spectral mean. and the TICF threshold ratio is assumed a wider range variable. The variations of the PBR and the PDE. using the same input object. are plotted in Figs.9(a) and (b), respectively. From the plot of the PDE. we see that. the optimum diffraction efficiency occurs at about 0.6 for TICF threshold ratio, whereas the PBR does not vary significantly within the range of 0.2 to 10 for TICF threshold ratio. This implies that the TICF threshold value is not a demanding parameter in TICF fringe binarization process.

IV. Concluding Remarks

We have taken the benefit of the power spectrum of the reference function. by which an ICF can be constructed to improve the correlation performance and the diffraction efficiency in a JTC. Since the synthesis of the ICF is basically based on the reference function, the ICF can be regarded as an object independent filter. However, if some information is provided by the object function *a priori*, such as estimated SNR, an optimal ICF can then be synthesized. Although the advantage of the CJTC is its strong resistance to noise, yet it lacks the sensitivity to discriminate some high spatial frequency content. On the other hand, the ICF technique would provide an easy make-up for this drawback by balancing the system noise immunity and the discrimination sensitivity and accuracy, which can be achieved by adjusting the threshold (or bias) ratio. From the simulated results, we can see some

some significant improvements in terms of discrimination capability and diffraction efficiency for noisy input object, cluttered object, multi-target environment, etc.. The technique can also be used in fringe binarization as a pre-binarization processing, which would ease the problem of determining the proper threshold level that decreases the risk of faulty correlation peaks.

Acknowledgement

We acknowledge the support of the US Army Missile Command through the US Army Research Office under contract DAAL03-87-0147.

* Professor Pedro Andres was taking sabbatical leave from Departamento de Optica, Facultad de Fisicas, Universidad de Valencia, Valencia, Spain.

References

[1] C.S. Weaver and J.W. Goodman,"Technique for optically convolving two functions," Appl. Opt. **5**, 1248-1249 (1966)

[2] F.T.S.Yu and X.J.Lu,"A realtime programmable joint transform correlator," Opt. Commun., **52**, 10-20 (1984)

[3] F.T.S.Yu, S. Jutamulia, and T.Lin and D.A. Gregory,"Adaptive realtime pattern recognition using liquid crystal TV based joint transform correlator," Appl. Opt. **26**, 1370-1372 (1987)

[4] J. Florence,"Joint transform correlator system using deformable mirror spatial light modulator," Opt. Lett. **14**, 341-343 (1989)

[5] F.T.S. Yu, F. Cheng, and T. Negata,"Effect of fringe binarization of multiobject joint transform correlation," Appl.Opt., **28**, 2988-2990 (1989)

[6] J.A. Davis, E.A. Merrill, D.M. Cotrell and R.M. Bunch, "Effects of sampling and binarization in the output of the joint transform correlator," Opt. Eng.,**29**, 1094-1100 (1990)

[7] Ying Sun, Zhao-Qi Wang, and Guo-Guang Mu,"Amplitude compensated matched filters using circular harmonic expansion and a Mellin transform," Appl. Opt., **29**, 4779-4783 (1990)

[8] B.V.K.V. Kumar and L. Hassebrook,"Performance measures for correlation filters," Appl.Opt., **29**, 2997-3006 (1990)

[9] B.V.K.V. Kumar, W. Shi and C. Hendrix,"Phase-only filters with maximally sharp correlation peaks," Opt. Lett., **15**,807-809 (1990)

[10] J.L. Horner,"Light utilization in optical correlation," Appl. Opt., **21**, 4511-4514 (1982)

[11] O.K. Ersoy and M. Zeng,"Nonlinear matched filtering," J.Opt.Soc.Am.A, **6**, 636-648 (1989)

Figure Captions

Fig.1 An optical joint transform correlator

Fig.2(a) Input object and reference functions

(b) Correlation output produced by CJTC

(c) Correlation output produced by BICF JTC

Fig.3(a) Input object cluttered by a shuttle image

(b) Correlation output produced by CJTC

(c) Correlation output produced by TICF JTC

Fig.4(a) Input object embedded in additive white Gaussian noise

(b) Correlation output produced by CJTC

(c) Correlation output produced by TICF JTC

(d) Correlation output produced by MMSE ICF JTC

Fig.5(a) Multi-object and multi-reference functions

(b) Correlation output produced by CJTC

(c) Correlation output produced by TICF JTC

Fig.6(a) PBR as a function of MMSE bias ratio

(b) PBR as a function of TICF threshold ratio

Fig.7(a) PBR as a function of input SNR

(b) PDE as a function of input SNR

Fig.8(a) PBR as a function of binarization threshold ratio

(b) PDE as a function of binarization threshold ratio

(c) PBR after TICF compensation

(d) PDE after TICF compensation

Fig.9(a) PBR as a function of TICF threshold ratio for fringe binarization

(b) PDE as a function of TICF threshold ratio for fringe binarization

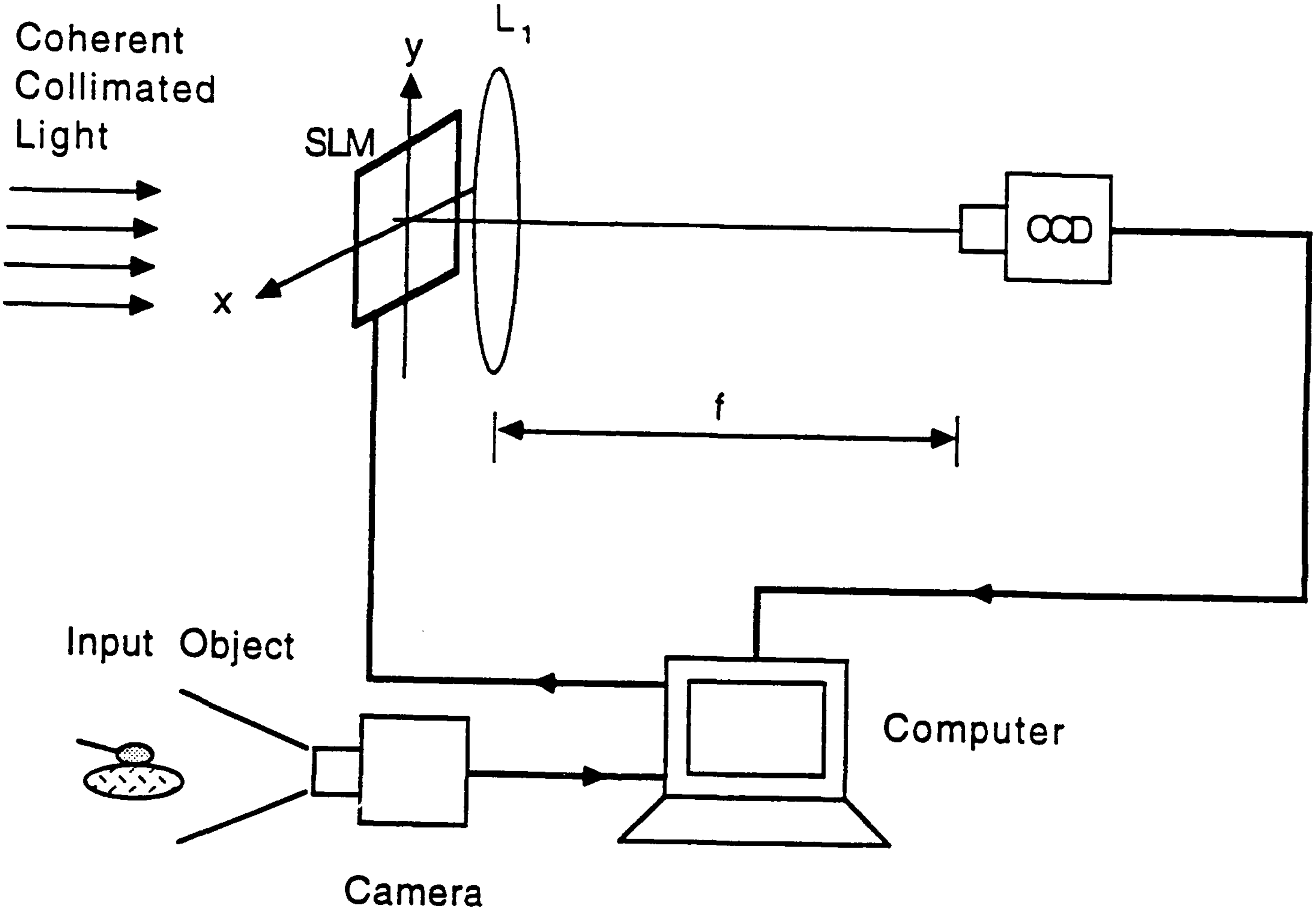
Coherent
Collimated
Light
SLM
y
x
L₁
CCD
f
Input Object
Camera
Computer

Fig 1

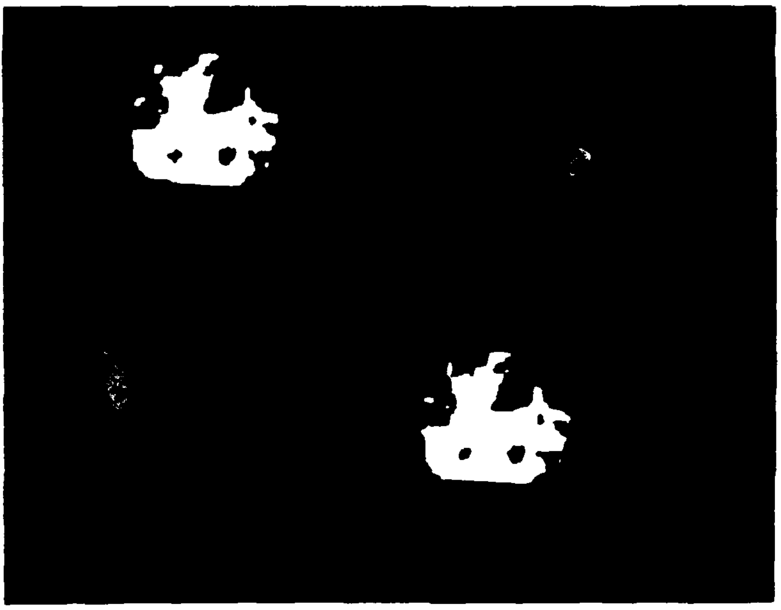

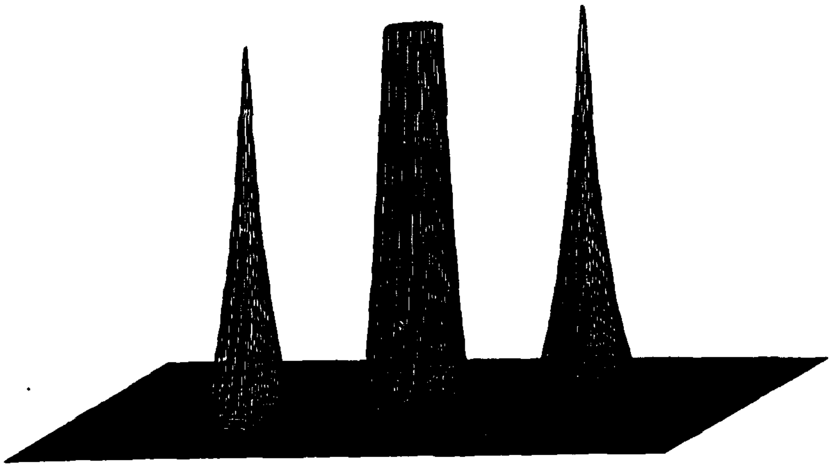

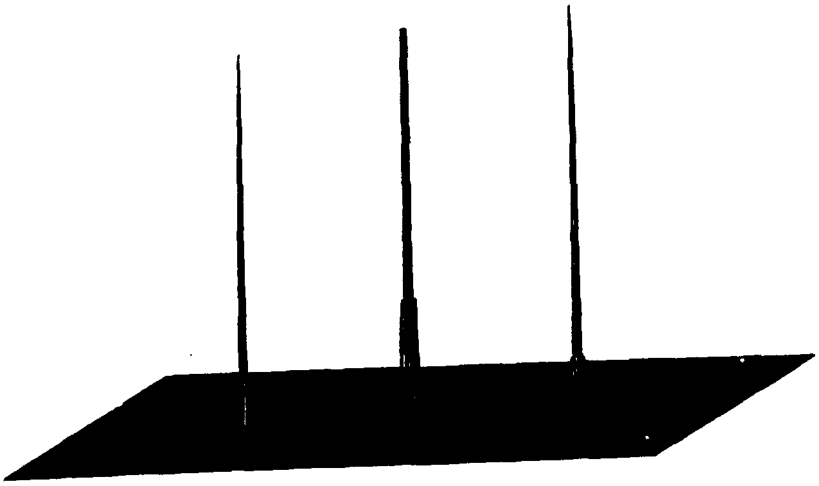

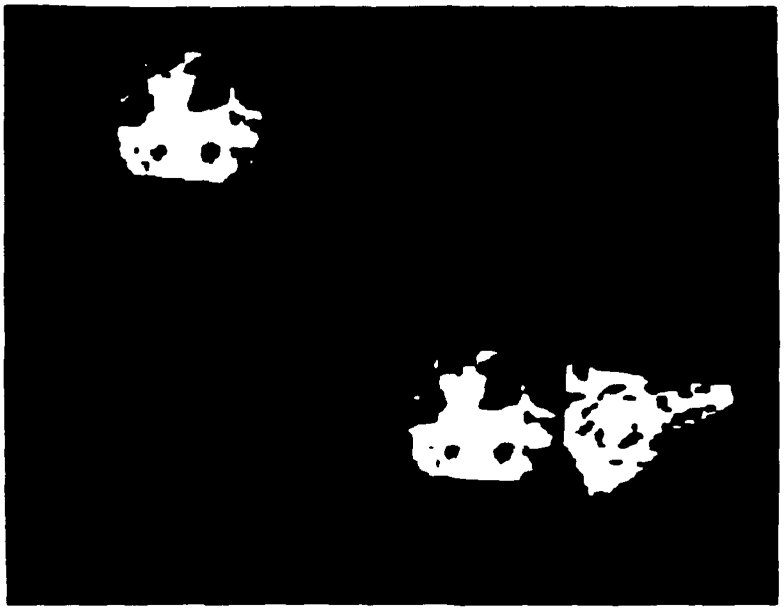

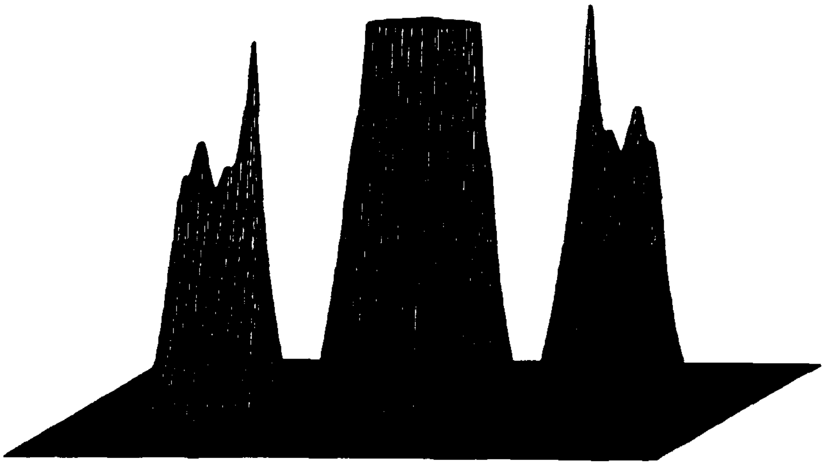

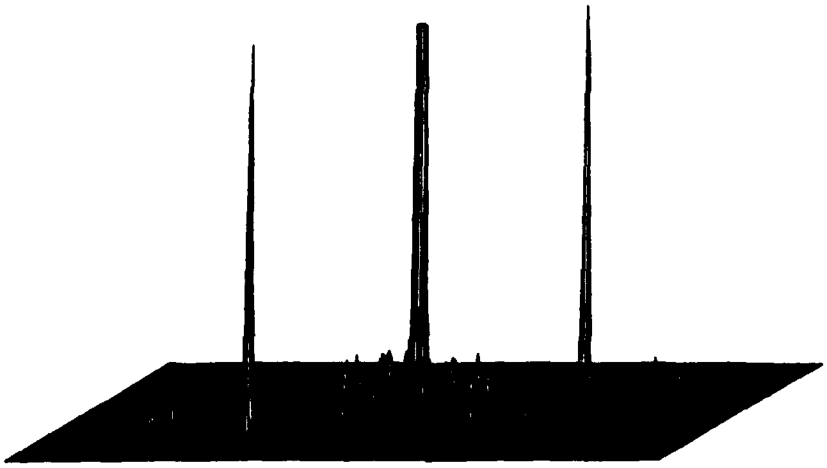

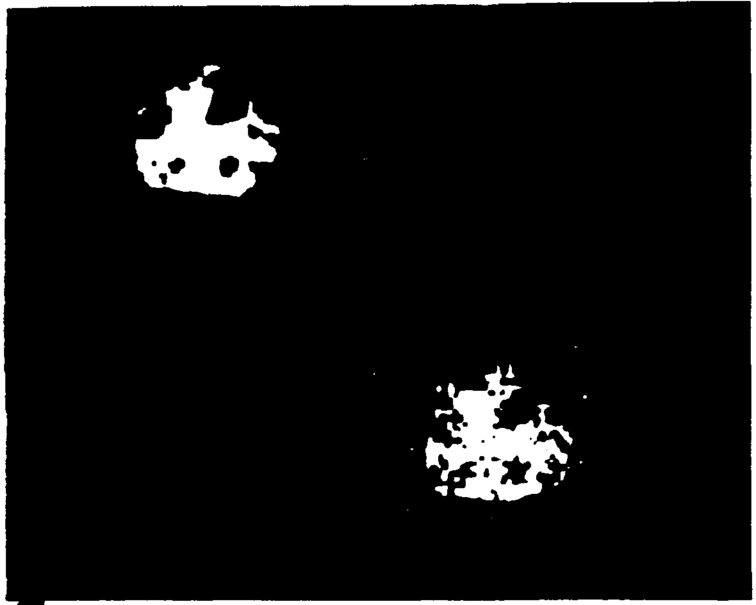

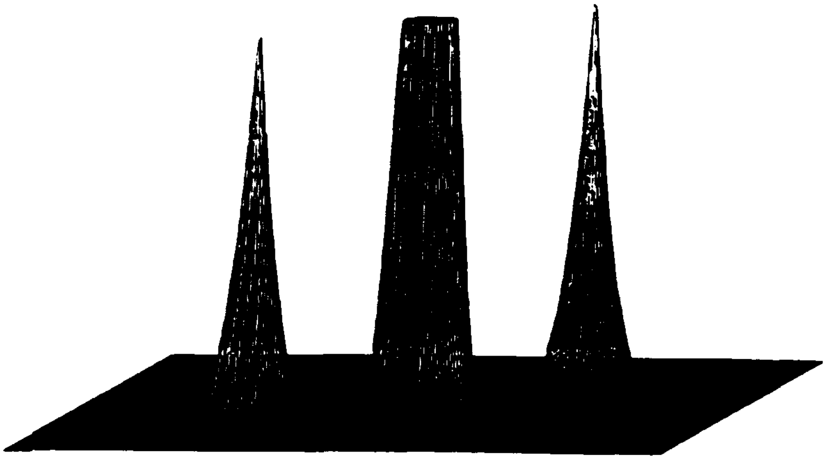

[illegible]

[illegible]

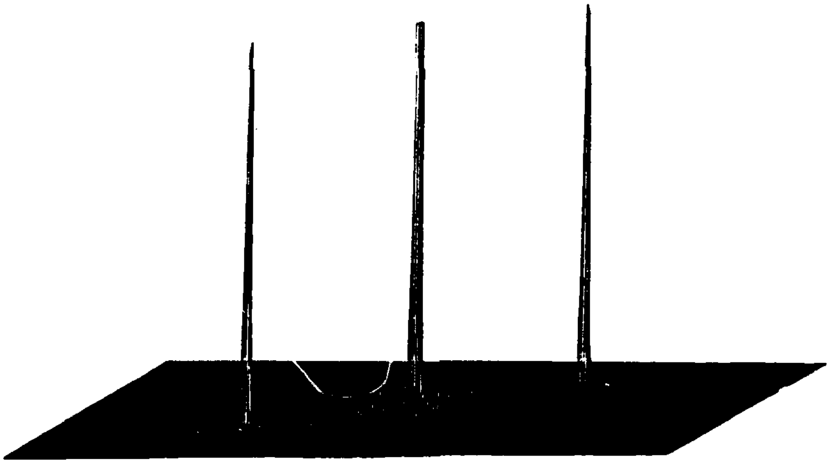

[illegible]

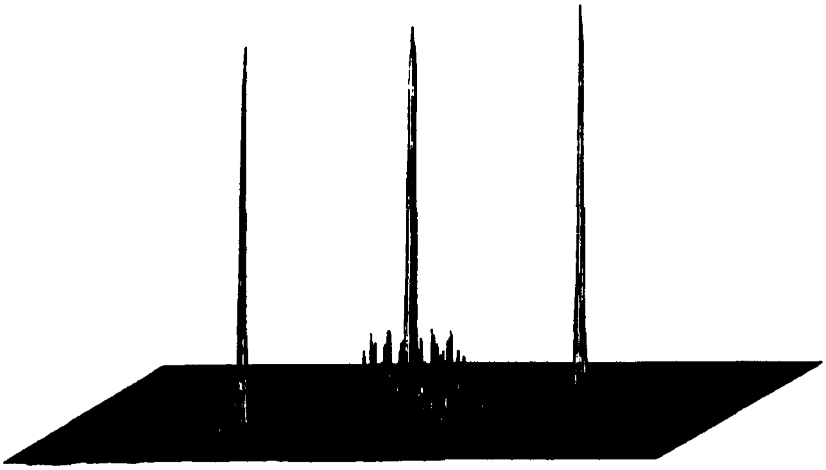

[illegible]

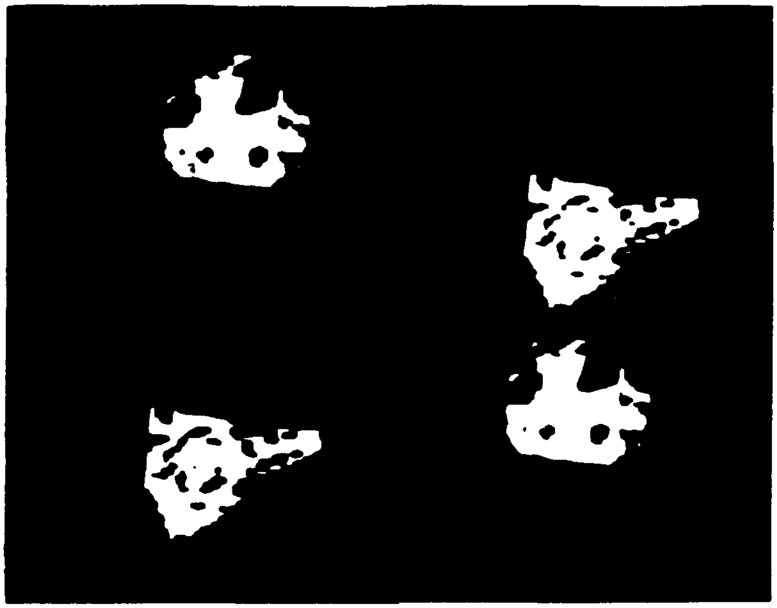

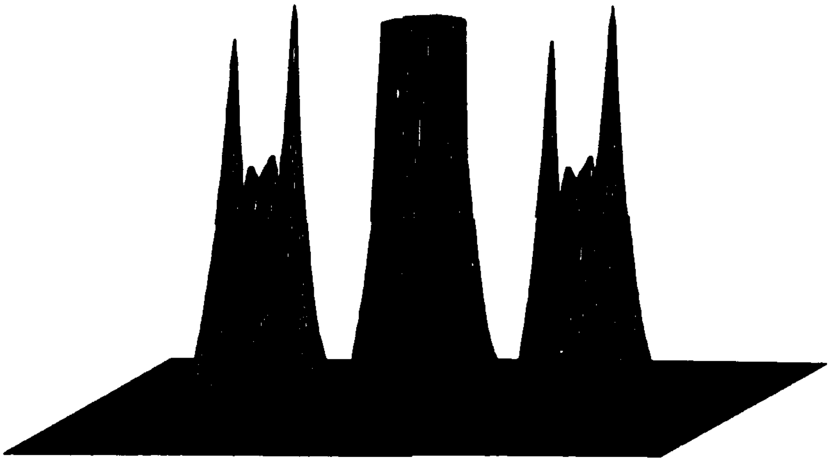

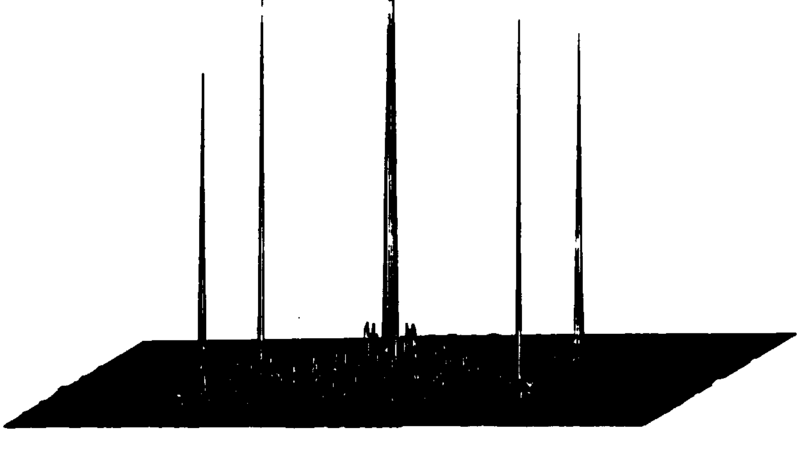

PBR vs. Bias Ratio

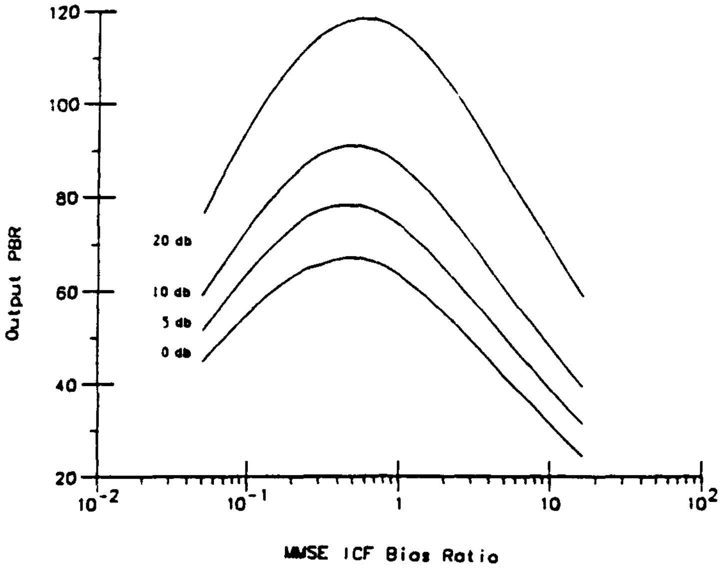

PBR vs. Threshold Ratio

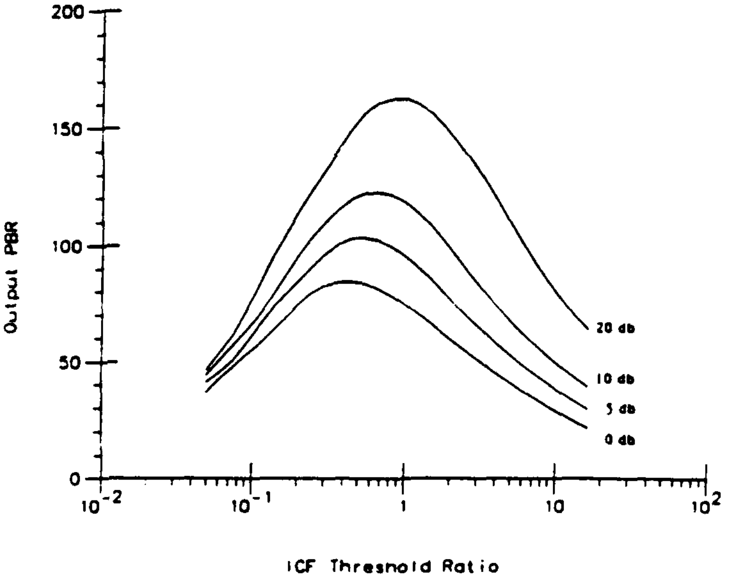

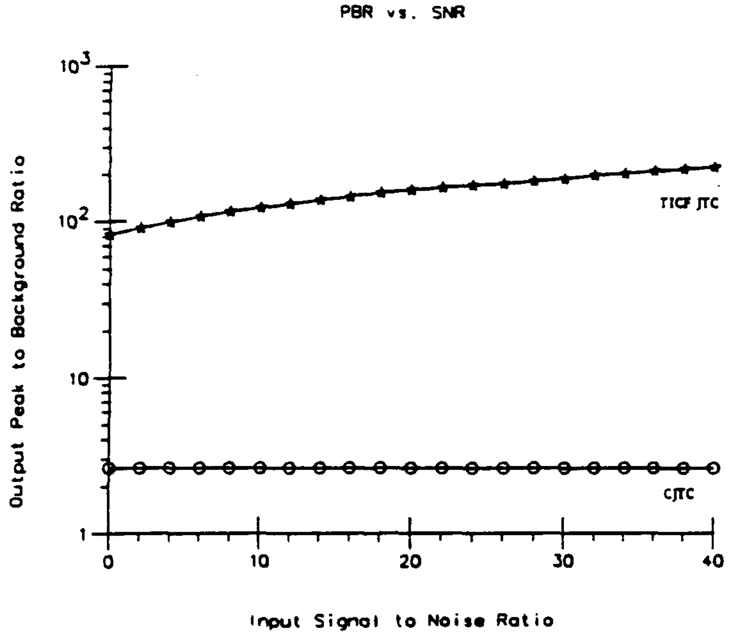

PBR vs. SNR

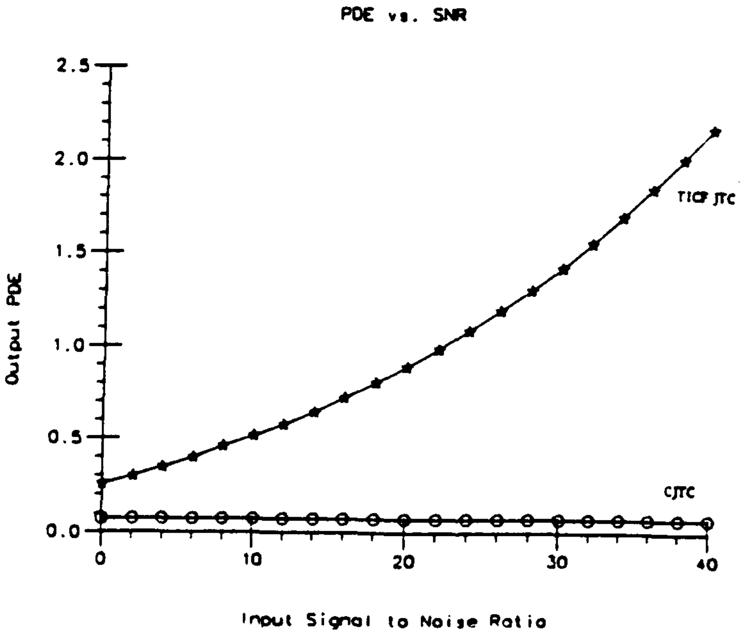

PDE vs. SNR

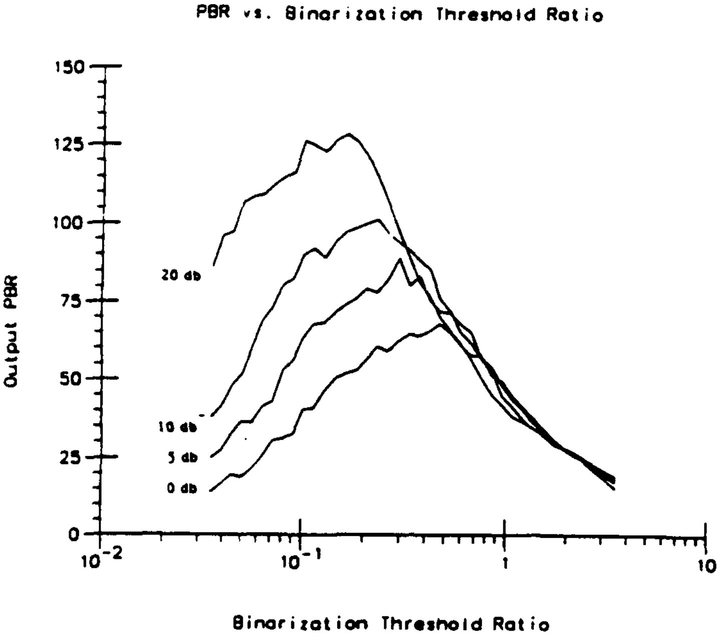
PBR vs. Binarization Threshold Ratio
Output PBR
150
125
100
75
50
25
0
20 db
10 db
5 db
0 db
10^{-2}
10^{-1}
1
10
Binarization Threshold Ratio

Fig. [illegible] (a)

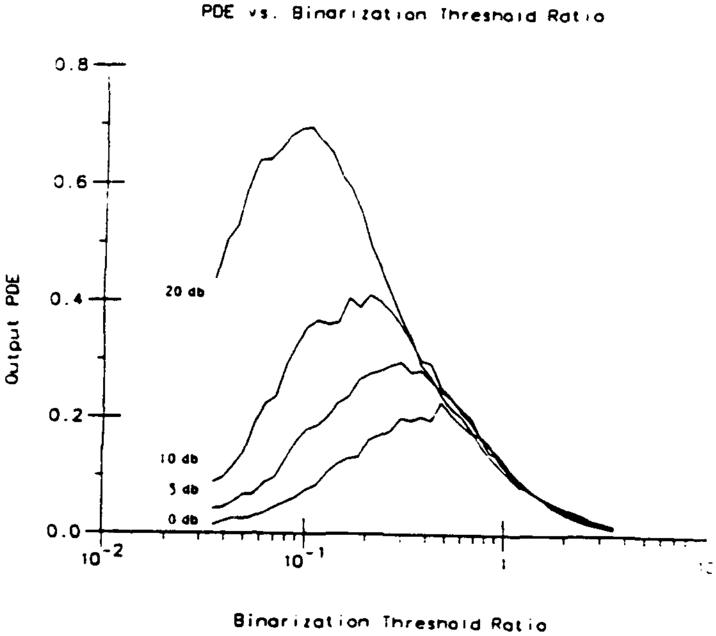
PDE vs. Binarization Threshold Ratio
Output PDE
0.8
0.6
0.4
0.2
0.0
20 db
10 db
5 db
0 db
10^{-2}
10^{-1}
1
10
Binarization Threshold Ratio

[illegible] (b)

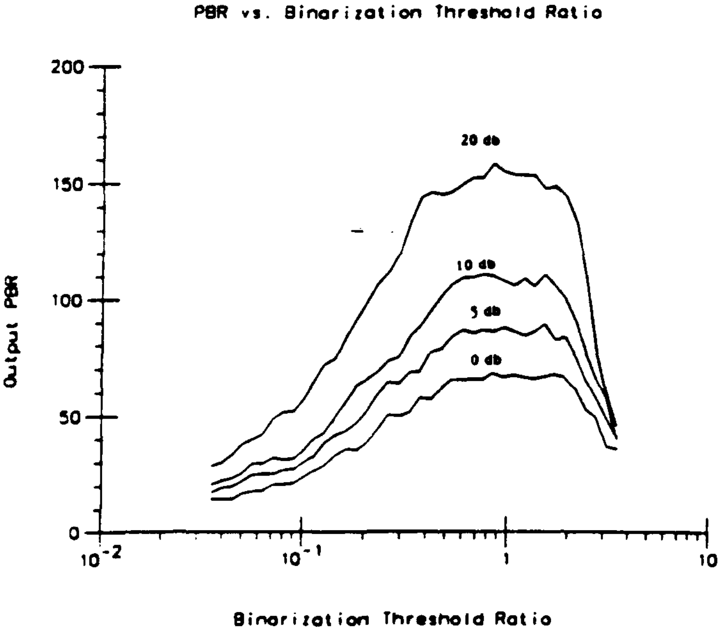
PBR vs. Binarization Threshold Ratio
Output PBR
200
150
100
50
0
20 db
10 db
5 db
0 db
10^{-2}
10^{-1}
1
10
Binarization Threshold Ratio

[illegible] (c)

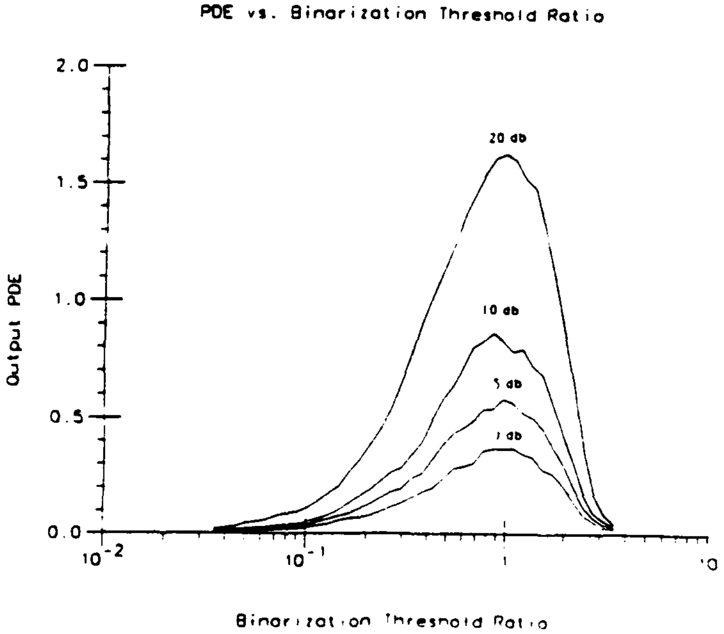
PDE vs. Binarization Threshold Ratio
Output PDE
2.0
1.5
1.0
0.5
0.0
20 db
10 db
5 db
0 db
10^{-2}
10^{-1}
1
10
Binarization Threshold Ratio

[illegible] (d)

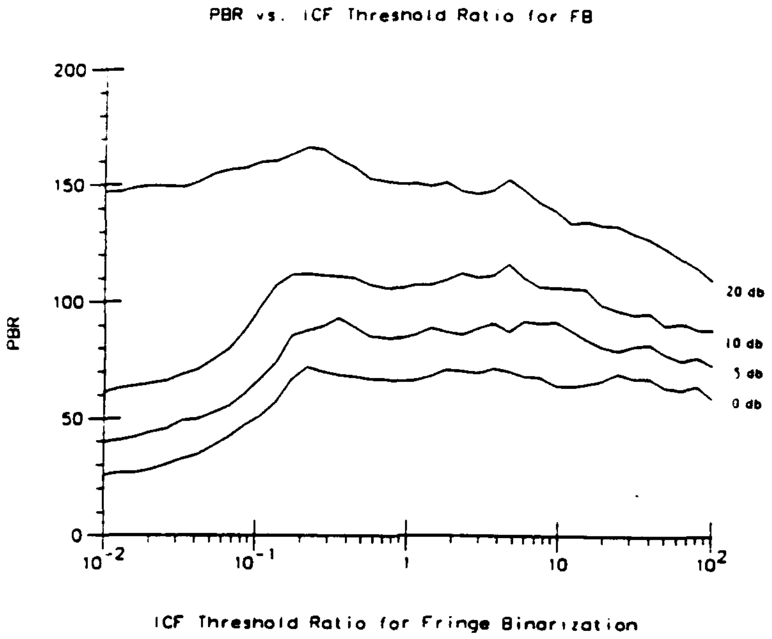
PBR vs. ICF Threshold Ratio for FB
200
150
100
50
0
PBR
20 db
10 db
5 db
0 db
10^{-2}
10^{-1}
1
10
10^{2}
ICF Threshold Ratio for Fringe Binarization

[illegible]

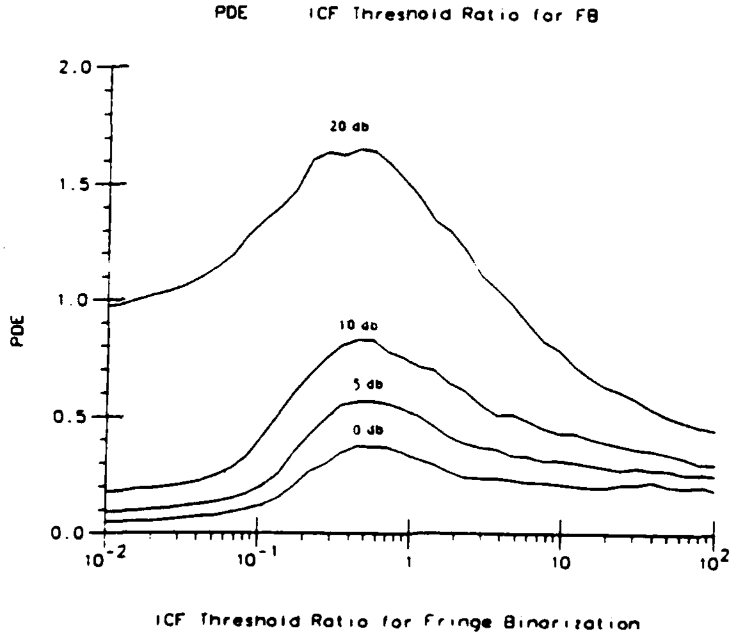
PDE ICF Threshold Ratio for FB
2.0
1.5
1.0
0.5
0.0
PDE
20 db
10 db
5 db
0 db
10^{-2}
10^{-1}
1
10
10^{2}
ICF Threshold Ratio for Fringe Binarization

[illegible]

APPENDIX 10.6

Multi-Target Detection Spatial Synthesis JTC

Multi-target detection using spatial synthesis joint transform correlation

Feng Cheng and Francis T.S. Yu
Penn State University
Dept. of Electrical and Computer Engineering
University Park, PA 16802

Don A. Gregory
US Army Missile Command
Redstone Arsenal, AL 35898-5248

Abstract

A spatial synthesis method to improve accuracy of detection for joint transform multi-target recognition is discussed. The reference function used for the conventional joint transform correlation is replaced by a synthesized function for sharpening correlation profiles without using a filter in Fourier domain. It is shown that the synthesized function can be spatially truncated to fit multiple reference applications and the effectiveness of this technique would not be affected by the number of references. The optical implementation of the synthesized function, effects due to noise disturbance, background cluttering, and spectral fringe binarization are investigated.

I. Introduction

Joint transform correlator offers the advantages of simplicity of alignment and suitable for hybrid-optical processing [1-4]. However, due to heavy DC content of the input target, it also produces relatively broad correlation profiles, which hinders the application to multi-target detection. Although this problem can be solved by using an intensity compensation filter (ICF), it is generally limited for single reference problem [5]. Nevertheless, this problem can be alleviated if a spatial function, whose Fourier transform (FT) is equivalent to the FT of the reference multiplied by the ICF can be synthesized.

In this paper, we shall discuss the applicability of this technique for multi-target recognition, for which a detail will be given and the implementation of the spatial synthesis will be provided.

II. Spatial Synthesis

A single SLM JTC is shown in Fig.1, in which the input patterns and the joint transform power spectrum (JTPS) can be alternatively addressed and displayed using a microcomputer [3][6]. As it is well known for a conventional JTC, a pattern f(x,y) is provided as the reference function for correlation with respect to an input object function o(x,y). It is trivial that, if the input object function matches the reference function, i.e. o(x,y)=f(x,y), a set of autocorrelation peaks can be detected at the correlation output. However, due to the broad profile of the correlation distributions, low accuracy of detection would generally occur, and therefore a new reference function r(x,y) should be synthesized in place of the conventional reference function f(x,y) to obtain sharper correlation profiles. Let us first set o(x,y)=f(x,y) to evaluate the pattern matched correlation output. We further assume that the input object function f(x,y) and the synthesized reference function r(x,y) are placed at x=+b and x=-b, respectively in the input plane, by which the amplitude transmittance t(x,y) is written as

$$t(x,y)= f(x-b,y) + r(x+b,y). \tag{1}$$

The corresponding joint Fourier transform is

$$T(p,q) =F(p,q) \exp(-jbp) + R(p,q) \exp(jbp), \tag{2}$$

and the JTPS is given as

$$| T |^2 = | F |^2 + | R |^2 + F R^* \exp(-2jbp) + F^*R \exp(2jbp), \tag{3}$$

where the super asterisk denotes the complex conjugation and (p,q) is the angular spatial frequency coordinate system. It can be seen from Eq.(3) that, if the FT of r(x,y) is given as

$$R(p,q) = K / F^*(p,q), \tag{4}$$

where K is a proportionality constant, the output correlations at $x=\pm 2b$ would become delta functions, which improve the accuracy of detection. Since the left hand side of Eq.(4) is essentially an inverse filter function that can also be written as

$$R(p,q) = K\, F(p,q) \,/\, |\, F(p,q)\, |^2 . \tag{5}$$

In view of the preceding equation, poles may occur if $|F(p,q)|^2$ approaches zero. We note that these poles may be completely removed if the denominator is properly thresholded, that is,

$$R(p,q) = K\, F(p,q) \,/\, T\{\, |\, F(p,q)|^2 \,\}_{Vt} , \tag{6}$$

where T represents thresholding operation and Vt denotes the threshold value which cuts off the lower part of the denominator. Notice that the thresholded denominator is equivalent to the ICF, in which the Vt would play an important role in adjusting the system to fit the input noise conditions [5]. A large threshold value will maintain the noise immunity of the JTC as a conventional optimum correlator. In fact, if Vt is greater than the maximum value of $|F(p,q)|^2$, the system would behave as a conventional JTC, for which it has the highest noise immunity. On the contrary, a small threshold value would produce a sharper correlation profiles as long as the input noise level is relatively low. Nevertheless, the trade-off value for an optimum value of Vt is chosen based on the balance of adequate sharpness of the correlation profiles and sufficient degree of noise tolerance. It has been shown in our previous paper [5] that, when Vt is in the same order of noise intensity, that is

$$Vt \approx \gamma \sigma^2 , \tag{7}$$

the ratio of the correlation peak intensity to the average background intensity [or Peak-to-Background Ratio (PBR)] would be the highest, where γ is a proportionality constant and σ^2 is the input noise variance. Since the spatial synthesis r(x,y) can be regarded as the impulse response of Eq.(6), it can be written as

$$r(x,y) = K\,\mathbf{F}^{-1}\{\,F(p,q)\,/\,T\{\,|F(p,q)|^2\,\}_{Vt}\,\}, \tag{8}$$

where $\mathbf{F}^{-1}$ denotes the inverse transform. In view of this result, we see that the contour of the original pattern f(x,y) would be preserved in the synthesis of Eq.(8), since the phase distribution of the original pattern spectrum F(p,q) remains unaltered during the synthesis process. This effect can be seen in Fig.2, in which a set of synthesized spatial functions that correspond to the original patterns of Fig.2(a) is shown in Fig.2(b). Based on Fig.2(b) a conjecture may be made that the crucial feature for recognizing the input targets must be the edges of the original patterns, which is largely dominated by phase spectrum of the inverse filter. Although the r(x,y) may be infinitely extended, the spatial truncation of the r(x,y) would not significantly affect the correlation operation, as long as the optical window of the truncated r(x,y) is larger than the original reference pattern r(x,y). In the computer simulations, the truncated window of r(x,y) is chosen as the same size as the original f(x,y). Thus the output correlation performance would not be appreciably affected by the truncation, which clears the overlapping problem for using multi-reference functions in the input spatial domain.

Hence, for N reference patterns, $f_i(x,y)$, i=1,2,...,N, we have

$$r_i(x,y) = K_i \mathbf{F}^{-1} \{ F_i(p,q) / T\{ |F_i(p,q)|^2 \}_{Vti} \} , i = 1,2,\ldots,N, \quad (9)$$

where Vti is the threshold value for the ith pattern and K_i is the proportionality constant, which is to maintain its energy level comparable with the others.

III. Optical Implementation

It can be shown that, if the original reference pattern f(x,y) is a real function, the corresponding spatial synthesis r(x,y) is also real regardless of the threshold value. It can be implemented by displaying parts of the function onto an SLM. In fact, r(x,y) can be decomposed into $r_+(x,y)-r_-(x,y)$, where $r_+(x,y)$ and $r_-(x,y)$ are the positive part and negative part of r(x,y) which can be separately displayed on an SLM. Thus the joint transform power spectra of the input object function o(x,y) and $r_+(x,y)$, and o(x,y) and $r_-(x,y)$ can be captured by the CCD in the respective steps. The joint spectra of the object and the reference functions, O*R and OR*, can be obtained, by subtracting this pair of JTPS's with a microcomputer, as given as

$$T = \{ |O|^2 + |R_+|^2 + O R_+^* \exp(-2jbp) + O^* R_+ \exp(2jbp) \} -$$

$$\{ |O|^2 + |R_-|^2 + O R_-^* \exp(-2jbp) + O^* R_- \exp(2jbp)$$

$$= O(R_+^* - R_-^*)\exp(-2jbp) + O^*(R_+ - R_-)\exp(2jbp) + |R_+|^2 - |R_-|^2$$

$$= OR^*\exp(-2jbp) + O^*R \exp(2jbp) + |R_+|^2 - |R_-|^2 . \qquad (10)$$

It is trivial that the correlation distributions can be seen around $x=\pm 2b$.

Notice that the spectra content $|R_+|^2 - |R_-|^2$ can be pre-obtained in the initialization stage and, by subtracting it from Eq.(10) with the computer, the unwanted content [i.e., the last two terms in Eq.(10)] can be completely removed.

IV. Simulated Results

Simulations for spatial synthesis and conventional JTC are provided, in which a VAX machine of 256X256 picture frame is used. Four patterns and the spatial synthesis r(x,y) are shown in Fig.2(a) and (b) respectively, in which each pattern in r(x,y) is truncated to the same window size as the original pattern in f(x,y). The positive and the negative parts of the r(x,y) are shown in Figs.2(c) and (d) respectively.

We shall use the set of the original patterns f(x,y) and the set of the synthesized functions r(x,y) as the reference functions respectively for joint transform correlations. First let us correlate with respect to the input object of Fig.3(a). For simplicity the zero order diffraction will be disregarded in the simulations. The output correlation obtained with the conventional joint transform [i.e., using Fig.2(a) as the reference functions] is shown in Fig.3(b), in which we see that the correlation distributions are severely overlapped. Thus it produces lower accuracy of detection. On the other hand, Fig.3(c) shows the output correlation of Fig.3(a) with respect to spatially synthesized r(x,y). In this result, a pair of distinctive the joint transform correlation peaks can be identified, which produces a higher accuracy of detection.

Let us now demonstrate for the multi-object detection. Figure 4(a) shows a set of input objects which are to be joint transform correlated with respect to the set of reference functions f(x,y) of Fig.2(a) and the spatially synthesized r(x,y) of Fig.2(b). The corresponding output correlation with respect to f(x,y) and r(x,y) are provided in Figs.4(b) and (c) respectively, from which we see that the spatial synthesis technique performs better. The locations and the correlation peaks can be easily identified using the spatially synthesized functions r(x,y).

To further demonstrate the performance under noisy condition, we assume that the input object of Fig.3(a) is embedded in an additive random noise shown in Fig.5(a). The output correlations using the conventional reference functions of Fig.2(a) and the spatially synthesized function of Fig.2(b) are provided in Figs.5(b) and (c). Once again we show that the spatially synthesized r(x,y) offers better signal discrimination under noisy environment. Mention must be made that the sharpness of the correlation profile depends on the threshold value of Vt in Eq.(8). By choosing a sufficiently large value of Vt under the constraint of Eq.(7), an optimum peak-to-background ratio can be obtained under a noisy environment.

To investigate the effects due to cluttering and complicated background scene, Fig.6(a) is used as the input object. The simulated result using the conventional joint transform correlation is shown in Fig.6(b) and the one with spatial synthesis method is provided in Fig.6(c). In view of these results, we see that the one using conventional joint transform correlation suffers a large degree of ambiguity, while the spatial synthesis method offers a better performance, in which all the matched correlation peaks can be identified. Another interesting investigation is to compare the correlation performances using the fringe binarization of the JTPS for conventional and synthesis methods. First, we have used a constant threshold value for binarizing the JTPS of the conventional joint transform. Due to large dynamic range of the JTPS, a constant threshold value occasionally produces low quality binarized JTPS. Notice that, by trial and error, a compromised threshold level can be found. If the synthesis method is used, a convenient way to improve the binarized output is to first purge the power spectra of the reference and the object functions (as discussed in the end of section III), and then apply the constant thresholding method using the mean of purged JTPS as the threshold value. The output correlation results using the conventional

and synthesis methods are given in Figs.6(d) and (e) respectively. From these figures, we see that there is a miss and a false alarm using the conventional JTPS fringe binarization method as indicated in the figure. On the other hand, the spatial synthesis technique avoids using the tedious trial and error method in finding a suitable threshold value and apparently offers a better performance.

V. Concluding Remarks

The most frequently used correlation peak sharpening techniques for a single reference correlator require Fourier domain filtering to accentuate certain frequency contents of the reference spectrum. Strictly speaking, each reference function requires a unique filter for the accentuation purpose. However, these techniques are occasionally inapplicable for multiple reference joint transform correlations, since the reference spectra are only using one composite filter. The efficiency and effectiveness of applying multi-reference filtering technique would substantially reduce as the number of the reference patterns increases.

We have shown that the spatial synthesis technique can be applied for multi-reference functions, since it synthesizes a finite sized spatial impulse response as a substitute for the reference pattern used for the conventional joint transform correlation. And the spatially synthesized reference functions can be easily implemented with a current state-of-the-art SLM, e.g., LCTV, by using a two-step sign decomposition technique. We have further demonstrated by choosing a proper threshold level, the spatial synthesis joint transform correlation can be fit for different input object conditions, e.g. noise, cluttering, etc.. Comparison of the performance between the conventional and spatial synthesis techniques are provided. We have shown that the spatial synthesis technique offers a higher signal discrimination for noisy input, cluttering, and spectral fringe binarization.

Acknowledgement

We acknowledge the support of the US Army Missile Command through the US Army Research Office under contract DAAL03-91-0112.

Reference

[1] C.S. Weaver and J.W. Goodman,"Technique for optically convolving two functions," Appl. Opt. **5**, 1248-1249 (1966)

[2] F.T.S. Yu and X.J. Lu,"A realtime programmable joint transform correlator," Opt. Commun., **52**, 10-20 (1984)

[3] F.T.S. Yu, S. Jutamulia, and T. Lin and D.A. Gregory,"Adaptive realtime pattern recognition using liquid crystal TV based joint transform correlator," Appl. Opt. **26**, 1370-1372 (1987)

[4] J. Florence,"Joint transform correlator system using deformable mirror spatial light modulator," Opt. Lett. **14**, 341-343 (1989)

[5] F. Cheng, P. Andres, and F.T.S. Yu,"Intensity compensation filter for joint transform correlation peak enhancement," submitted to Appl. Opt.

[6] E. Tam, F.T.S. Yu, and D. Gregory,"Autonomous real-time objects tracking with an adaptive joint transform correlator,"SPIE vol. 1098, 253-260 (1989)

Figure Captions

Figure 1 A single SLM hybrid optical joint transform correlator

Figure 2 Spatial synthesis

(a) Conventional reference functions f(x,y)

(b) Spatially synthesized reference functions r(x,y)

(c) Positive part of r(x,y)

(d) Negative part of r(x,y)

Figure 3 Accuracy of detection using f(x,y) and r(x,y) respectively

(a) A single truck image as the input object

(b) 2D and 3D output correlation obtained using the conventional joint transform technique [i.e., f(x,y)], in which the zero order diffraction has been disregarded

(c) 2D and 3D output correlation obtained from spatial synthesis method [i.e. r(x,y)]

Figure 4 Multi-target detection

(a) A multi-target input object

(b) Output correlation obtained from the conventional joint transform technique

(c) Output correlation obtained from the spatial synthesis method

Figure 5 Detection under noisy environment

(a) The truck image of Fig.3(a) embedded in an additive white Gaussian noise with SNR=5db

(b) Output correlation obtained from the conventional joint transform technique

(c) Output correlation obtained from the spatial synthesis technique

Figure 6 Detection under cluttering condition

(a) Input object patterns cluttered in a complicated scene

(b) Output correlation obtained from the conventional joint transform technique

(c) Output correlation obtained from the spatial synthesis method

(d) Output correlation obtained from conventional joint transform technique using spectral fringe binarization

(e) Output correlation obtained from the spatial synthesis method using spectral fringe binarization

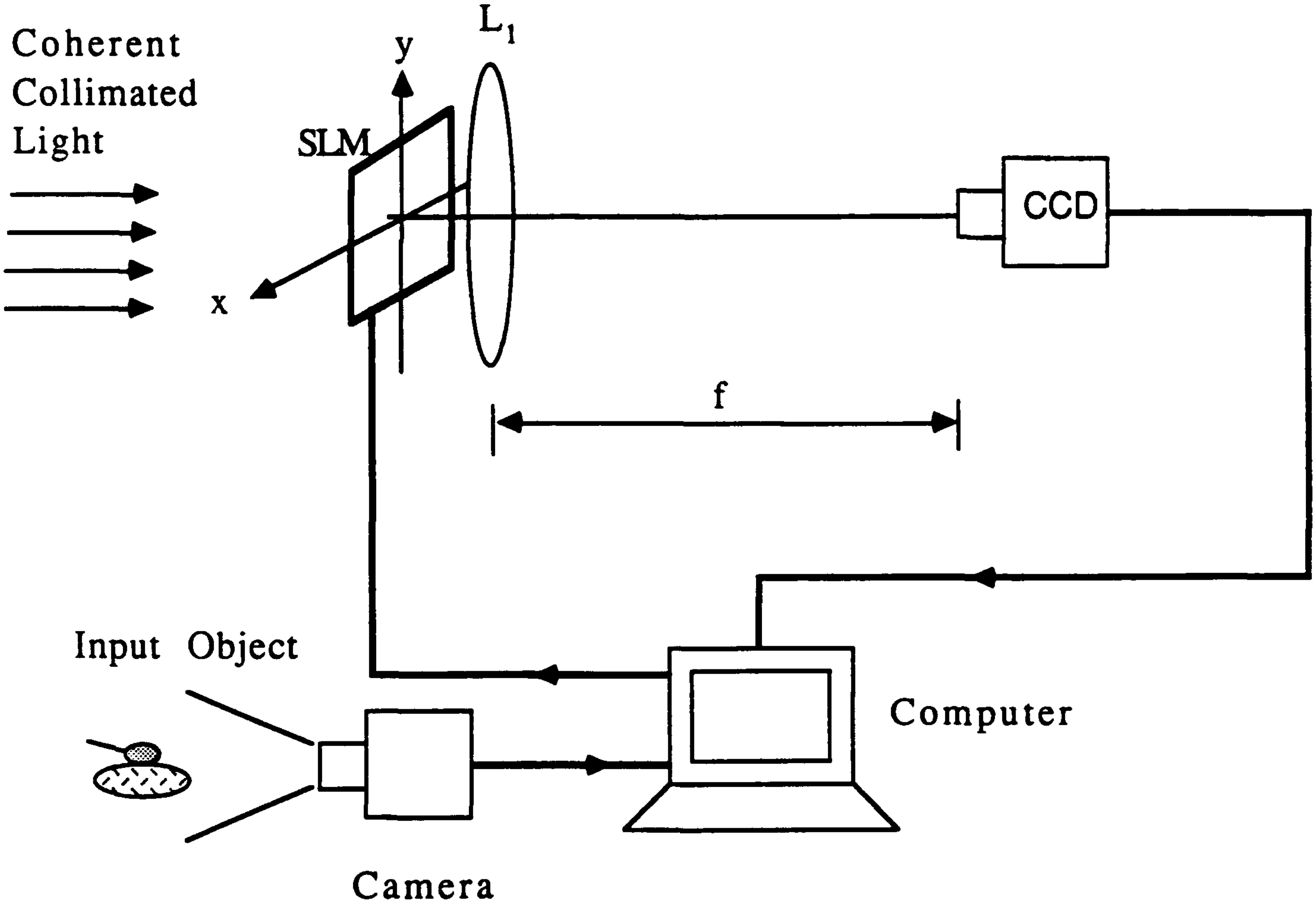
Coherent Collimated Light
SLM
y
x
L$_1$
CCD
f
Input Object
Camera
Computer

Figure 1

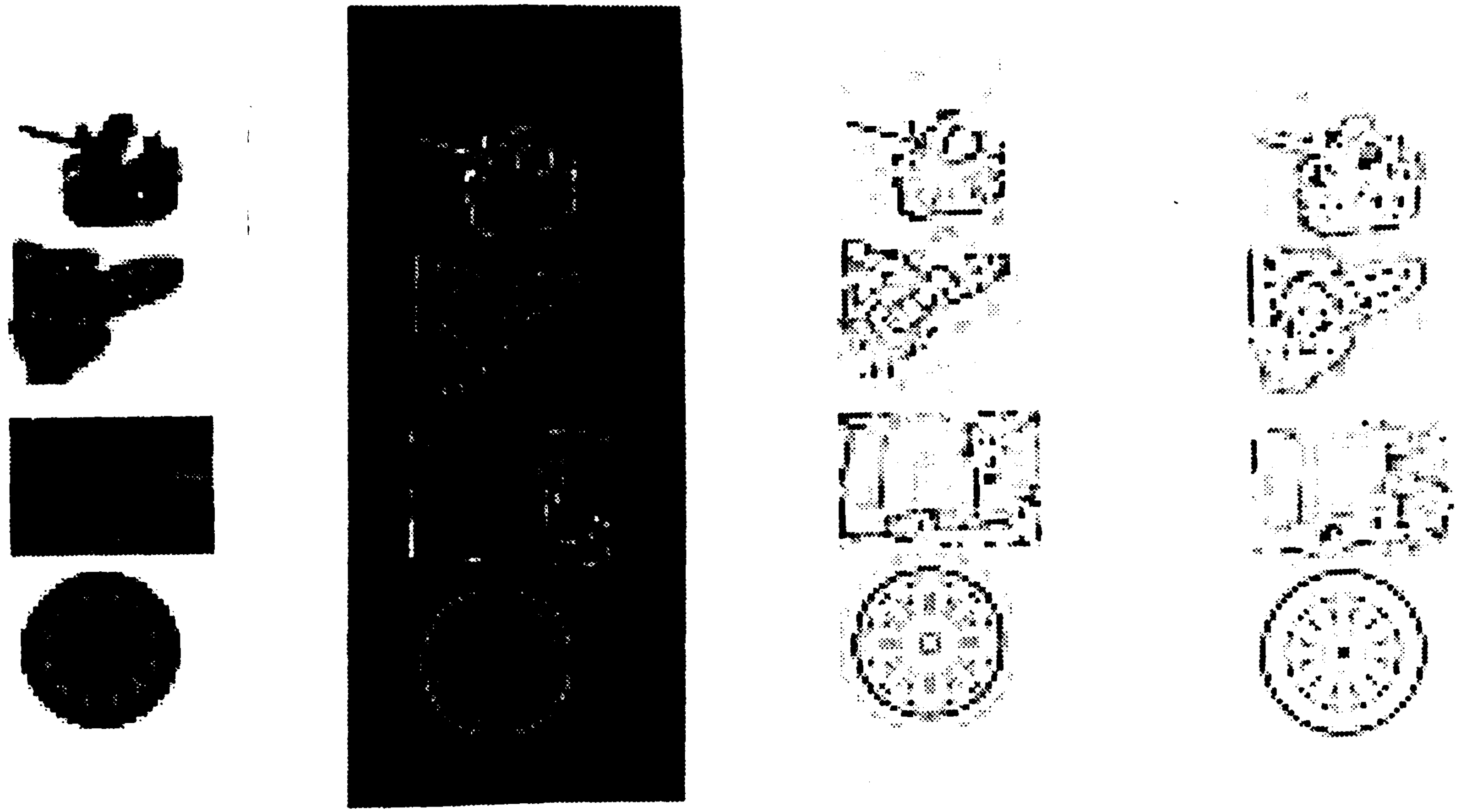

(a) (b) (c) (d)

Figure 2

Figure 3(a)

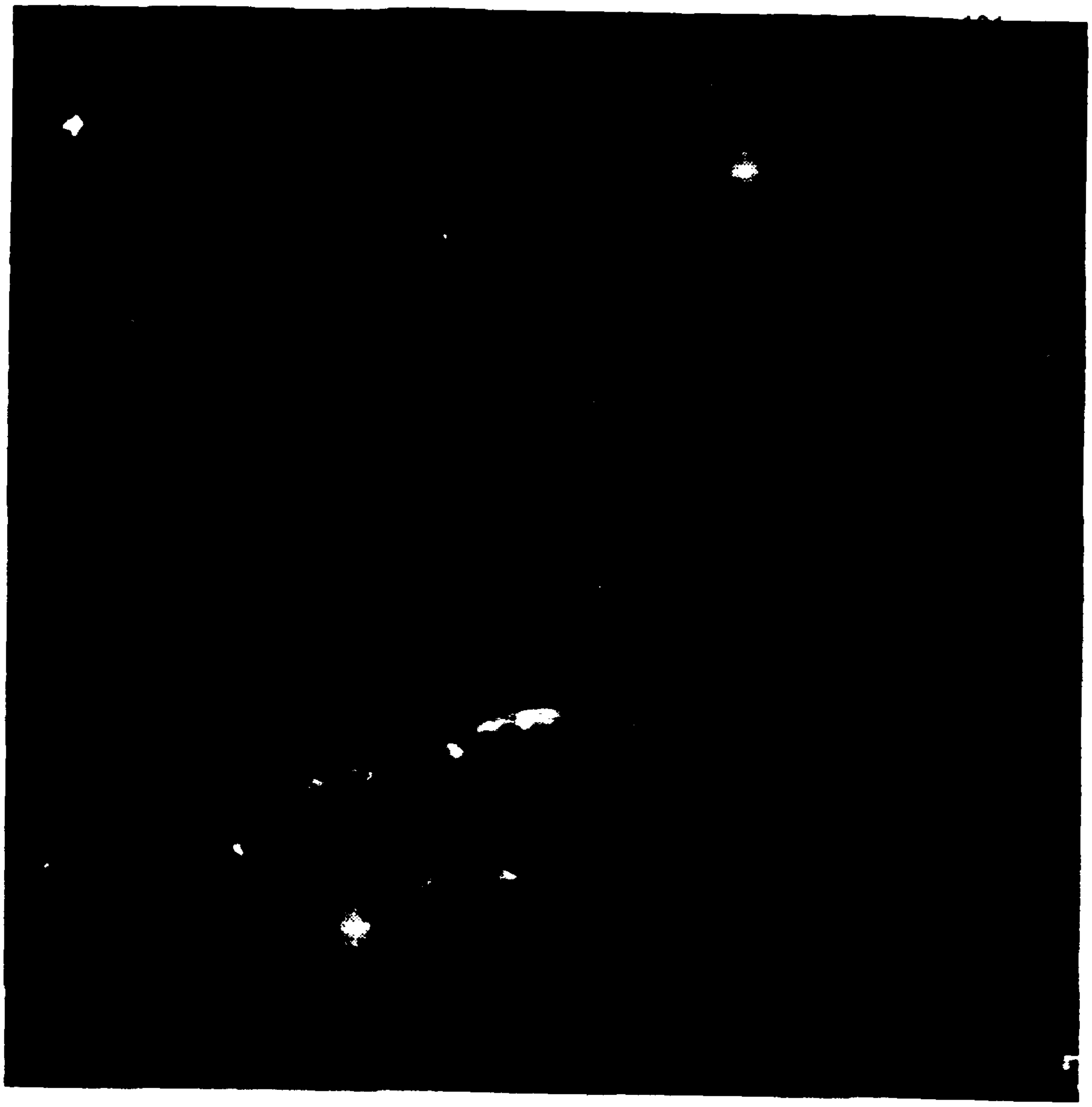

Figure 3(b)

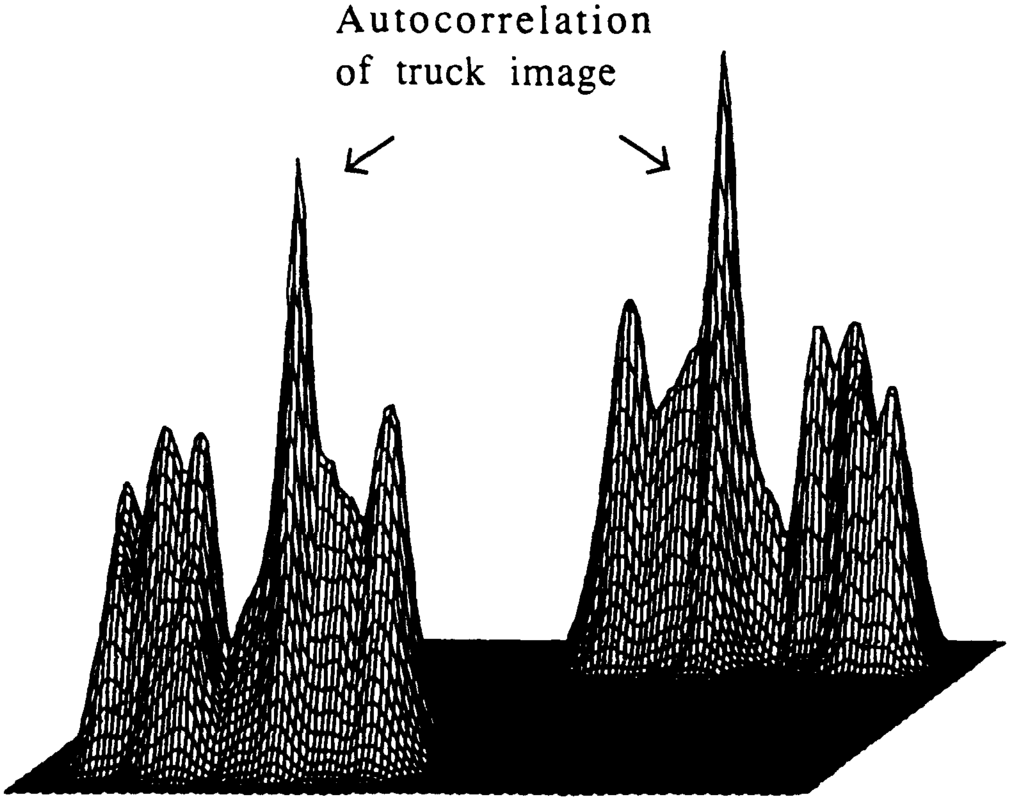

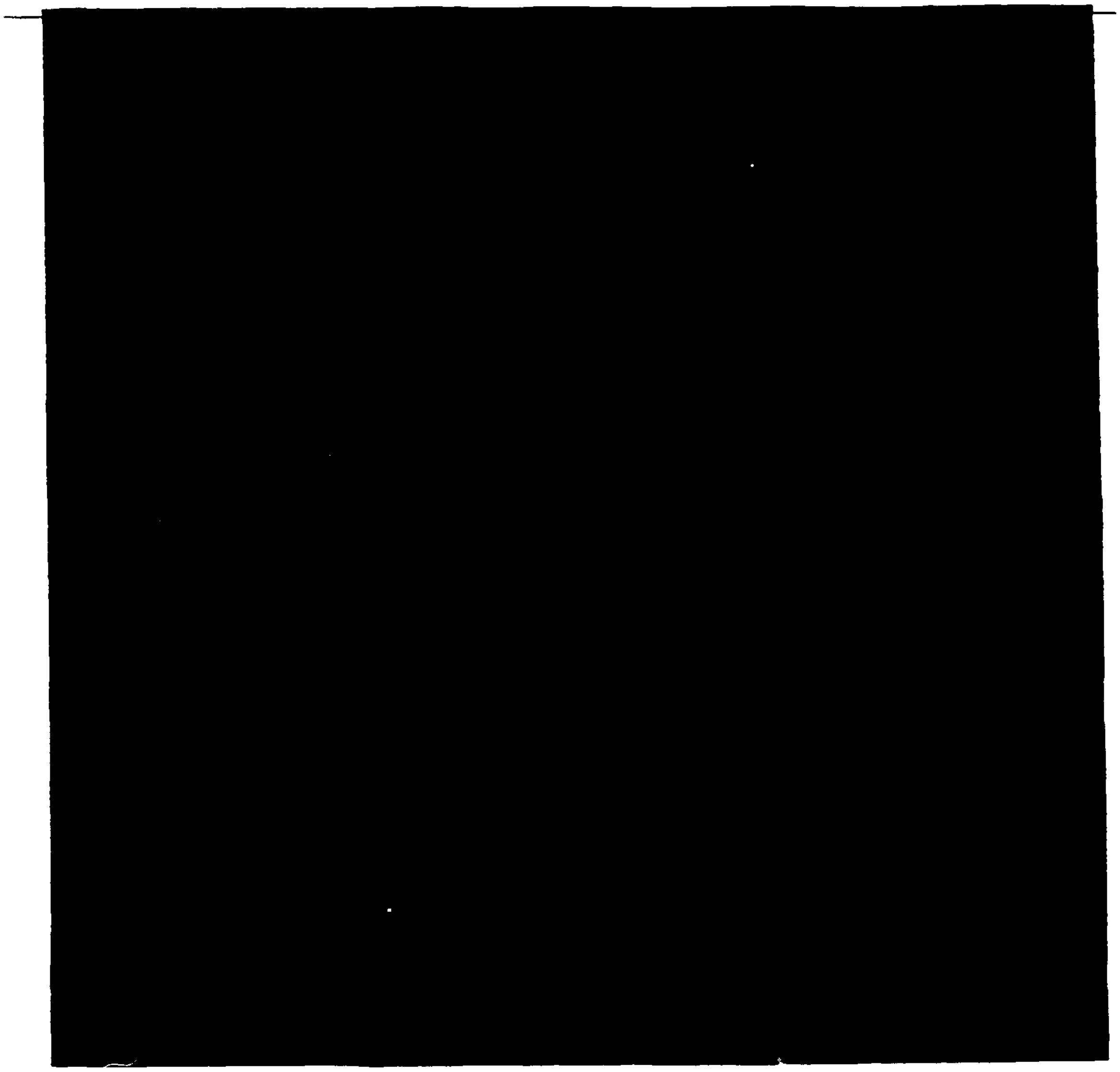

Figure 3(c)

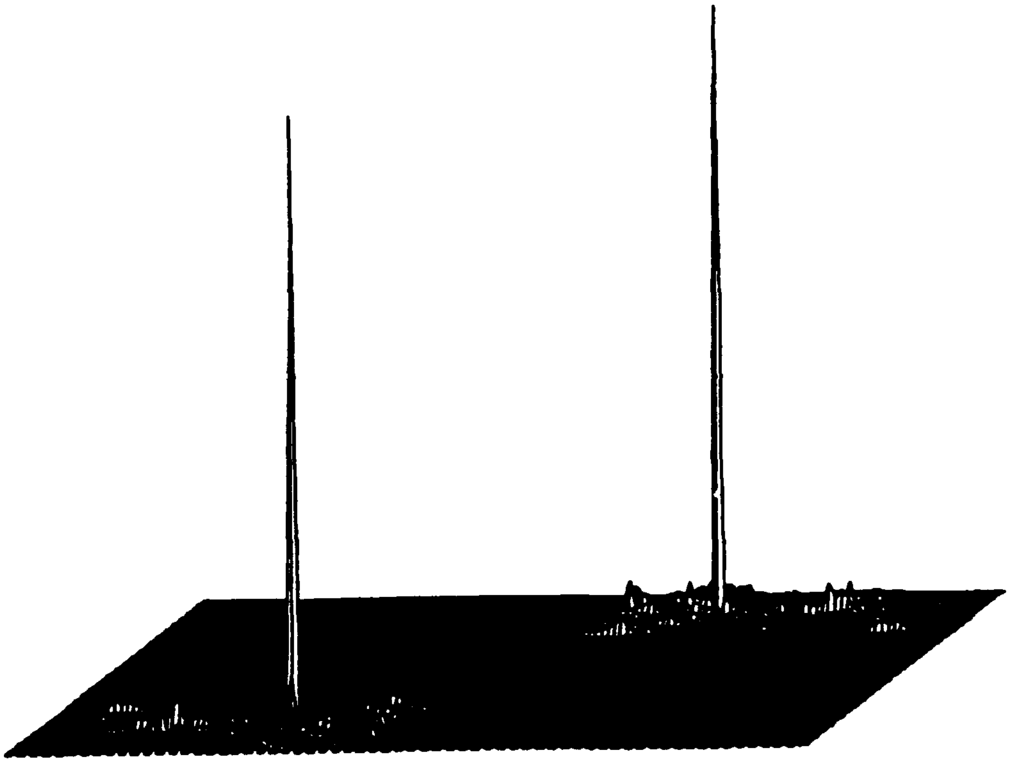

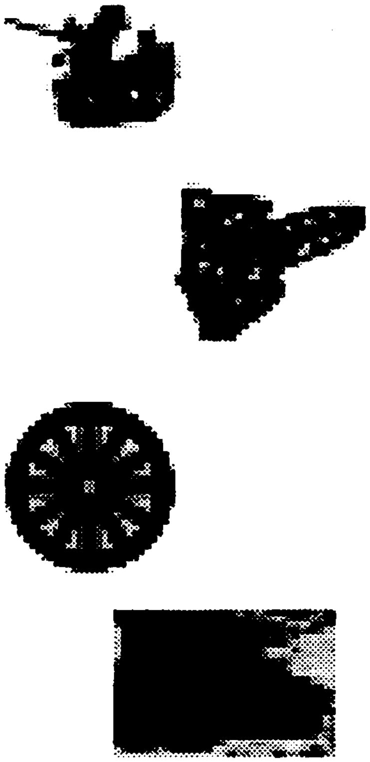

Figure 4(a)

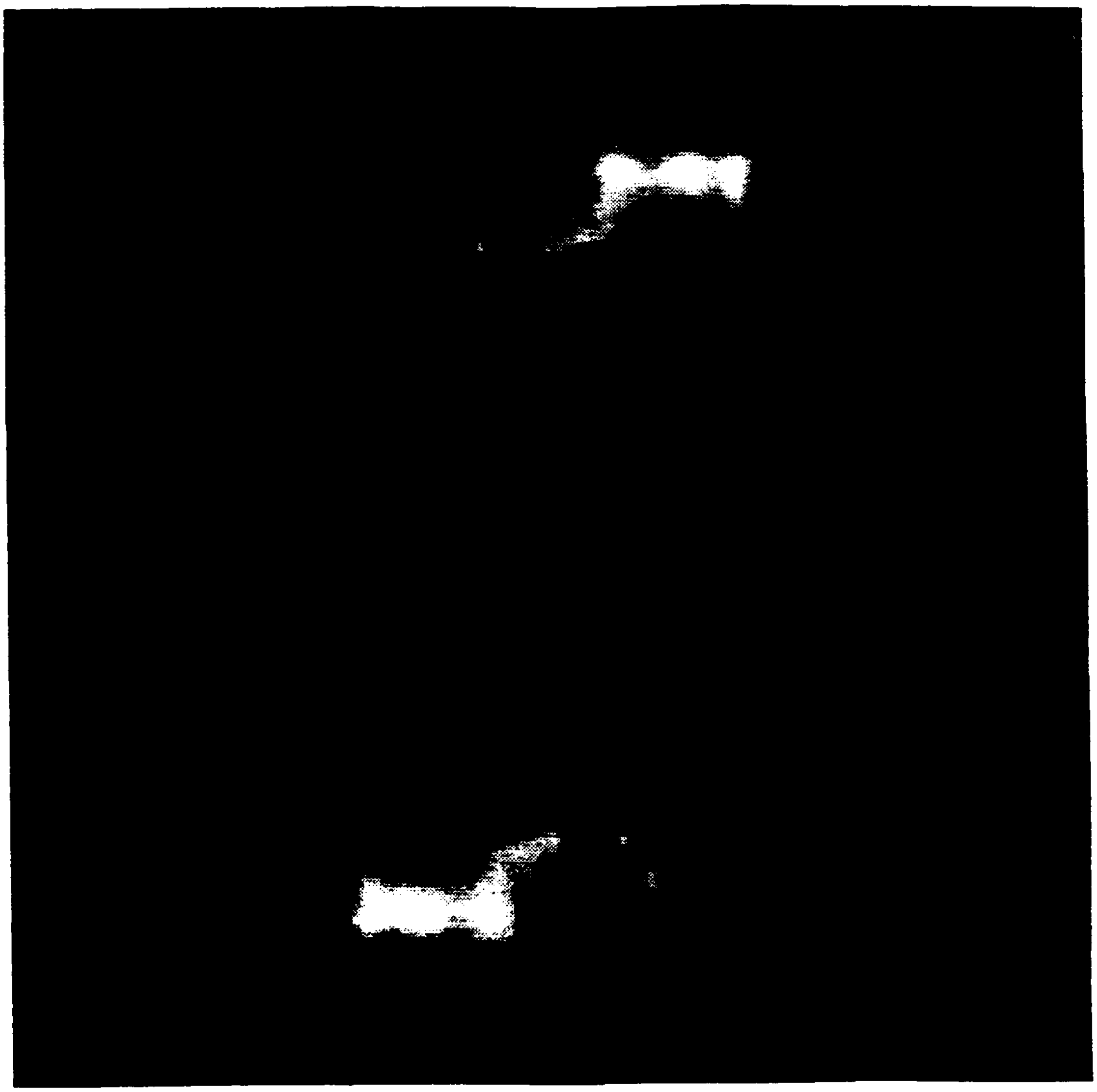

Figure 4(b)

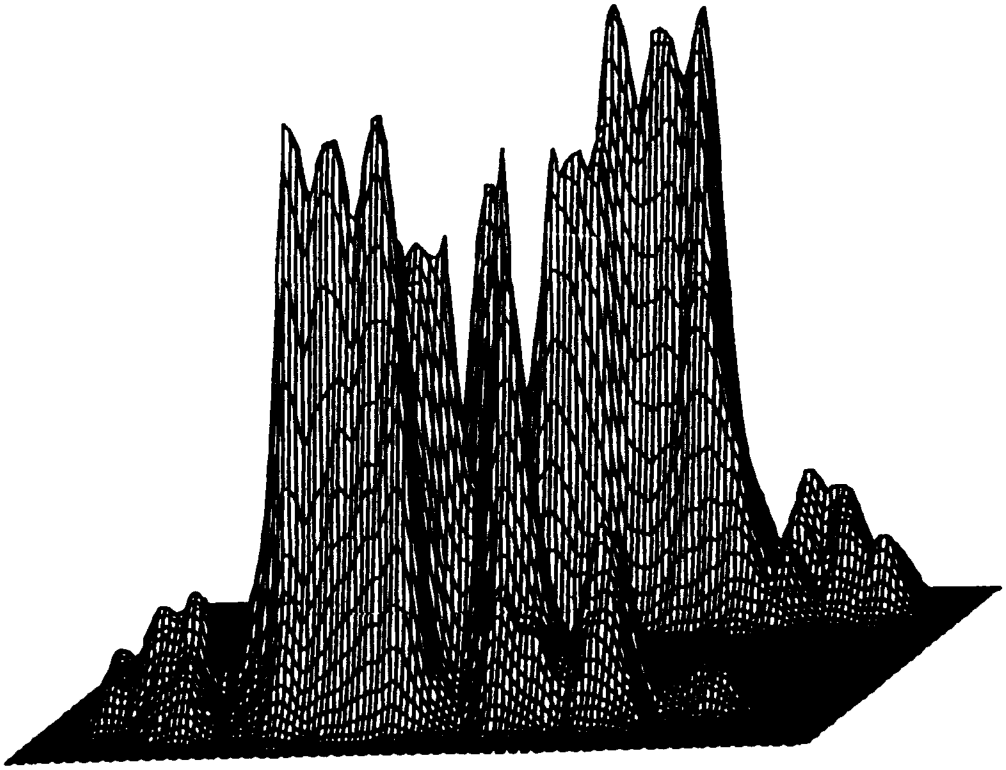

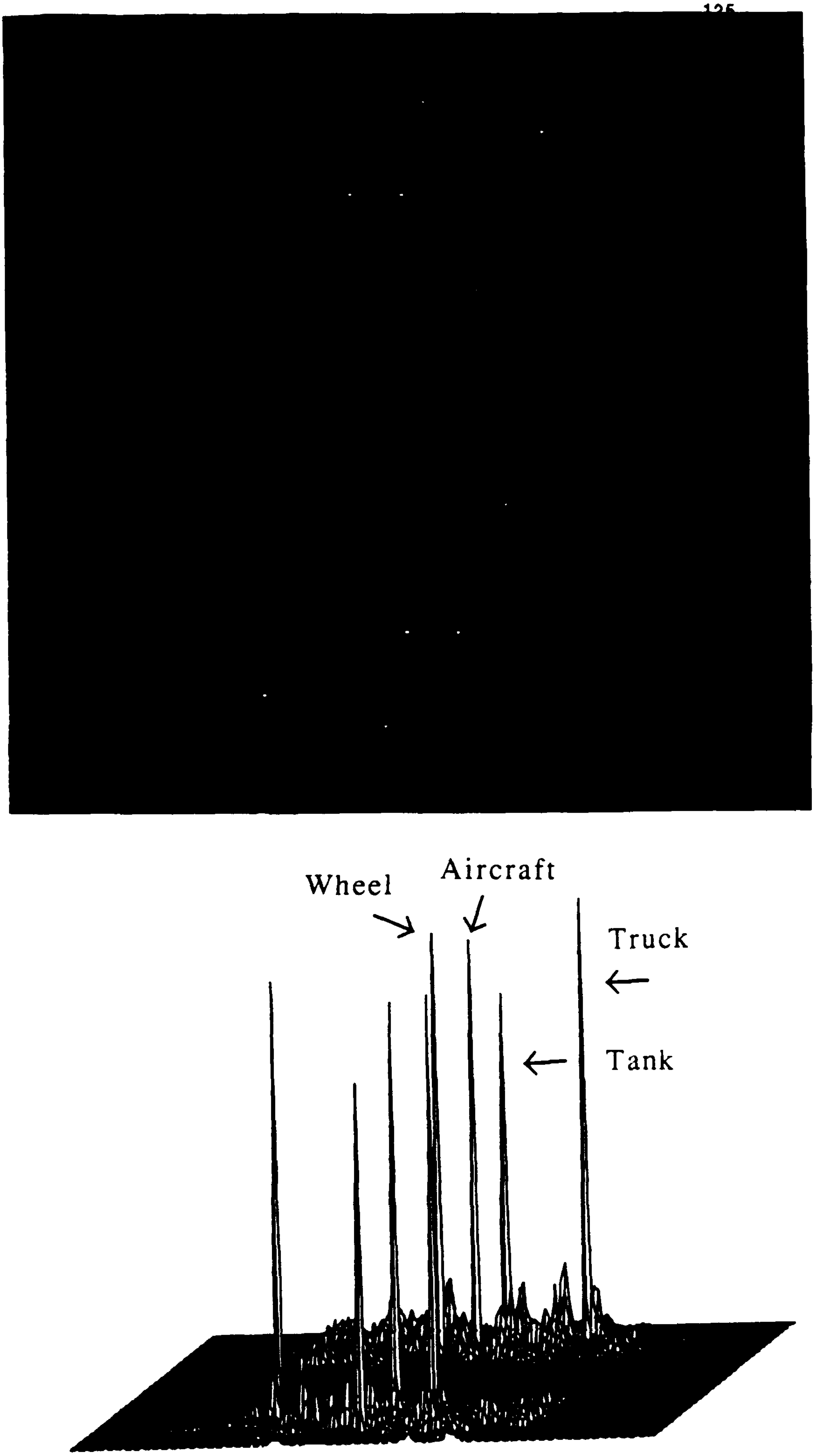

Figure 4(c)

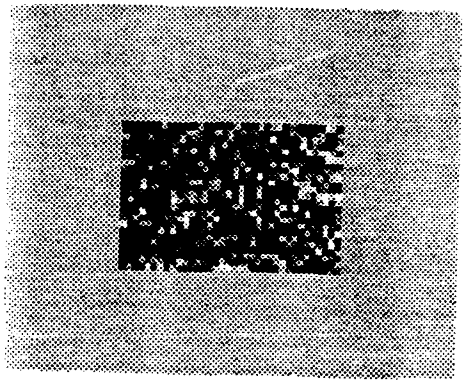

Figure 5(a)

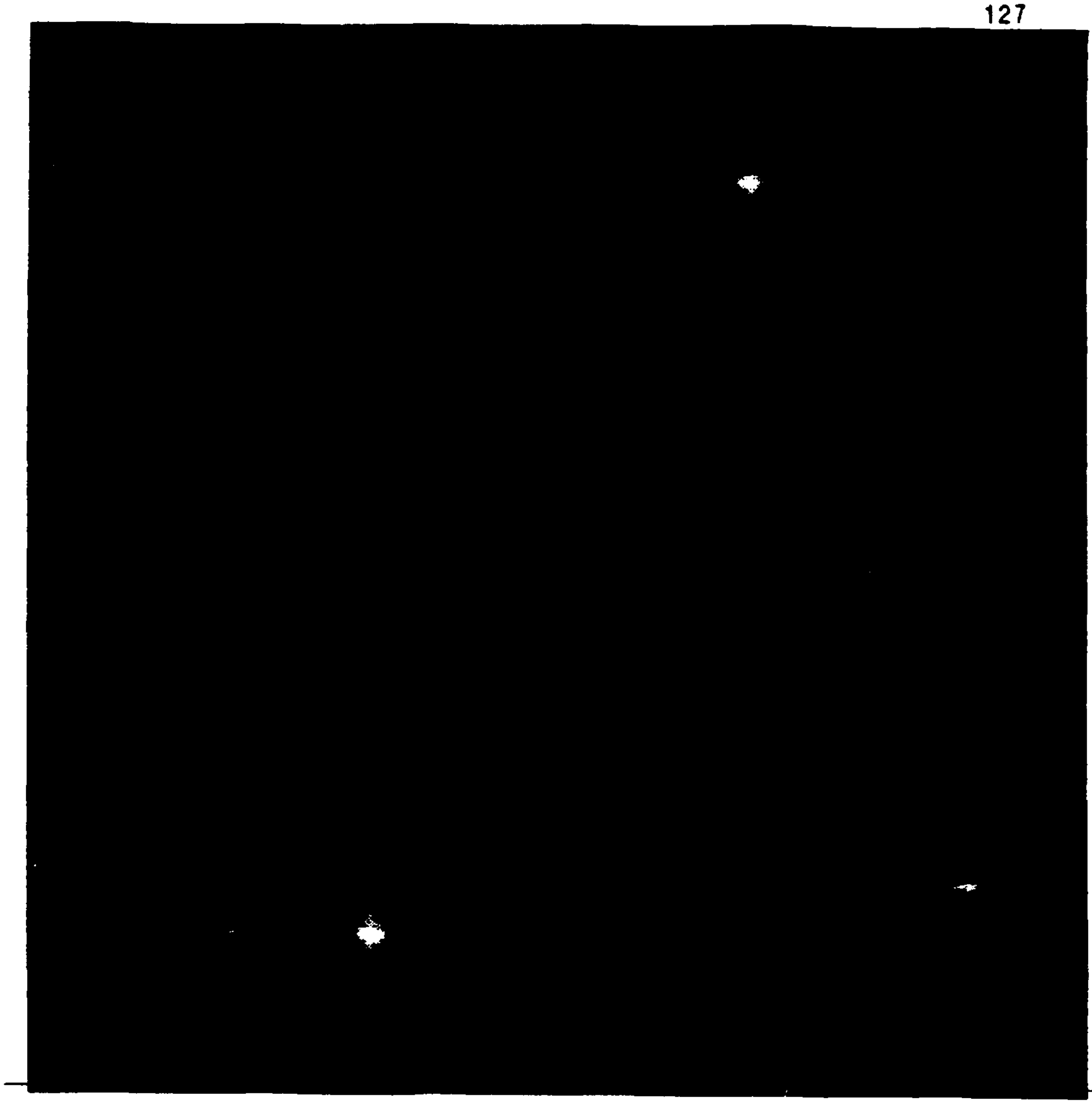

Figure 5(b)

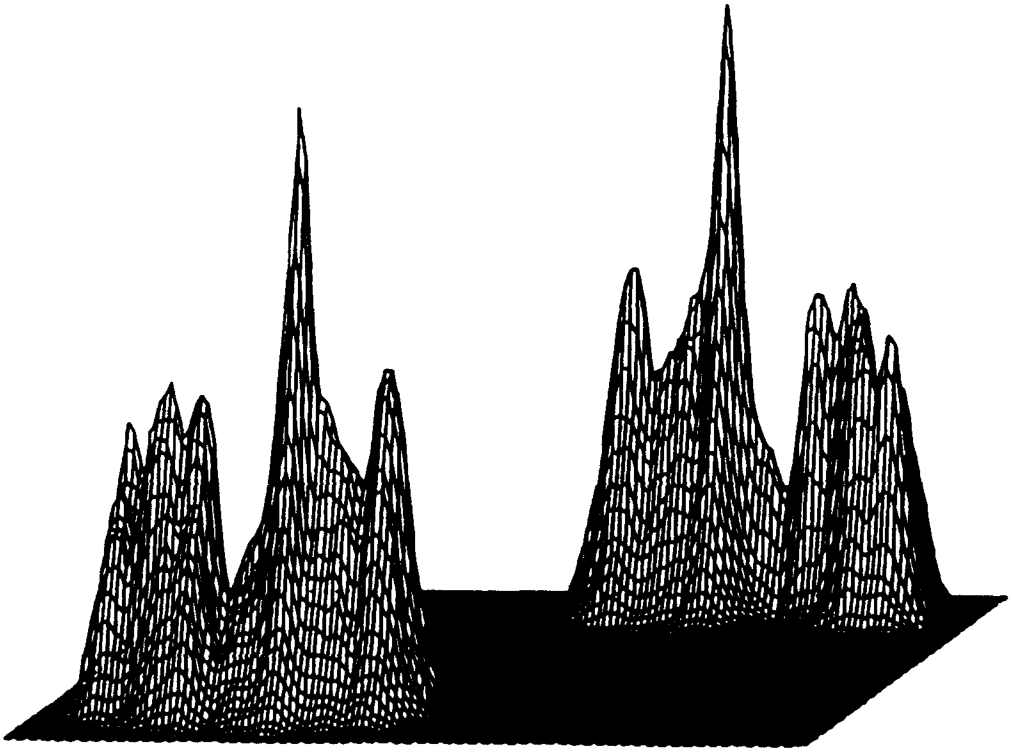

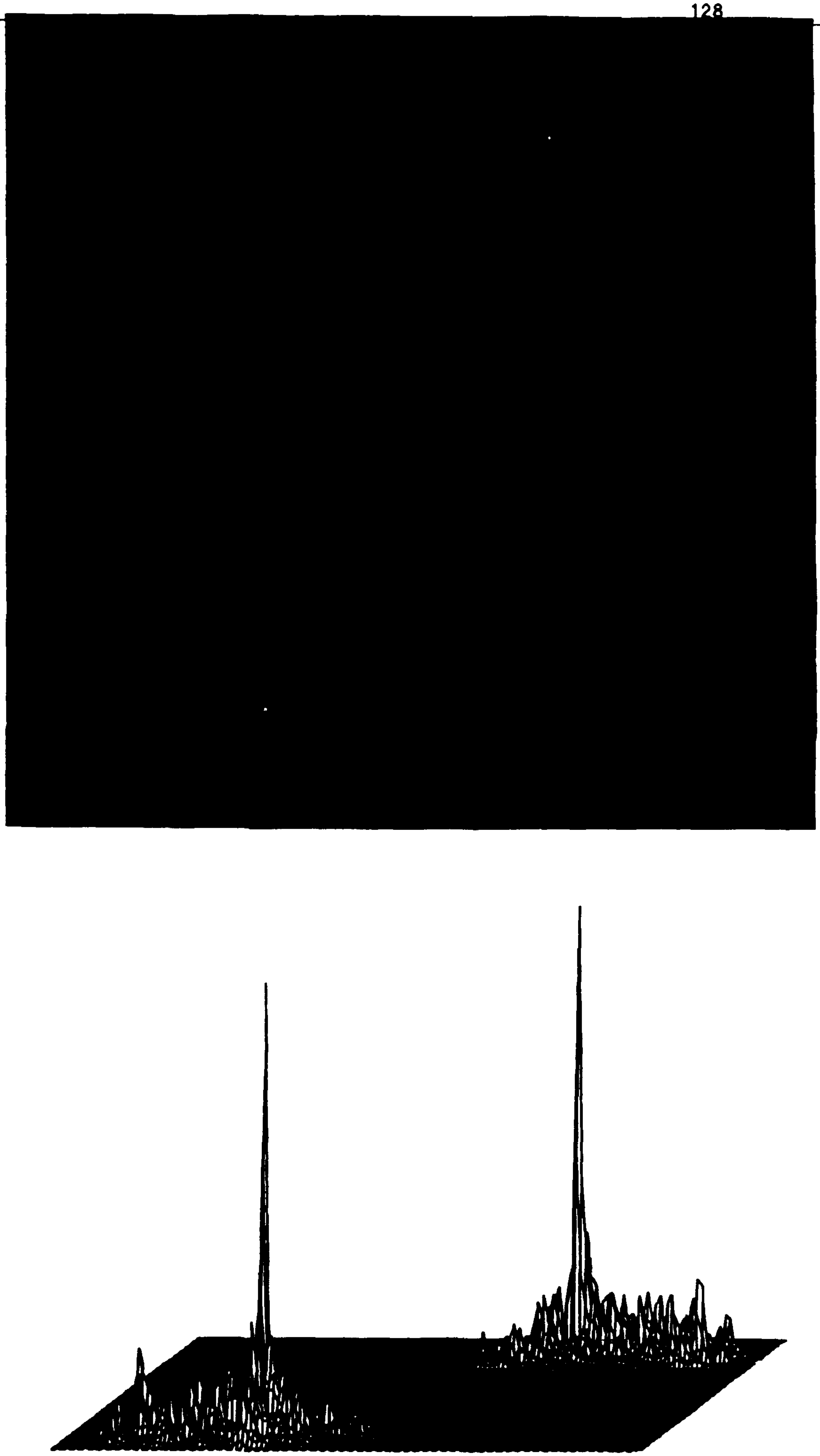

Figure 5(c)

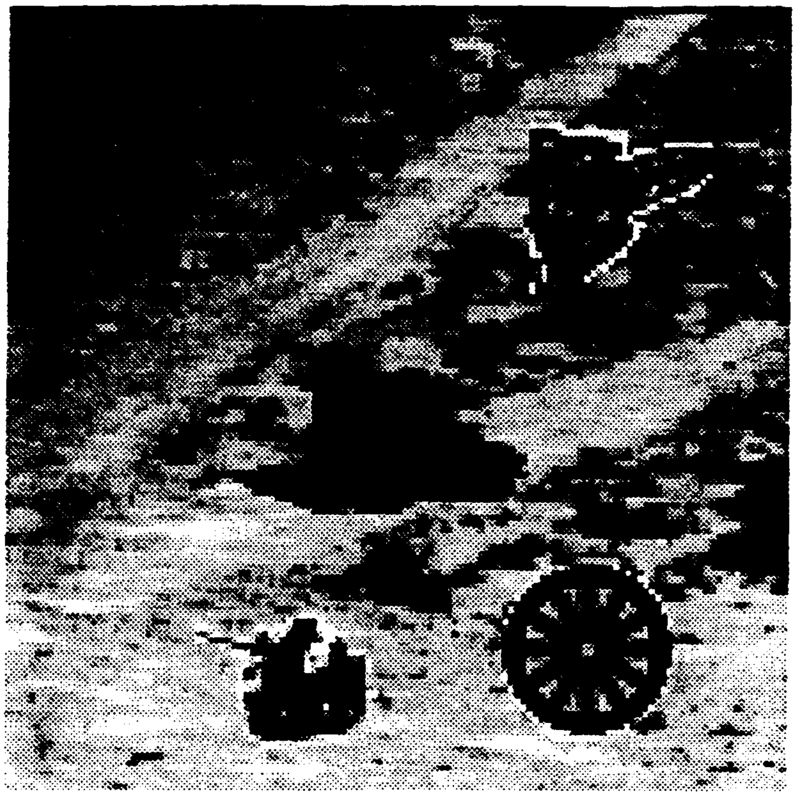

Figure 6(a)

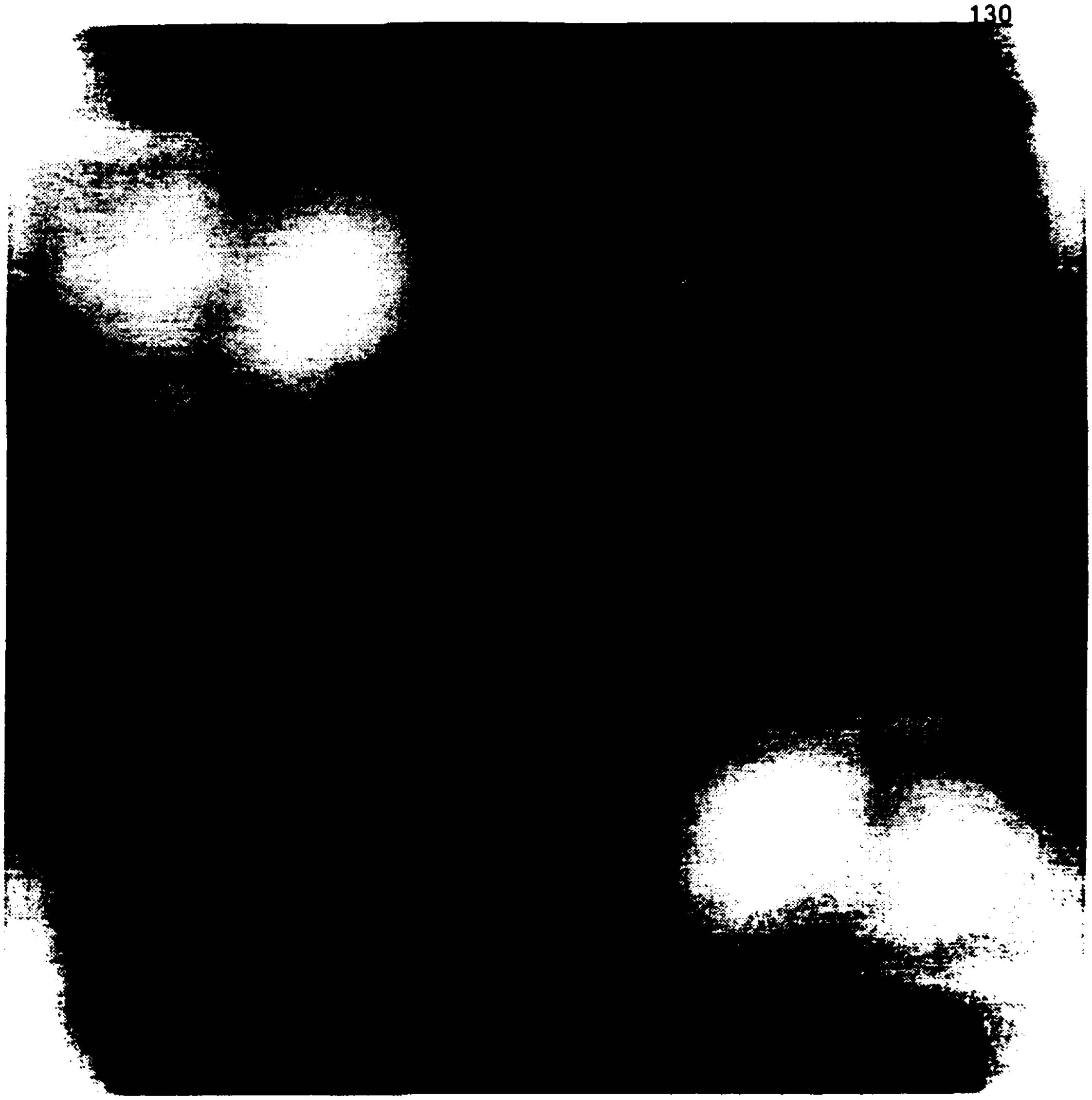

Figure 6(b)

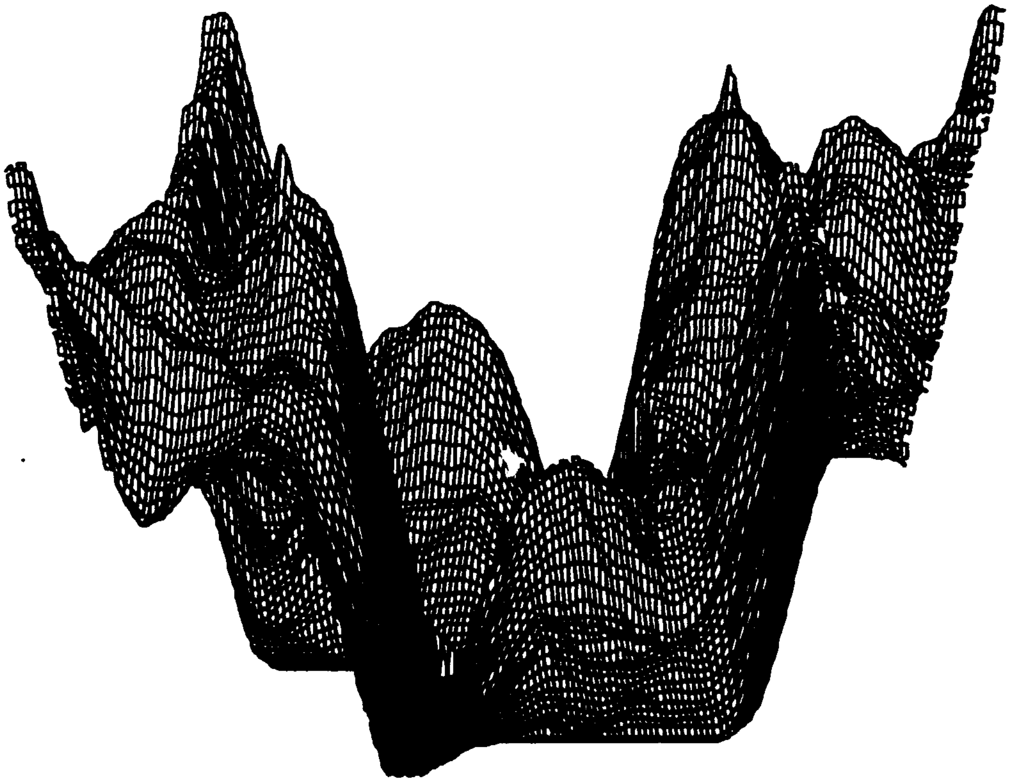

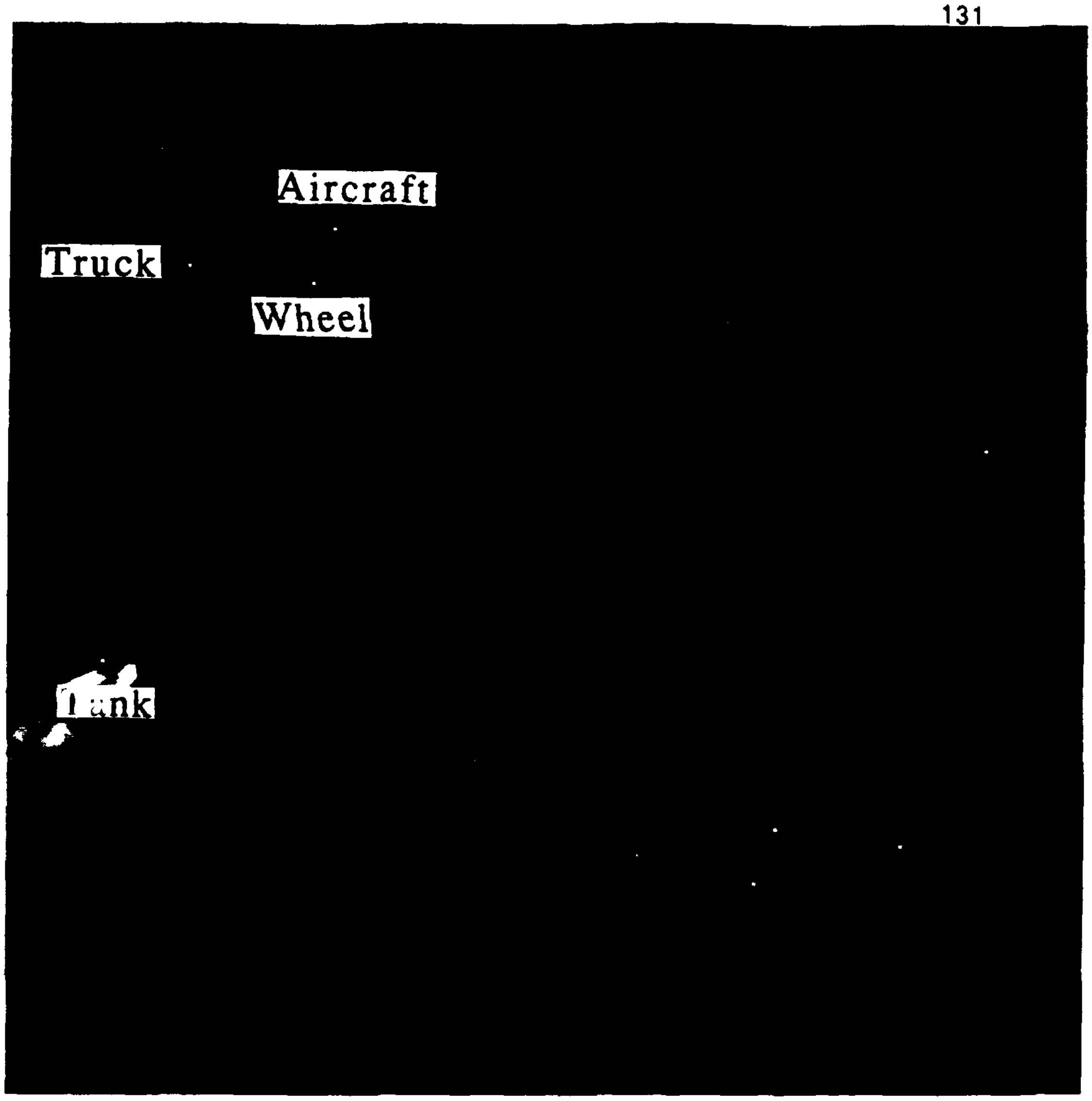

Figure 6(c)

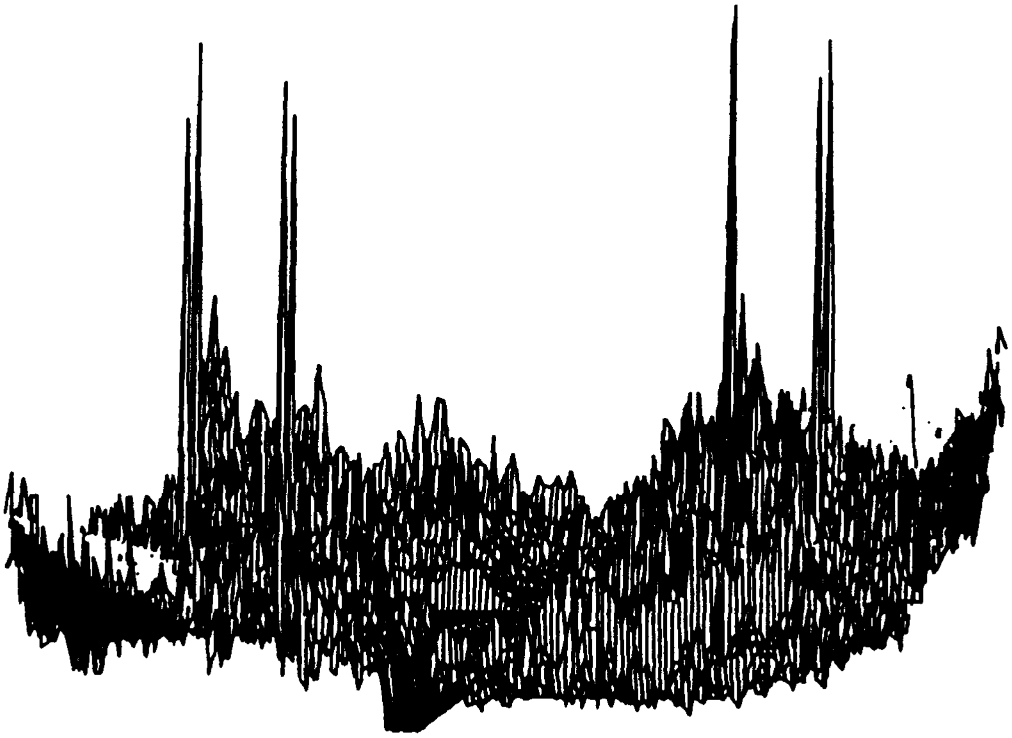

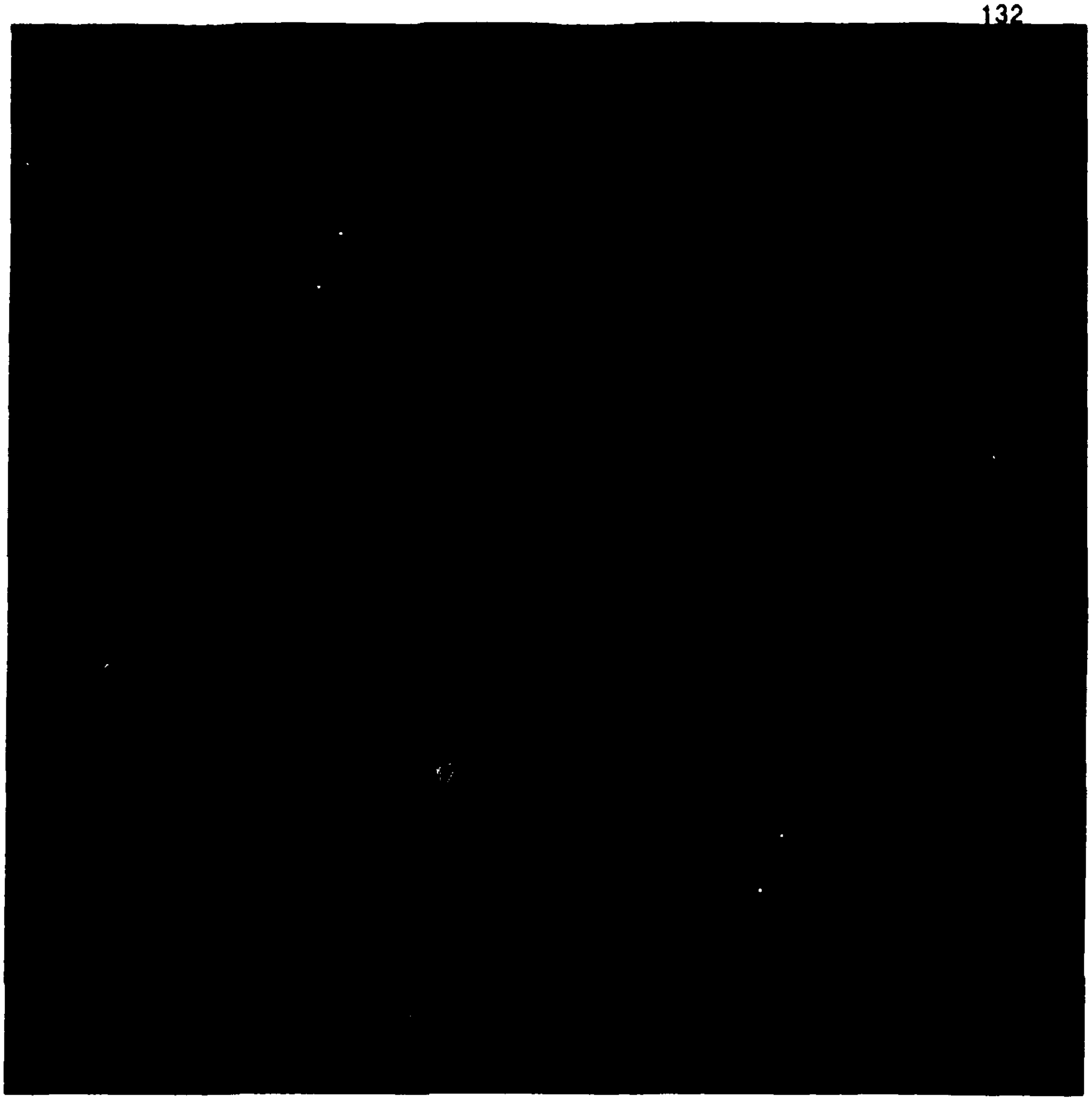

Figure 6(d)

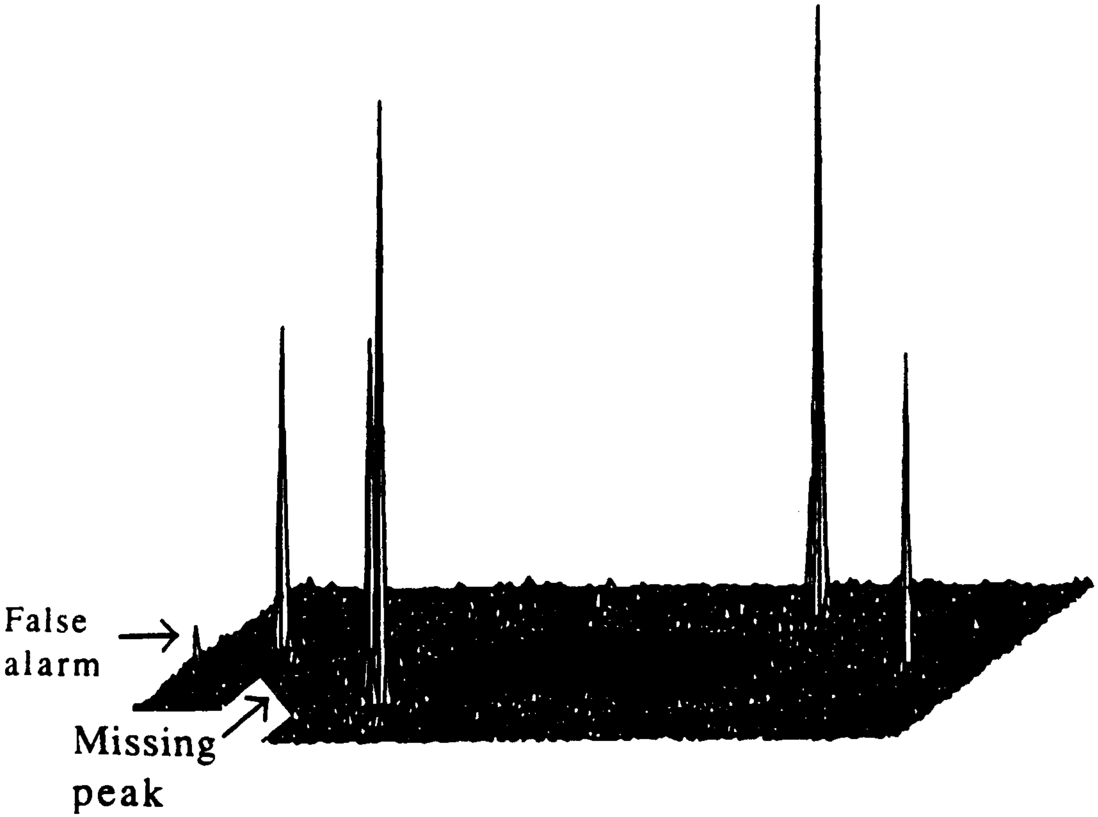

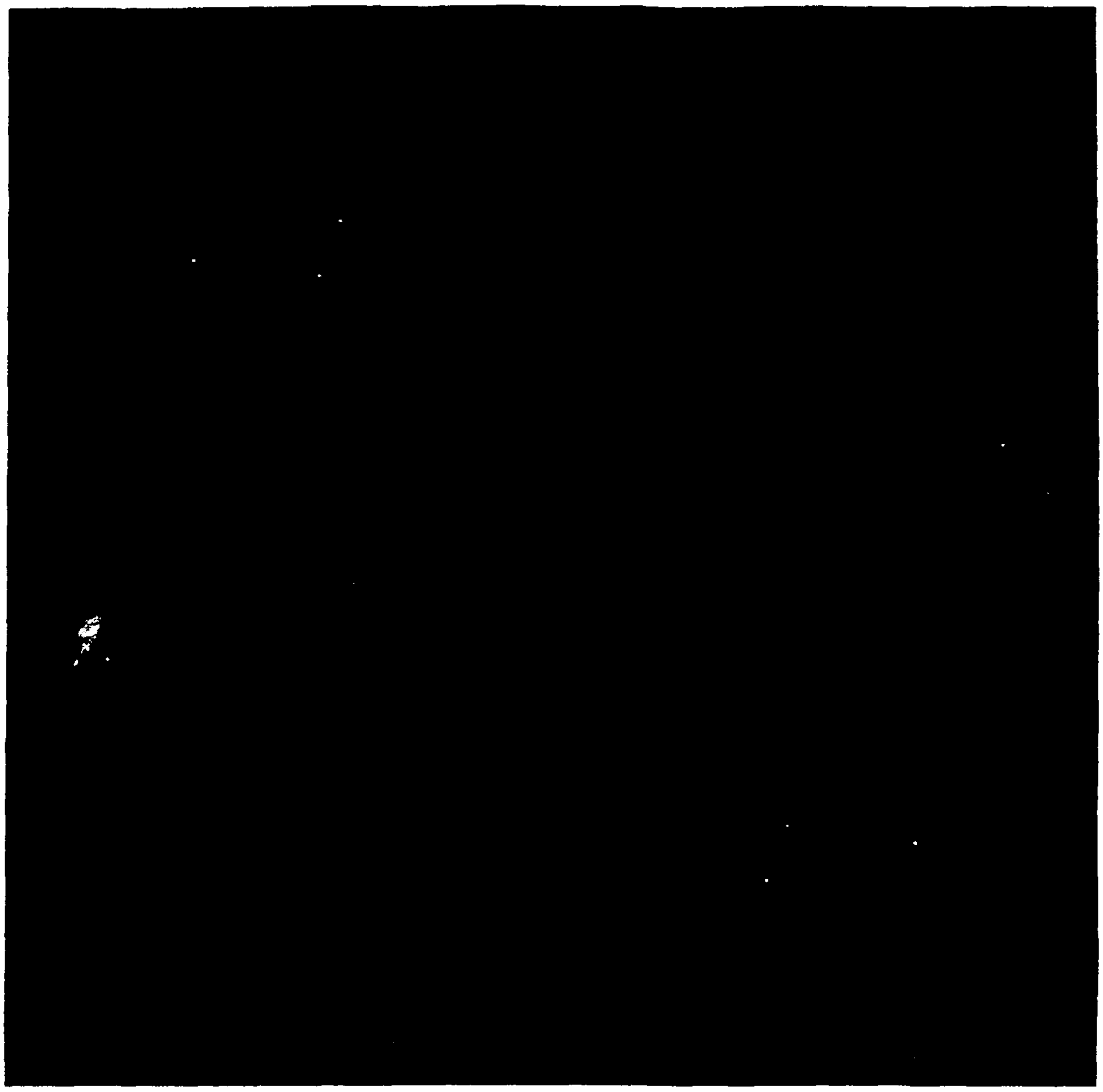

Figure 6(e)

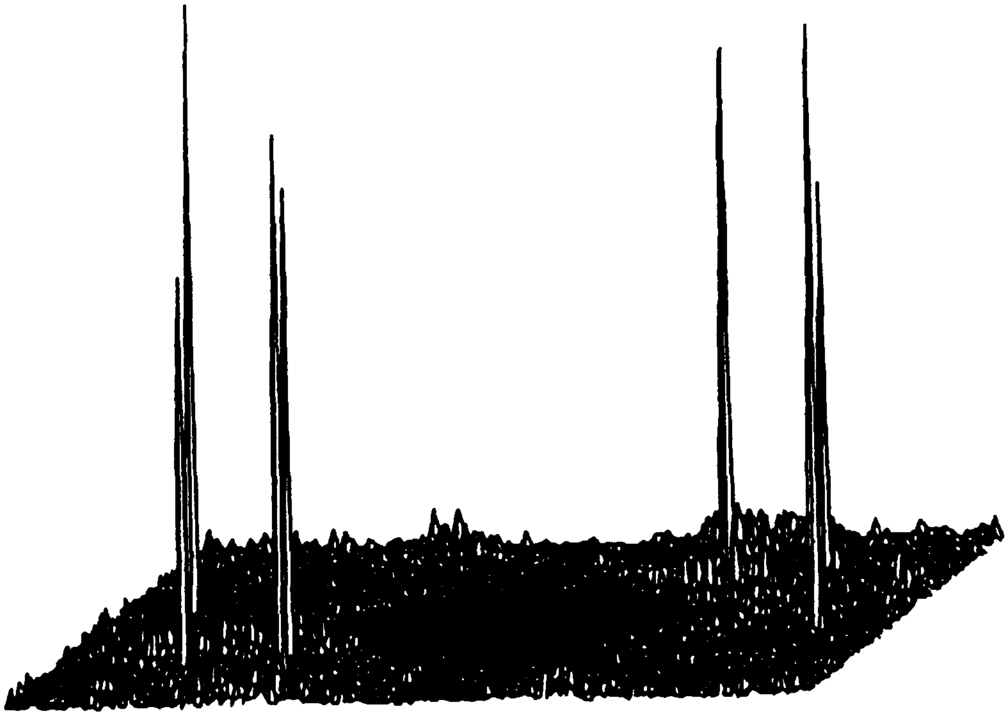

APPENDIX 10.7

Moment Invariant Neural Net

Optik 89, No. 2 (1991) 55-58 © Wissenschaftliche Verlagsgesellschaft mbH, Stuttgart

Application of moment invariant pattern recognition to optical neural net

F. T. S. Yu, Y. Li, X. Yang, and T. Lu

Electrical and Computer Engineering Department, The Pennsylvania State University, University Park, Pennsylvania, USA

D. A. Gregory

U.S. Army Missile Command, Redstone Arsenal, Alabama, USA

Application of moment invariant pattern recognition to optical neural net. Shift, scale and rotation invariant pattern recognition using moment invariants is discussed in this paper. Calculated moment invariants are coded in binary forms, which are used to construct the associative memory in the neural network. The combination of moment invariants with optical neural network makes it possible to realize the distortion invariant pattern recognition. Shift and rotation invariances have been experimentally demonstrated with a low-cost LCTV optical neural network using the moment invariant principle.

Anwendung der momenteninvarianten Zeichenerkennung in optischen neuronalen Netzen. In dieser Arbeit wird die verschiebungs-, skalierungs- und rotationsinvariante Zeichenerkennung mittels Momenteninvarianten besprochen. Berechnete Momenteninvarianten werden in binärer Form kodiert und zur Bildung assoziativer Speicher in neuronalen Netzen verwendet. Die Kombination von Momenteninvarianten mit optischen neuronalen Netzwerken ermöglicht die verzeichnungsfreie Zeichenerkennung. Verschiebungs- und Rotationsinvarianz wurden experimentell mit einem billigen LCTV optischen neuronalen Netz unter Verwendung des Prinzipes der Momenteninvarianz bestätigt.

1. Introduction

An image generally contains a large amount of information, for which pattern recognition is usually loaded with heavy and time consuming computation. However pattern recognition can be performed more efficiently by the biological neural net, which has led to intensive research on artificial neural network (ANN) [1-3]. Because of the massive parallel operation of the neural net, von Neumann digital computer is not suitable for its implementation. Since optics offers the advantage of three dimensional (3-D) interconnection and parallel processing, it has become a prime candidate for the implementation of ANN [4-7]. Although neural network is robust to input noise, most of the neural network models are not distortion invariant (e.g., shift, rotation and scale variation), which severely limits the practical application. Since the distortion invariant pattern recognition is the ultimate goal that we would like to achieve, in this paper, we shall discuss an invariant neural network using the principle of moment invariant. Application to an optical neural network is also provided.

2. Encoding of moment invariants

In 1962, Hu has introduced the concept of moment invariant to optical pattern recognition [8], by which the moment of an image irradiance $f(x, y)$ is defined as

$$m_{p,q} = \iint x^p y^q f(x, y)\, dx\, dy, \quad (p, q = 0, 1, 2, \ldots). \quad (1)$$

Apparently, this definition is not invariant to distortion. To obtain the shift invariance, central moment is defined as:

$$C_{p,q} = \iint x^p y^q f(x + x_0, y + y_0)\, dx\, dy, \quad (p, q = 0, 1, 2, \ldots). \quad (2)$$

where

$$x_0 = \frac{m_{1,0}}{m_{0,0}}, \quad (3\text{a})$$

$$y_0 = \frac{m_{0,1}}{m_{0,0}}, \quad (3\text{b})$$

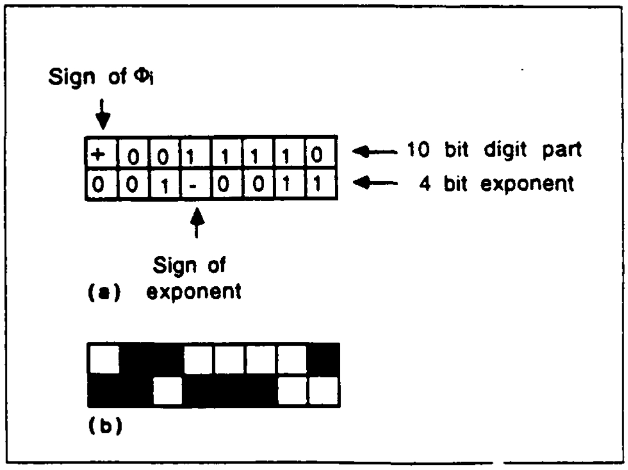

Fig. 1. Encoding of moment invariants. (a) The construction of the binary codes; (b) binary code of value 241×10^{-3}.

Received May 23, 1991. In final form July 5, 1991.

Francis T. S. Yu, Yajun Li, Xiangyang Yang, Taiwei Lu, Electrical and Computer Engineering Department, The Pennsylvania State University, University Park, PA 16802, USA.

Don A. Gregory, U.S. Army Missile Command, Redstone Arsenal, Alabama 35898, USA.

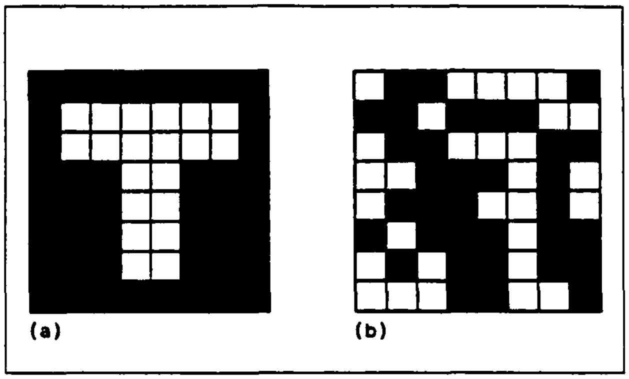

Fig. 2. Binary code array. (a) English letter "T"; (b) binary code of its moment invariants.

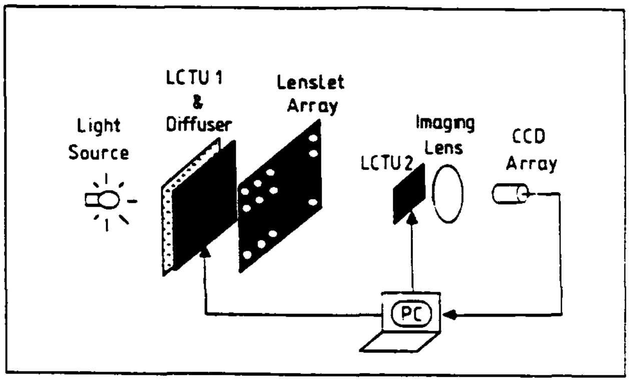

Fig. 3. The optical neural network.

is the centroid of the image irradiance $f(x, y)$. The central moments can be further normalized to achieve the scale invariance:

$$M_{p,q} = \frac{C_{p,q}}{C_{0,0}^{1+(p+q)/2}}. \tag{4}$$

Hu has also derived seven normalized moment invariants, which are shift, scale and rotation invariant [8]. The first four of the seven moment invariants are repeated in the following:

$$\Phi_1 = M_{2,0} + M_{0,2}, \tag{5}$$

$$\Phi_2 = (M_{2,0} - M_{0,2})^2 + 4\,M_{1,1}^2, \tag{6}$$

$$\Phi_3 = (M_{3,0} - 3\,M_{1,2})^2 + (3\,M_{1,2} - M_{0,3})^2, \tag{7}$$

$$\Phi_4 = (M_{3,0} + M_{1,2})^2 + (M_{2,1} + M_{0,3})^2. \tag{8}$$

We note that these moments have been proven sufficient to discriminate alphabetical characters, which permits the recognition of multisensor imagery [9, 10].

Recently, Yu and Li have proposed the application of the moments invariants to neurocomputing, for which they suggested to encode the moment invariants in the preprocessing circuit prior being applied to an optical neural network (ONN) [11, 12]. They have shown that the order of magnitude of moment invariants decreases, by which the attention can be concentrated to the lower order moment invariants. In fact, only the first four moment invariants (i.e., eqs. (5)–(8)) have been shown adequate for the recognition. For the implementation on an 8 × 8-neuron network, each of the moment invariants is encoded into a 16-bit binary signal, in which 10 bits represent the digit part of the moments, 4 bits are the exponential part and the remaining 2 bits present the sign bits. An example of encoding a value of 241×10^{-3} into its binary code is shown in fig. 1, in which the digital part is converted into a binary sequence as given by

$$+(241)\,D = +(0011110001)\,B, \tag{9}$$

and the exponent is converted as

$$-(3)\,D = -(0011)\,B. \tag{10}$$

Notice that the bright pixels represent the "+" sign and the "1" state, while the dark pixels represent the "−" sign and the "0" state. Since the 16-bit binary code is folded into 2 rows, the first four moment invariants can be encoded into a 8 × 8 array. Fig. 2 shows the English character "T" and its associated binary code of the first four moment invariants, i.e.,

$$\Phi_1 = 241 \times 10^{-3},$$

$$\Phi_2 = 230 \times 10^{-5},$$

$$\Phi_3 = 106 \times 10^{-4},$$

and $\Phi_4 = 551 \times 10^{-6}$.

Because of the one-to-one mapping between the moment invariant sequence $\{\Phi_i\}$ and the image distribution $f(x, y)$, the binary codes can be used to represent the patterns without risk, as long as the encoding array has a capacity to accommodate all the coded exemplars. We note that the moment invariants are sensitive to noise [13], that would pose limited practical application. In order to improve the roustness, the moment invariant sequences can be applied to a neural network for pattern recognition.

3. Optical neural network

Notice that the iterative equation of a two-dimensional (2-D) neural network is given by

$$U_{lk}(n+1) = f\left[\sum_{i=1}^{N}\sum_{j=1}^{N} T_{lkij}U_{ij}(n)\right] \tag{11}$$

where U_{lk} and U_{ij} represent 2-D pattern vectors, T_{lkij} is a 4-D interconnection weight matrix (IWM), and $f[\cdot]$ is a nonlinear operator which is usually a sigmoid function for gray level images and a thresholding function for binary patterns. Since the matrix T can be partitioned into an array of submatrices, it can be displayed on a spatial light modulator (SLM).

The schematic diagram of a compact optical neural network with 8 × 8 neurons is shown in fig. 3 [6]. An 80-W Xenon Arc lamp is used as the incoherent light source. A Hitachi Model C5-LC1 5 inch color liquid crystal television (LCTV) and a Seiko Model LVD-202 3 inch LCTV

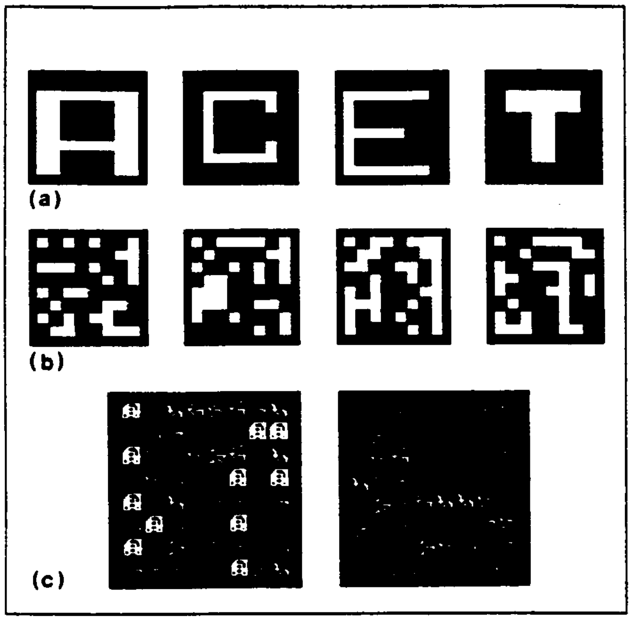

Fig. 4. (a) Four exemplar letters; (b) binary codes of their moment invariants; (c) positive (left) and negative (right) parts of the IWM.

are used as spatial light modulators. The learning process is conducted in the microcomputer. The calculated interconnection weights are displayed on the Hitachi LCTV (LCTV1) as a matrix, i.e., IWM, which consists of an 8 × 8 array of submatrices with each submatrix having 8 × 8 elements. The Seiko LCTV (LCTV2) is used as an input device to display the input patterns. The lenslet array, which consists of 8 × 8 lenses of 6 mm diameter and 36 mm focal length, establishes the interconnections between the IWM and input pattern. The lenslet array is imaged by the imaging lens onto the charge coupled device (CCD) camera. The overall light through each specific lenslet is collected by the CCD camera to form an 8 × 8 output array. The detected signals are then sent to a digital thresholding circuit to perform the nonlinear operation, for which the final result can be fed back to the LCTV2 for next iteration.

4. Experimental demonstration

Distortion invariant pattern recognition is demonstrated using the optical neural network described in the previous section. In our experiments, English letters are used as the training set, in which four letters "A", "C", "E" and "T" and their moment invariant encoded patterns are shown in fig. 4(a) and 4(b), respectively. The interpattern association (IPA) model has been used to construct the optical neural network [14]. The IPA model uses the association among the reference patterns and emphasizes on the special features of each pattern. The interconnection weights are determined by simple logic rules. Since the IPA model is based on the comparison of differences rather than the similarities of the reference patterns, it has a larger storage capacity and better performance than the Hopfield model. The IPA model generates ternary interconnection weights. Although the area encoding and biasing method can be used to accommodate the negative value of the IWM, the positive and negative parts of the IWMs are sequentially displayed on the LCTV2 for simplicity. A subtraction operation is performed by the microcomputer before the thresholding. The positive and negative parts of the IWM are depicted in fig. 4(c).

As an example, the character "T" is rotated 90° and shifted one pixel up and one pixel left. It is then embedded in 20% random noise, as shown in fig. 5(a). The corresponding encoded moment invariant is illustrated in fig. 5(b). If this encoded pattern is displayed on LCTV2 of the optical neural network, a convergent result is obtained after only one iteration, as shown in fig. 5(c). Thus by decoding fig. 5(c), a final result of "T" can be seen in fig. 5(d). Hence, by applying moment invariant principle to the neural net, pattern recognition under shift, rotation and noise disturbances can be achieved. We stress that since the optical neural network we used has 8 × 8 neurons (i.e., pixels), the scale invariance has not been tested in our experiment; nevertheless it can be easily verified using computer simulation [11]. In order to achieve the scale invariance, more pixels (e.g., 32 × 32 pixels) are needed for the display of the input patterns. Thus, a large scale optical neural network with adequate neurons is required.

We further notice that although the decoding (e.g., from fig. 5(c) to 5(d)) is performed by a microcomputer, it can be accomplished optically by adding a second neural layer using a hetero-associative algorithm. Furthermore, the multilayer structure will make the neural network more robust to the image distortions as well as to the input noise.

We have also tested the processing capacity of the 8 × 8-neuron optical neural network, for which various combinations of the English letters are used as the training set. We have found that the neural network can always converge to the correct result up to 4 stored patterns and about 40% error probability for 5 stored patterns, however if the number of the stored patterns is beyond 6, the network becomes unstable and generally converges to a "spurious" output, which is different from all the examplars.

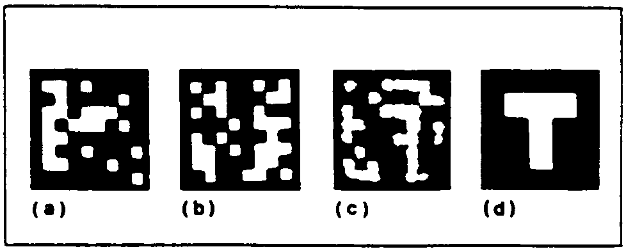

Fig. 5. Experimental result. (a) Letter "T" with shift, 90° rotation and 20% random noise; (b) binary code of pattern (a); (c) output pattern of neural network; (d) decoded result.

5. Concluding remarks

In concluding this paper, we would remark that, in order to increase the discriminability and the processing capacity of the neurocomputing, higher order moment invariants should be also considered. However it would require more pixels for the encoding. Furthermore, since the different bits in the binary code represent the values of different order of magnitude, it represents an nonuniformly weighted code. For instance, the first bit in the 10 digit bits represents a value of 512, but the last bit represents only a value of 1. Because all the bits will be equally processed in the optical neural network, to improve the overall performance, either a uniformly weighted code has to be developed, or the network should be trained to process nonuniformly (e.g., pay more attention to the neurons representing the exponent than those representing the lower digit bits).

Acknowledgement

We acknowledge the support of the US Army Missile Command through the US Army Research Office under contract DAAL03-87-0147.

References

[1] K. Fukushima: Neural network model for selective attention in visual pattern recognition and associative recall. Appl. Opt. 26 (1987) 4985-4992.

[2] G. A. Carpenter: Neural network model for pattern recognition and associative memory. Neural Networks 2 (1989) 243-257.

[3] O. J. Murphy: Nearest neighbor pattern classification perceptrons. Proc. IEEE 78 (1990) 1595-1599.

[4] N. H. Farhat, D. Psaltis: Optical implementation of associative memory based on models of neural network. In J. L. Horner ed.: Optical Signal Processing, pp. 129-162. Academic Press, New York 1987.

[5] K. Hsu, H. Li, D. Psaltis: Holographic implementation of a fully connected neural network. Proc. IEEE 78 (1990) 1637-1645.

[6] F. T. S. Yu, T. Lu, X. Yang, D. A. Gregory: Optical neural network with pocket sized liquid crystal televisions. Opt. Lett. 15 (1990) 863-865.

[7] X. Yang, T. Lu, F. T. S. Yu: Compact optical neural network using cascaded liquid crystal televisions. Appl. Opt. 29 (1990) 5223-5225.

[8] M.-K. Hu: Visual pattern recognition by moment invariants. IRE Trans. Inform. Theory IT-8 (1962) 179-187.

[9] M. R. Teague: Image analysis via the general theory of moments. J. Opt. Soc. Am. 70 (1980) 920-930.

[10] D. Casasent, D. Psaltis: Hybrid processor to compute invariant moments for pattern recognition. Opt. Lett. 5 (1980) 395.

[11] F. T. S. Yu, Y. Li: Application of moment invariants to neural computing for pattern recognition. Proc. SPIE 1297 (1990) 307-316.

[12] Y. Li, F. T. S. Yu: Variations of irradiance moments in neurocomputing for pattern recognition. Optik 86 (1991) 141-143.

[13] Y. Abu-Mostafa, D. Psaltis: Recognitive aspects of moment invariants. IEEE Trans. Pattern Anal. Mach. Intell. PAMI-6 (1984) 698-706.

[14] T. Lu, X. Xu, S. Wu, F. T. S. Yu: Neural network model using interpattern association. Appl. Opt. 29 (1990) 284-288.

APPENDIX 10.8

Mirror-Array Interconnection Neural Net

1602 OPTICS LETTERS / Vol. 16, No. 20 / October 15, 1991

Mirror-array optical interconnected neural network

Francis T. S. Yu, Xiangyang Yang, and Shizhuo Yin

Department of Electrical and Computer Engineering, The Pennsylvania State University, University Park, Pennsylvania 16802

Don A. Gregory

U.S. Army Missile Command, Redstone Arsenal, Alabama 35898

Received May 14, 1991

A high-light-efficiency optical neural network that uses a mirror-array interconnection is proposed. Design considerations for the mirror array and experimental demonstration are given.

Optical implementations of neural nets have been burgeoning in recent years.[1-11] One of the key reasons must be the massive interconnection capabilities of optics, in which either lenslet-array[1-6] or holographic[8-11] interconnections are employed. The basic distinction between these techniques is that the lenslet-array interconnection neural network is essentially an incoherent interconnection system, whereas the holographic interconnection is coherent. Although the advantage of using incoherent light is the capability of suppressing coherent artificial noise, the lenslet-array interconnection suffers from low light efficiency, which limits large-scale operations. To alleviate this shortcoming, we propose here a mirror-array interconnection method, for which high light efficiency can be achieved.

Let us recall the iterative equation for an $N \times N$ neuron network, as given by

$$u_{lk}(n+1) = f\left[\sum_{i=1}^{N}\sum_{j=1}^{N} T_{lkij}u_{ij}(n)\right], \qquad (1)$$

where u_{lk} and u_{ij} represent the N^2-element output and input pattern vectors, respectively, T_{lkij} is the N^4-element interconnection weight matrix (IWM), which is partitioned into a two-dimensional array of submatrices in order to be displayed on a spatial light modulator, and $f(\cdot)$ represents a nonlinear operator. The IWM submatrices can be interconnected onto the input pattern vector by a lenslet array.[5] All the IWM submatrices are imaged onto an $N \times N$ image array, but only one of these images would be used for the interconnection. It is apparent that the overall interconnection light efficiency of the system would be reduced by a factor of $1/N^2$.

To improve the light efficiency of the optical neural network, we discuss a mirror-array interconnection technique, as shown in Fig. 1, in which the IWM and the input pattern vector are displayed onto two tightly cascaded liquid-crystal televisions (LCTV's). As proposed in Ref. 5, the input pattern is enlarged so that each input pixel element is the same size as an IWM submatrix. If we assume that a collimated white light is illuminating the cascaded LCTV's as shown in the Fig. 1, the emerging light field would be proportional to the product $T_{lkij}u_{ij}(n)$. If we further assume that an $N \times N$ mirror array is affixed onto a parabolic substrate, then each of the mirror elements would reflect the product submatrix $[TU]$ submatrices can be detected by the charge-coupled-device (CCD) detector. By properly thresholding the array of output signals, an output pattern vector can be obtained, and it can also be fed back to LCTV1 for the next iteration. We note that by using the mirror array for interconnections, the light efficiency of the system would increase by a factor of N^2 compared with the lenslet technique.

As can be seen in Fig. 1 the reflected product submatrices $[TU]$ are not, however, perfectly superimposed with respect to each other, and this may deteriorate the interconnection performance. Let us now consider a one-dimensional analysis in the following:

The position error occurs mostly at the edge of the $[TU]$ submatrices as given by

$$\epsilon = \frac{Na}{4}\beta^2, \qquad (2)$$

where N is the number of neurons in a row or column of the two-dimensional input, a is the pixel size, and β is the maximum allowable angle with respect to the mirror array, which can be estimated as (in the paraxial case)

$$\beta = \frac{N^2 a}{F \cos\theta}, \qquad (3)$$

with F the focal length of the parabolic substrate and θ the angle between the incident and the reflected light beams. By substituting Eq. (3) into Eq. (2), we have

$$\epsilon = \frac{N^5 a^3}{4F^2 \cos^2\theta}, \qquad (4)$$

in which the position error increases as the fifth power of the number of neurons (i.e., N^5).

Note that the pixel overlapping within the interconnected product submatrices $[TU]$ would also deteriorate the performance of the system. This is primarily due to the diffraction effect and the source

0146-9592/91/201602-03$5.00/0

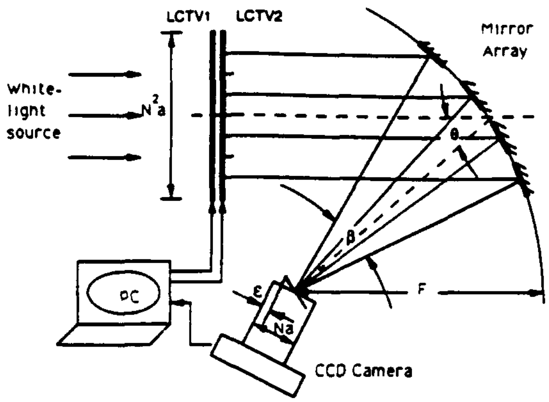

Fig. 1. Schematic diagram of the optical neural net with a mirror array.

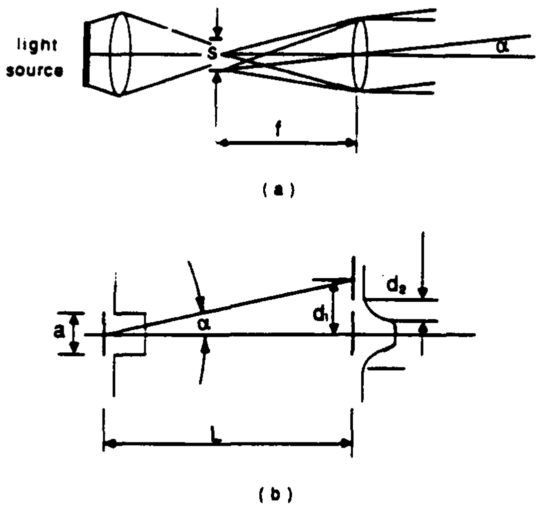

Fig. 2. Shadow-casting imaging configuration: (a) effect due to a light source, (b) image shifting due to source size and image broadening due to diffraction.

of the system. For example, an extended light source would produce a divergent angle as given by

$$\alpha = \frac{s}{2f}, \tag{5}$$

where s is the source size and f is the focal length of the collimating lens, as shown in Fig. 2(a). Figure 2(b) illustrates the shifting effect of the pixel image, in which the deviation of the shadow-casted image can be expressed as

$$d_1 = l\alpha = \frac{Ls}{2f}, \tag{6}$$

where L is the distance from the LCTV's to the CCD detector. Figure 2(b) also shows the diffraction effect on a pixel. The spread of the pixel images is given by

$$d_2 = \frac{\lambda L}{a}, \tag{7}$$

where λ is the wavelength of the light source.[12] We now restrict the position errors and overlapping pixel to be within one tenth of the pixel size, which are the criteria for excellent performance of the system. Then we have

$$\epsilon < \frac{a}{10}, \tag{8}$$

$$d = d_1 + d_2 < \frac{a}{10}. \tag{9}$$

With these restrictions, adverse effects of the proposed mirror-array interconnections can be minimized.

For example, given a 4 × 4 neuron net, in which we assume that the pixel size is 2 mm, the distance between the $[TU]$ plane and the CCD detector is approximately 300 mm and the focal lengths of the collimating lens and the parabolic substrate are 400 and 175 mm, respectively. If the maximum angle between the incident and the reflected light beams of the mirrors is 30°, the diameter of the source size is approximately 0.3 mm, and the mean wavelength of the light source is 0.5 μm, then the position error of the pixel is $\epsilon = 0.09$ mm $< (a/10) = 0.2$ mm and the overlapping pixel is $d = 0.19$ mm $< (a/10) = 0.2$ mm, which are within the criteria imposed by relations (8) and (9). For a system with more neurons (e.g., 32 × 32 neurons), the architectural parameters must be carefully designed in order to satisfy relations (8) and (9).

An optical neural network that uses a 4 × 4 mirror array is shown in Fig. 1, in which two cascaded Hitachi color LCTV's are used for the generation of the input pattern and the IWM. As an example, a training set of four 4 × 4 pixel binary patterns shown in Fig. 3(a) is used for the construction of the interpattern association memory matrix. The positive part of the IWM is shown on the left side of Fig. 3(b), and the negative part is shown on the right

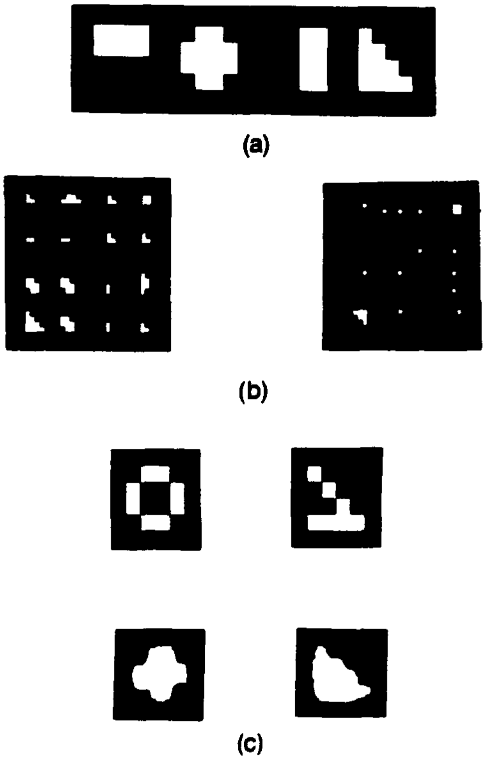

Fig. 3. Experimental results: (a) training set, (b) positive and negative parts of the IWM, (c) partial input patterns and the corresponding outputs.

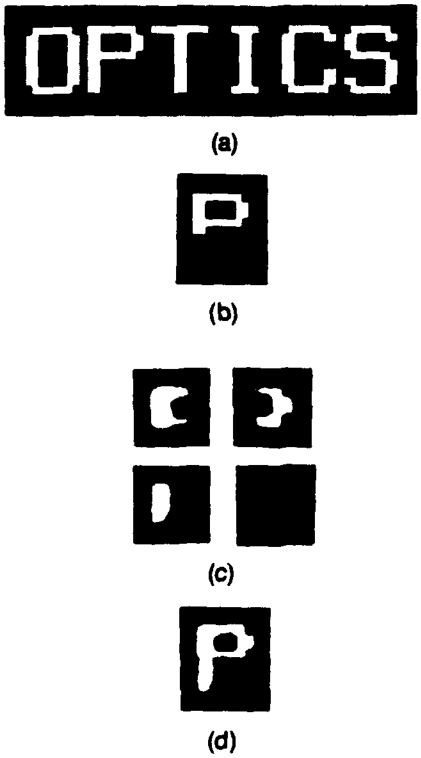

Fig. 4. Results with the space–time-sharing technique: (a) training set, (b) one partial input pattern, (c) suboutputs, (d) composed output.

side of Fig. 3(b). We assume that a partial input pattern is presented at the input LCTV [shown in the upper row of Fig. 3(c)]; then a reconstructed stored pattern can be recalled, as illustrated in the lower row of Fig. 3(c).

Since the space–bandwidth product of the 4 × 4 mirror-array neural net is rather limited, we have also used a space–time-sharing technique[6] for the determination, in which the six 8 × 8 pixel roman letters shown in Fig. 4(a) are used as the training set. The interpattern association IWM is partitioned into 2 × 2 sub-IWM's, which are sequentially displayed on LCTV2 with the input subpattern displayed on LCTV1. By thresholding the output signal array, an output subpattern can be reconstructed. We illustrate one partial input pattern P in Fig. 4(b). The corresponding output subpatterns obtained with the mirror-array interconnection are shown in Fig. 4(c). And the final composite results obtained with this proposed technique are given in Fig. 4(d), in which we see that fully reconstructed P is obtained.

In conclusion, we have presented a highly efficient optical neural net using a mirror array for interconnections. By replacing the commonly used lenslet array with the mirror array, we increase the light efficiency by a factor of N^2. The overall performance of the system depends on the source size, the diffraction effects, and the focal length of the parabolic mirror-array substrate. In short, the synthesizing of a large-scale mirror array for optical interconnections is possible, for which experimental demonstrations are provided.

We acknowledge the support of the U.S. Army Missile Command through the U.S. Army Research Office under contract DAAL03-91-G-0112.

References

1. N. H. Farhat, D. Psaltis, A. Prata, and E. Paek, Appl. Opt. **24**, 1496 (1985).
2. D. Psaltis and N. H. Farhat, Opt. Lett. **10**, 98 (1985).
3. T. Lu, S. Xu, S. Wu, and F. T. S. Yu, Appl. Opt. **28**, 4908 (1989).
4. F. T. S. Yu, T. Lu, X. Yang, and D. A. Gregory, Opt. Lett. **15**, 863 (1990).
5. X. Yang, T. Lu, and F. T. S. Yu, Appl. Opt. **29**, 5223 (1990).
6. F. T. S. Yu, X. Yang, and T. Lu, Opt. Lett. **16**, 247 (1991).
7. R. A. Athale and C. W. Stirk, Opt. Eng. **28**, 447 (1989).
8. C. Peterson, S. Refield, J. D. Keeler, and E. Hartman, Opt. Eng. **29**, 359 (1990).
9. K. Hsu, H. Li, and D. Psaltis, Proc. IEEE **78**, 1637 (1990).
10. J. S. Jang, S. Y. Shin, and S. Y. Lee, Opt. Lett. **13**, 693 (1988).
11. C. H. Wang and B. K. Jenkins, Appl. Opt. **29**, 2171 (1990).
12. M. Born and E. Wolf, *Principles of Optics* (Pergamon, Oxford, 1975).

APPENDIX 10.9

Redundant Interconnection Neural Net

Redundant-interconnection interpattern-association neural network

Xiangyang Yang, Taiwei Lu, Francis T. S. Yu, and Don A. Gregory

We have shown that introducing interconnection redundancy can make a neural network more robust. We describe performances under noisy input and partial input that show that the optimum-redundant interconnection improves both the noise tolerance and the pattern discriminability. Simulated and experimental demonstrations are also provided.

I. Introduction

There is much interest in neural networks, which is due primarily to their brainlike processing capabilities.[1-15] Although neural models were proposed a few decades ago, the resurgence of interest is due to the development of the Hopfield model.[3,4] The Hopfield model uses essentially the outer-product method to construct the interconnection weight matrix, which emphasizes the intrapattern associations but ignores the associations among the patterns. In other words, the Hopfield network becomes unstable for patterns of great similarity (e.g., fingerprints, handwriting).

We recently introduced an interpattern-association (IPA) algorithm in an optical neural network,[12,13] in which the special and the common features among the reference patterns can be determined. However, we show here that the interconnection for an IPA network would be highly redundant. Although a more highly redundant interconnection would produce higher noise immunity, the discriminability would be reduced. We show, however, that the overall performance of a neural net should be improved, if an optimum-redundant-interconnection network can be found.

II. Interpattern-Association Model

We note that the excitatory and the inhibitory interconnections of an IPA neural network can be determined by using the logic operation illustrated in Fig. 1. Assume that three reference patterns are situated in the pattern space, in which the special and the common subsets are defined. If the states between two different subsets are complementary (e.g., $P_1\bar{P}_2\bar{P}_3$ and $\bar{P}_1P_2P_3$), then these subsets are called opposite subsets. Thus, when an input neuron in a subset is excited, all the output neurons in the same subset will be excited, but the output neurons in the opposite subset will be inhibited. In other words, if an input neuron in $P_1P_2\bar{P}_3$ is excited, the input pattern has the features of the P_1 and P_2 patterns but has no features of pattern P_3. Therefore this neuron will excite all the output neurons within $P_1P_2\bar{P}_3$ and inhibit all the output neurons in $\bar{P}_1\bar{P}_2P_3$. Thus, by using this logic operation, we would not find a redundant interconnection between the input and the output neurons.

By using logic-operation rules, we observe that the output neurons within the common subsets will be excited not only by the input neurons but also by those belonging to the special subsets. However, the output neurons represented by the special subsets would be excited by the input neurons belonging to the special subsets. In other words, subsets in a higher order would be excited by the lower-order subsets, but this is not true for the reverse. For instance, output neurons belonging to $P_1P_2\bar{P}_3$, (i.e., second order) would be excited not only by the input neurons that belong to $P_1P_2\bar{P}_3$ but also by the input neurons within $P_1\bar{P}_2\bar{P}_3$ and $\bar{P}_1P_2\bar{P}_3$ (i.e., first order). Because the common features $P_1P_2P_3$ represent the third-order subset, the neurons within this subset can be excited by all other subsets. Because the special features $P_1\bar{P}_2\bar{P}_3$, $\bar{P}_1P_2\bar{P}_3$, and $\bar{P}_1\bar{P}_2P_3$ are at the lowest order, they can be excited by only themselves. It is therefore apparent that the common features would have more redundant interconnections. The redundancy level of excitation can be defined as the difference in the orders of interconnection. The redun-

---

X. Yang, T. Lu, and F. T. S. Yu are with the Department of Electrical and Computer Engineering, Pennsylvania State University, University Park, Pennsylvania 16802. D. A. Gregory is with the U.S. Missile Command, Redstone Arsenal, Alabama 35898.

Received 30 October 1990.
0003-6935/91/355182-06$05.00/0.

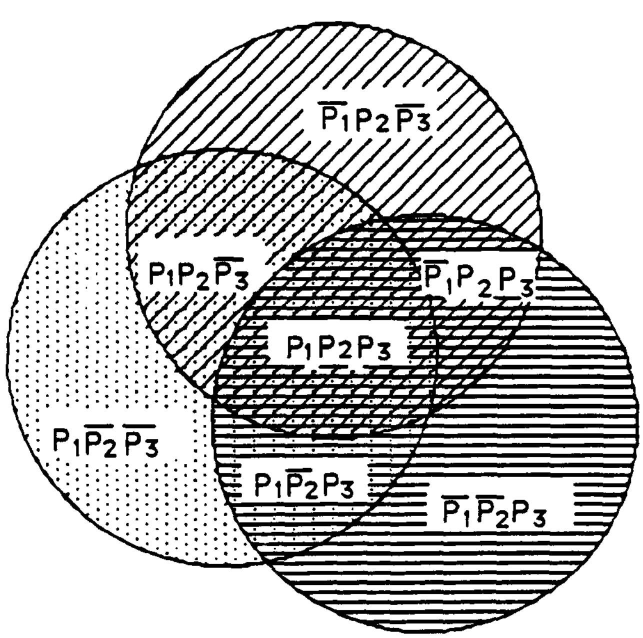

Fig. 1. Representations of the reference patterns in a pattern space. Subsets are categorized into three orders: $P_1\overline{P}_2\overline{P}_3$, $\overline{P}_1P_2\overline{P}_3$, and $\overline{P}_1\overline{P}_2P_3$ are in the first order; $P_1P_2\overline{P}_3$, $\overline{P}_1P_2P_3$, and $P_1\overline{P}_2P_3$ are in the second order; and $P_1P_2P_3$ is in the third order.

dancy level of inhibition can be determined in the same manner.

It can be seen that with the IPA algorithm the common features are enhanced, whereas the special features are relatively suppressed. Thus the neural net is less effective in recognizing patterns of great similarities. For example, the letter P has all the common features of B and R. An input letter B to the IPA neural net may produce an erroneous output P.

There is, however, an advantage to implementing redundant interconnection in a neural network, for which a greater input-noise immunity is provided. The conjectural performance of a redundant interconnection with respect to the input-noise tolerance and the pattern discriminability is plotted in Fig. 2, in which an optimum-redundancy level can be found.

III. Redundant-Interconnection Interpattern-Association Model

In this section we discuss a redundant-interconnection IPA (R-IPA) network, in which a set of binary reference patterns, $P_1, P_2, \ldots, P_M$, is stored in the memory matrix. The excitation and the inhibition interconnections can be determined by the following logic operations:

$$S_{in} = P_1P_2\ldots P_k\overline{P}_{k+1}\overline{P}_{k+2}\ldots\overline{P}_M \quad (1 \le k \le M), \tag{1}$$

$$S_{out} = P_1P_2\ldots P_m\overline{P}_{m+1}\overline{P}_{m+2}\ldots\overline{P}_M \quad (1 \le m \le M). \tag{2}$$

Thus the differences between the excitatory layers (ELD) and the inhibitory layers (ILD) are given by

$$\mathrm{ELD} = M - k \quad (m > k), \tag{3}$$

$$\mathrm{ILD} = k - m \quad (m < k). \tag{4}$$

Because the ELD and the ILD can be bit-by-bit computed, they are the number 1 states obtained from $S_{out} - S_{in}$ and $\overline{S}_{out} - S_{in}$, respectively. In the case of the -1 state in $S_{out} - S_{in}$ or $\overline{S}_{out} - S_{in}$, the -1 represents a null interconnection. Thus the maximum layer differences in the excitatory and the inhibitory interconnections would be

$$\mathrm{ELD}_{max} = M - 1, \tag{5}$$

$$\mathrm{ILD}_{max} = M - 2. \tag{6}$$

Let ERL and IRL be the redundancy levels of the excitatory and inhibitory interconnections. If ELD ≤ ERL, the corresponding output neurons will be excited. On the other hand, if ELD > ERL, no interconnection will be provided between the input and the output neurons. Similarly, the output neurons will be inhibited for ILD ≤ IRL, and there is no interconnection between the input and the output neurons if ILD > IRL.

An example of redundant interconnection is shown

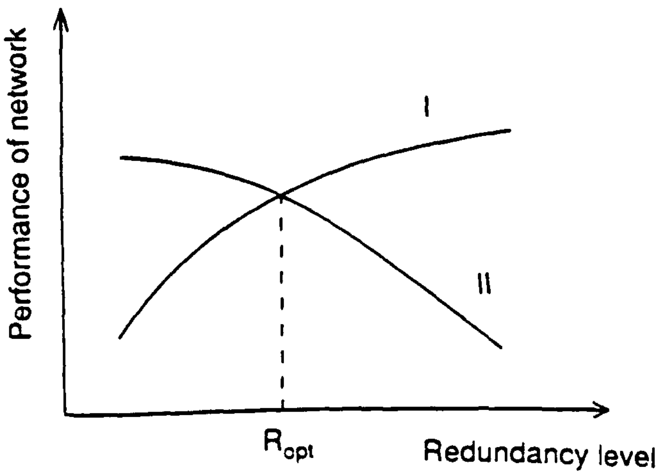

Fig. 2. Hypothical performance of a redundant interconnection. R_{opt}, optimum-redundancy level; I noise tolerance; II, discriminability.

in Fig. 3, in which three binary reference patterns are stored in the memory matrix and each pixel is assumed to equal one neuron. Let us look at the relationship between input neuron 3 and output neuron 1, by which we have $S_1 - S_3 = 0\ 1\ 1$, which implies that ELD = 2. If the ERL is equal to 1, input neuron 3 and output neuron 1 should not be interconnected, as Fig. 3(b) shows. However, if ERL = 2, then there will be an excitatory interconnection (+1) between these two neurons, as shown in Fig. 3(c).

Inhibitory interconnection can be determined in the same manner. For instance, with respect to input neuron 3 and output neuron 4 we have $\bar{S}_4 - S_3 = 0\ 1\ 0$, by which ILD = 1. If we assume that IRL = 0, then these two neurons should not be interconnected, whereas, if IRL = 1, there would be an inhibitory interconnection (−1) from input neuron 3 to output neuron 4, as shown in Fig. 3(c).

Furthermore, when input neuron 1 and output neuron 4 are considered, we have $S_4 - S_1 = -1\ -1\ 0$ and $\bar{S}_4 - S_1 = 0\ 0\ -1$. Because these results yield −1 states, there should be no interconnection among them, as can be seen from Figs. 3(b) and 3(c), respectively.

It is apparent that the IPA logic operation can be easily extended to M reference patterns, by which the subset X,

$$X = P_1P_2 \ldots P_k(\bar{P}_{k+1} + P_{k+2} + \cdots + P_M)$$
$$= P_1P_2 \ldots P_k\bar{P}_{k+1}\bar{P}_{k+2} \ldots \bar{P}_M \quad (1 \le k \le M), \qquad (7)$$

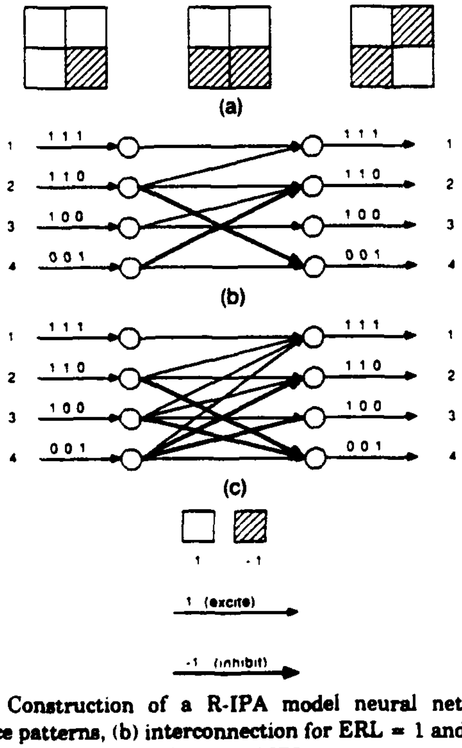

Fig. 3. Construction of a R-IPA model neural network. (a) Reference patterns, (b) interconnection for ERL = 1 and IRL = 0, (c) interconnection for ERL = 2 and IRL = 1.

will excite all the neurons in the following subsets:

$$P_e = P_1P_2 \ldots P_m\bar{P}_{m+1}\bar{P}_{m+2} \ldots \bar{P}_M \quad (m \le k), \qquad (8)$$

and inhibit all neurons in the P_i subsets,

$$P_i = (P_1 + P_2 + \cdots P_n)(P_{n+1}P_{n+2} \cdots P_M)$$
$$= P_1P_2 \cdots \bar{P}_nP_{n+1}\bar{P}_{n+2} \cdots \bar{P}_M \quad (1 \le n \le k). \qquad (9)$$

It is trivial to show that, for ERL = $\mathrm{ERL}_{\max} = M - 1$ and IRL = $\mathrm{IRL}_{\max} = M - 2$, the same result can be derived from the R-IPA algorithm, in which we have proved that the IPA neural network is indeed a maximum-redundant-interconnection network.

IV. Minimum-Redundant Interpattern-Association Model

The logic-operation rule for achieving minimum-redundant IPA interconnection by which the output neurons will be excited by the neurons in the same subset and will be inhibited by the neurons in the opposite subset was discussed in Section III. Because there are no interlayer excitatory and inhibitory interconnections, the network is indeed a minimum-redundancy interconnection network. In other words, the minimum-redundant-interconnection IPA (MR-IPA) model is a special case of the R-IPA model. To verify this fact, we can simply assign a zero redundancy level to the excitatory and inhibitory interconnections, i.e.,

$$\mathrm{ERL} = \mathrm{IRL} = 0. \qquad (10)$$

The minimum-redundancy interconnection weights for M binary patterns (assume that each has N pixels) can be written as

$$T_{ij} = h\left[\sum_{m=1}^{M} P_i(m)P_j(m)\right], \qquad (11)$$

where $h[\cdot]$ is a three-level hard-limiting function, i.e.,

$$h[x] = \begin{cases} 1 & x = M \\ 0, & -M < x < M, \\ -1 & x = -M \end{cases} \qquad (12)$$

As for the Hopfield model, the interconnection weights can be written as[12]

$$T_{ij} = \begin{cases} \sum_{m=1}^{M} P_i(m)P_j(m) & i \ne j \\ 0 & i = j \end{cases}, \qquad (13)$$

where T represents a multivalue memory matrix. For practical implementation, T is clipped into a tristate function, as given by

$$T_{ij} = \begin{cases} g\left[\sum_{m=1}^{M} P_i(m)P_j(m)\right] & i \ne j \\ 0 & i = j \end{cases}, \qquad (14)$$

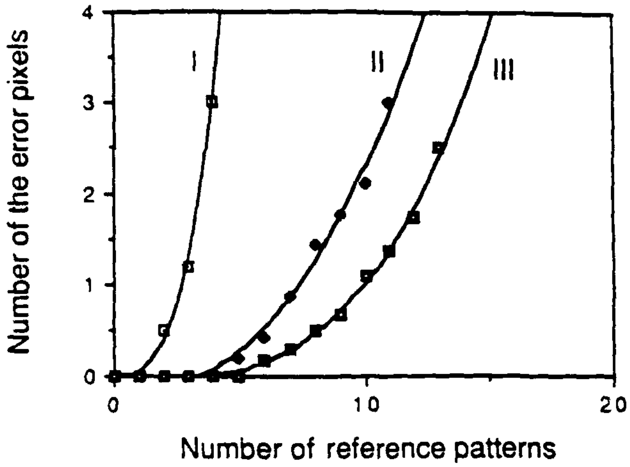

Fig. 4. Performance under 20% noisy inputs: I, Hopfield model; II, IPA model; and III, OR-IPA model [ERL = int(0.3M), IRL = ERL − 1].

Fig. 5. Simulated result with the OR-IPA model.

where

$$g[x] = \begin{cases} 1 & x \geq G \\ 0 & -G < x < G \\ -1, & x \leq -G \end{cases} \qquad (15)$$

We note that for most cases G = 0. We further see that, as G increases, the number of interconnections decreases. It is therefore apparent that the least-interconnection network occurs at $G = M$. Under this condition, Eq. (14) would reduce to Eq. (11), except for the diagonal elements T_{ii}, $i = 1, 2, 3, \ldots N$. Thus we see that the MR-IPA interconnection can be derived from either the R-IPA model or the Hopfield model. In other words, the Hopfield model and the R-IPA model would be the same if all the redundancy interconnections were eliminated. However, the basic distinction between the R-IPA and the Hopfield models must be in the way that redundancy is introduced. In the Hopfield model, the redundancy is introduced based on the information within each of the stored patterns that ignores the interpattern relationship. On the other hand, the redundancy in the R-IPA model is based on the interpattern association among the stored patterns.

We further note that without the redundancy interconnection the MR-IPA neural network would have the lowest input-noise tolerance compared with all the R-IPA models. However, the MR-IPA model possesses the highest discriminability for patterns with similarity. Because the MR-IPA neural net has the least interconnection, it should have the merit of applications to data-reduction assessment, e.g., weather forecasting, earthquake predicting.

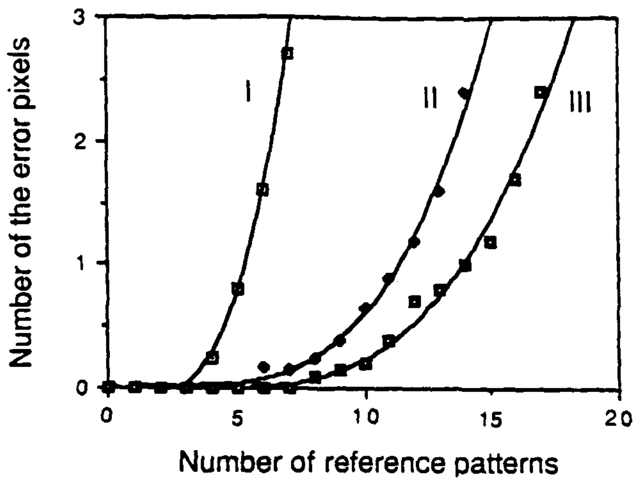

Fig. 6. Performances for partial inputs. I, Hopfield model; II, IPA model; and III, OR-IPA model [ERL = int(0.3M), IRL = ERL − 1].

Fig. 7. Simulated result with the OR-IPA model.

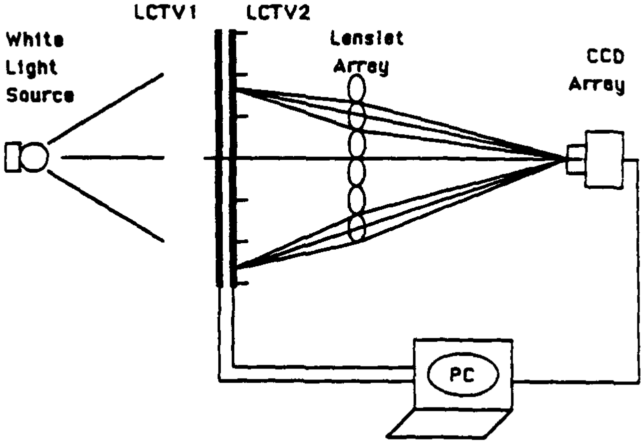

Fig. 8. Optical neural network with cascaded LCTV's; CCD, charge-coupled device; PC, microcomputer.

Simulated and Experimental Results

We first simulated the Hopfield and the R-IPA models using various redundancy levels in an optical neural network. Twenty-six capital Roman letters were used as the training set. If the input pattern is contaminated with 20% noise, the output results show that

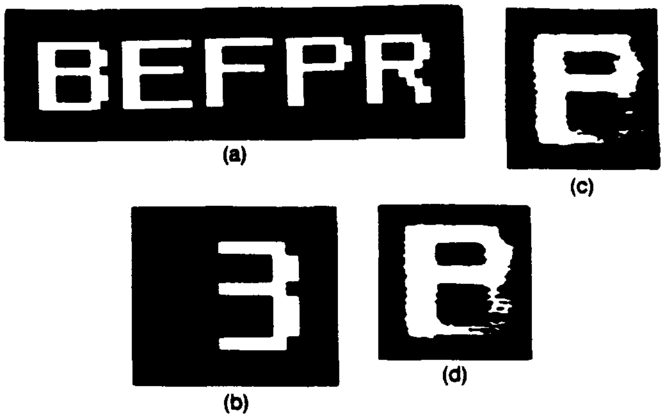

Fig. 9. Experimental results from (a) training sets, (b) partial input, (c) the IPA model, and (d) the OR-IPA model.

the optimum-redundancy (OR) level, R_{opt}, occurs as shown:

$$\mathrm{ERL}_{opt} = \mathrm{int}(0.3M),$$
$$\mathrm{IRL}_{opt} = \mathrm{ERL}_{opt} - 1, \tag{16}$$

where int(·) represents an integer function and M is the number of reference patterns. We stress that the empirical formulas used to estimate optimum redundancy at different noise levels can actually be derived with a larger database simulation.

The error rates, as a function of stored patterns, are also plotted in Fig. 4. We see that the Hopfield, the R-IPA, and the OR-IPA models can sustain 4, 8, and 10 patterns, respectively. Thus the OR interconnection is capable of improving the performance of a neural network under noisy conditions. A simulated result for the OR-IPA model with 10 Roman letters is shown in Fig. 5. The middle row represents the input patterns with a 20% error rate, whereas the bottom row represents the reconstructed output patterns.

Furthermore, performance under partial inputs is also provided. The OR levels are found to be

$$\mathrm{ERL}_{opt} = \mathrm{int}(0.5M),$$
$$\mathrm{IRL}_{opt} = \mathrm{ERL}_{opt} - 1. \tag{17}$$

Once again we see that the OR-IPA model performs better than the Hopfield and the IPA models, as Fig. 6 shows.

Because the R-IPA interconnection weights emphasize the interpattern relationship, the features of the stored patterns play an important role in pattern recognition. It is therefore apparent that the stored patterns should retain this main feature; otherwise erroneous results would be produced. Figure 7 shows a simulated result obtained by using the OR-IPA model. The middle row represents a set of partial input letters that contain the major features. The reconstructed letters are shown in the bottom row, in which 9 of 10 letters can be completely recalled.

Figure 8 shows a cascaded liquid-crystal TV (LCTV) neural network[14,16] that we have used for our experimental demonstrations. Because the interconnection weight matrix and the input pattern vector are displaced in the LCTV's, the emerging light field is proportional to the product of $\mathbf{T}_{lkij}\mathbf{U}_{ij}$ vectors. Notice that these emerging light fields are then incoherently added with a lenslet array imaging onto the charge-coupled device (CCD) camera, and the array of output signals can be thresholded to yield the output result. The output result can also be fed back for the next iteration.

For experimental demonstration, the letters B, E, F, P, and R are used as the training set for which each letter is represented by an 8 × 8 pixel array. Figure 9(b) shows a partial input that contains the main feature of B. The results with the IPA and the OR-IPA models are given in Figs. 9(c) and 9(d), respectively. By comparing these two results, once again we see that the OR-IPA model performs better than the IPA or the Hopfield models.

Conclusions

We have introduced a R-IPA model to improve the performance of the neural network. Although redundant interconnection is more robust, it reduces the discriminability for pattern recognition. Nevertheless, under noisy-input and partial-input situations, the redundant-interconnection network performs better. We have shown that, compared with the Hopfield and the IPA models, the OR-IPA neural network improves the robustness and the pattern discriminability.

We acknowledge the support of the U.S. Army Missile Command through the U.S. Army Research Office under contract DAAL03-87-0147.

References

1. R. P. Lippmann, "An introduction to computing with neural nets," IEEE Trans. Acoust. Speech Signal Process. **ASSP-45**, 4–22 (1987).
2. D. E. Rumelhart and J. L. McClelland, eds., *Parallel Distributed Processing Exploration in the Microstructure of Cognition* (MIT Press, Cambridge, Mass., 1986), Vols. 1 and 2.
3. J. J. Hopfield, "Neural network and physical system with emergent collective computational abilities," Proc. Natl. Acad. Sci. USA **79**, 2554–2558 (1982).

4. J. J. Hopfield and D. W. Tank, "Computing with neural circuits: a model," Science **233**, 625–633 (1986).
5. K. Fukushima, "A neural network for visual pattern recognition," Computer **21**, 65–75 (1988).
6. D. Psaltis and N. H. Farhat, "Optical information processing based on an associative-memory model of neural nets with thresholding and feedback," Opt. Lett. **10**, 98–100 (1985).
7. N. H. Farhat, D. Psaltis, A. Prata, and E. Paek, "Optical implementation of the Hopfield model," Appl. Opt. **24**, 1469–1475 (1985).
8. R. A. Athale and C. W. Stirk, "Compact architectures for adaptive neural nets," Appl. Opt. **28**, 4908–4913 (1989).
9. C. Peterson, S. Redfield, J. D. Keeler, and E. Hartman, "Optoelectronic implementation of multilayer neural networks in a *single* photorefractive crystal," Opt. Eng. **29**, 359–368 (1990).
10. K. Hsu, H. Li, and D. Psaltis, "Holographic implementation of a fully connected neural network," Proc. IEEE **78**, 1637–1645 (1990).
11. C. H. Wang and B. K. Jenkins, "Subtracting incoherent optical neuron model: analysis, experiment, and applications," Appl. Opt. **29**, 2171–2186 (1990).
12. T. Lu, X. Xu, S. Wu, and F. T. S. Yu, "Neural network model using interpattern association," Appl. Opt. **29**, 284–288 (1990).
13. F. T. S. Yu, T. Lu, X. Yang, and D. A. Gregory, "Optical neural network with pocket-sized liquid-crystal televisions," Opt. Lett. **15**, 863–865 (1990).
14. X. Yang, T. Lu, and F. T. S. Yu, "Compact optical neural network using cascaded liquid crystal televisions," Appl. Opt. **29**, 5223–5225 (1990).
15. F. T. S. Yu, X. Yang, and T. Lu, "Space-time-sharing optical neural network," Opt. Lett. **16**, 247–249 (1991).
16. H.-K. Liu and T.-H. Chao, "Liquid crystal television spatial light modulators," Appl. Opt. **28**, 4772–4780 (1989).

APPENDIX 10.10

Polychromatic Neural Net

Optics Communications 88 (1992) 81–86
North-Holland

OPTICS
COMMUNICATIONS

Polychromatic neural networks

Francis T.S. Yu, Xiangyang Yang
Electrical and Computer Engineering Department, The Pennsylvania State University, University Park, PA 16802, USA

and

Don A. Gregory
U.S. Army Missile Command, Redstone Arsenal, AL 35898, USA

Received 28 March 1991; revised manuscript received 7 August 1991

A polychromatic optical neural network using cascaded liquid crystal televisions (LCTV) is presented and simulated which uses a polychromatic interconnection weight matrix (IWM) for color pattern recognition. Extension of the polychromatic neural net for multichannel operation is also proposed.

1. Introduction

Optical implementation of neural networks was initiated by Psaltis and Farhat in 1985 [1,2]. Since then various optical architectures have burgeoned [3–10]. The associative memory interconnection weight matrix (IWM) in those neural nets were either generated by spatial light modulators (SLM) [1–7] or holographic memories [8–10]. It was the parallelism and massive interconnection properties of optics that made it a primary candidate for large scale implementation.

We have recently presented an optical neural network using inexpensive pocket-size liquid crystal televisions (LCTVs) where the IWM was displayed on the LCTV with a microcomputer [4–6]. This LCTV neural network architecture is basically a hybrid optical–digital system where the parallelism and interconnectivity of optics is exploited. Currently available LCTVs are built with color liquid-crystal panels, which makes them particularly suitable for application to color neural nets.

There are two major operations in an artificial neural network (ANN), i.e., the learning phase and the recognition phase. In the learning phase, the interconnection weights among the neurons are decided by the network algorithm, which is implemented by a microcomputer. In the recognition phase, the ANN receives an external pattern and then iterates the interconnective operation until a match with the stored pattern is obtained. The iterative equation for a two-dimensional (2D) ANN is given by

$$U_{lk}(n+1)=f\left(\sum_{i=1}^{N}\sum_{j=1}^{N}T_{lkij}U_{ij}(n)\right), \qquad (1)$$

where U_{lk} and U_{ij} represent the 2D pattern vectors. T_{lkij} is a 4D IWM, f denotes a nonlinear operation, which is usually a sigmoid function for greylevel patterns and a thresholding operator for binary patterns.

2. Polychromatic neural network

A schematic polychromatic neural network is shown in fig. 1 where two LCTVs are tightly cascaded for displaying the input pattern and the IWM, respectively. To avoid the moiré fringes resulting from the LCTVs, a fine layer diffuser (e.g., Scotch tape) is inserted between them. To match the physical size of the IWM, the input pattern can be enlarged so the input pattern pixel is the same size as the submatrix of the IWM. This is illustrated in fig.

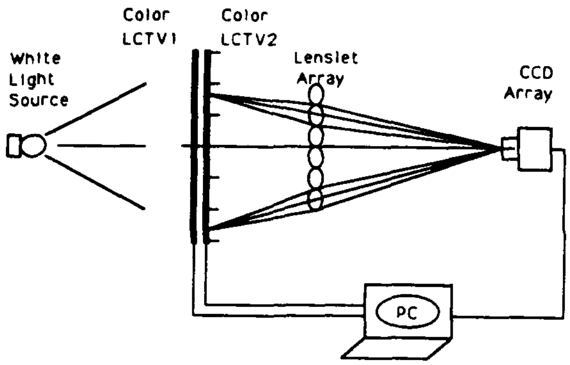

Fig. 1. Schematic diagram of the polychromatic neural network using cascaded color LCTVs.

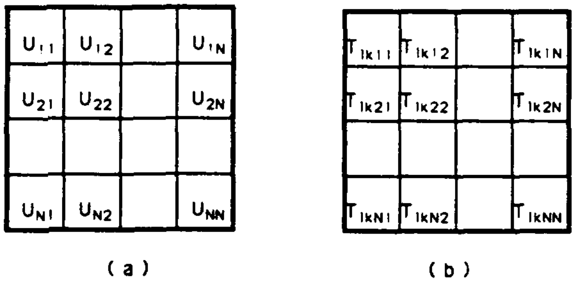

Fig. 2. Display formats for the input pattern and the IWM. (a) Input pattern, (b) IWM.

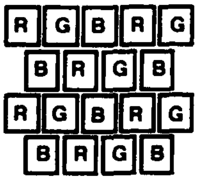

Fig. 3. Pixel structure of the color LCTV.

2. The summation of the input pattern pixels with the IWM submatrices can be obtained with a lenslet array by imaging the transmitted submatrices on the CCD array detector. By properly thresholding the array of detected signals, they can be fed back to LCTV1 for the next iteration.

The liquid crystal panels often used are the Hitachi C5-LC1 color LCTVS. The color pixel distribution is depicted in fig. 3. Every third neighboring RGB pixel element is normally addressed as one pattern pixel (called a triad). Although each pixel element transmits primary colors, a wide spectral content can be produced within each triad [11]. If we denote the light intensity of the pixel element within a triad as $I_R(x, y)$, $I_G(x, y)$ and $I_B(x, y)$, then the color image intensity produced by the LCTV is

$$I(x, y)=I_R(x, y)+I_G(x, y)+I_B(x, y)\ , \qquad (2)$$

where (x, y) represents the spatial coordinates of the liquid crystal panel.

A block diagram of the polychromatic neural network algorithm is illustrated in fig. 4. A set of reference color patterns is stored in the neural network, then each pattern is decomposed into three primary color patterns as the basic training set. For the learning phase, three primary color IWMs (i.e., IWM_R, IWM_G, and IWM_B) should be independently constructed allowing a multicolor IWM to be displayed on LCTV2. If a color pattern is fed into LCTV1, the

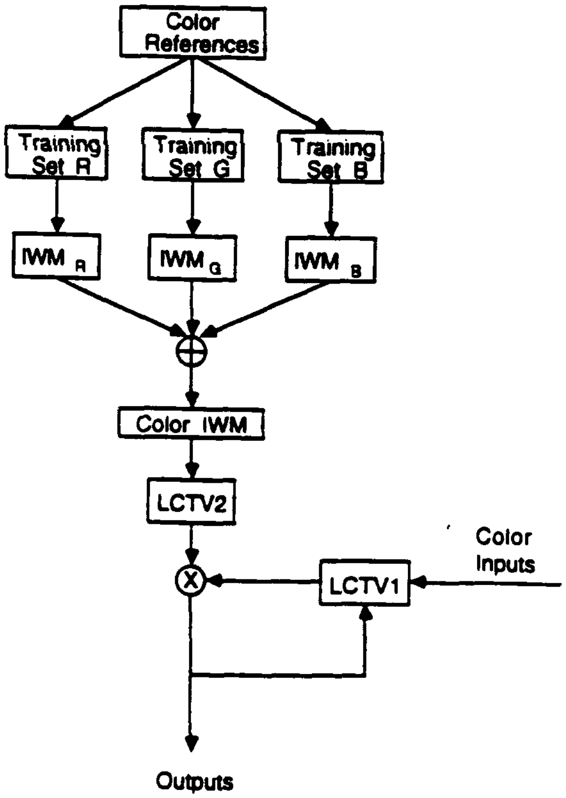

Fig. 4. Block diagram of the polychromatic neural network algorithm.

interative equation of the color neural net should be

$$U_{lk}(n+1)=f\Big(\sum_{i=1}^{N}\sum_{j=1}^{N}\{[T_{lkij}]_{\mathrm{R}}\,[U_{ij}(n)]_{\mathrm{R}} + [T_{lkij}]_{\mathrm{G}}\,[U_{ij}(n)]_{\mathrm{G}}+[T_{lkij}]_{\mathrm{B}}\,[U_{ij}(n)]_{\mathrm{B}}\}\Big). \quad (3)$$

It is then possible to reconstruct (i.e., recognize) the color pattern after some iterations.

We shall now demonstrate the operation of the color neural net through computer simulation where a set of 8×8 triad polychromatic reference patterns in fig. 5a is used as the training set. We used the interpattern association (IPA) algorithm [12,13] for the construction of the polychromatic IWM. The positive and the negative parts are shown in figs. 5b,c, respectively. To illustrate the recognition phase of the neural net, a partial pattern of fig. 5d is applied to the input LCTV1. A fully recovered color pattern shown in fig. 5e is reconstructed, with only one it-

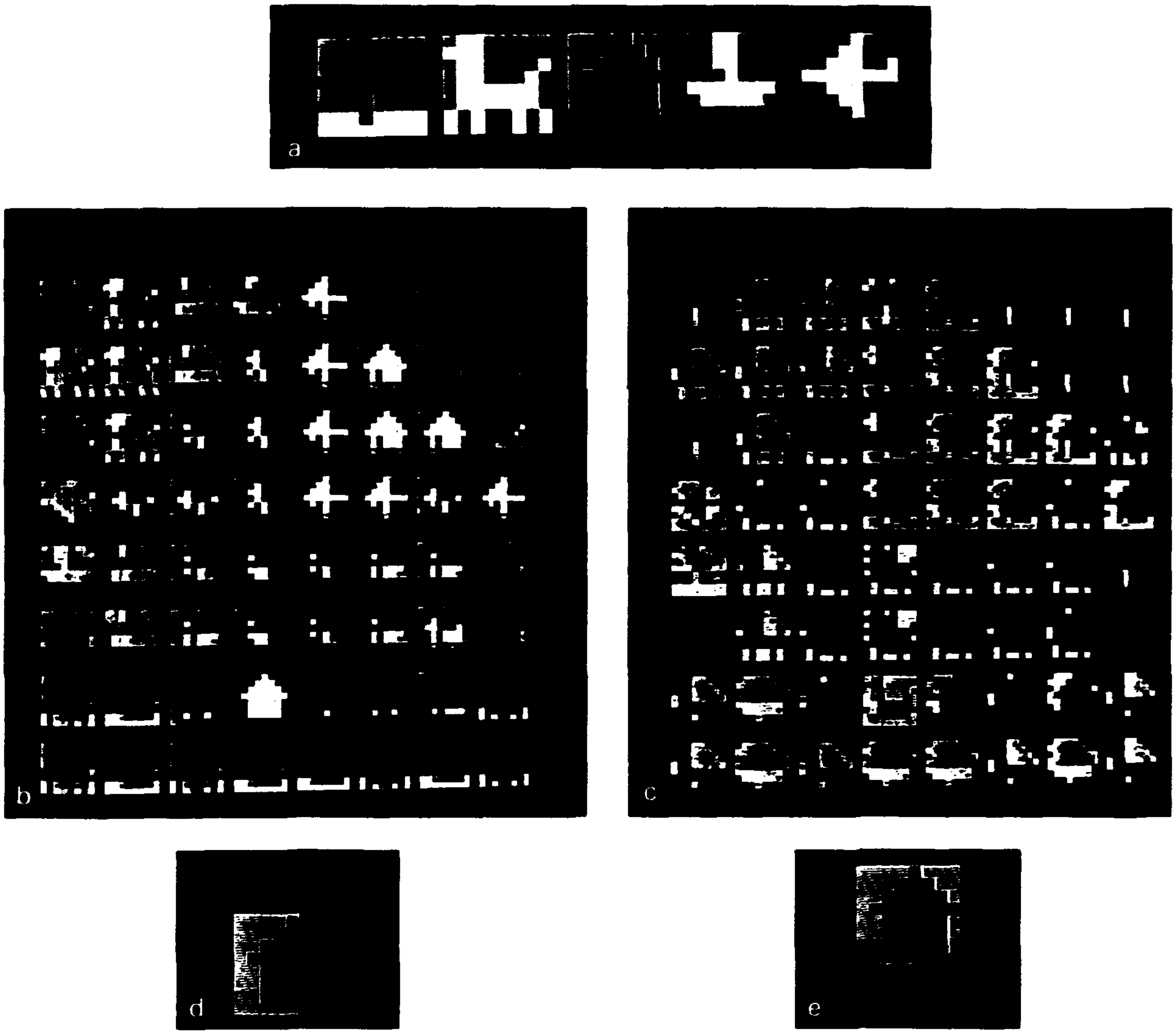

Fig. 5. Autoassociative memory for color patterns. (a) Reference patterns, (b) positive part of the IWM, (c) negative part of the IWM, (d) a partial input pattern, (e) reconstructed output pattern.

eration. From this simulated result, we see that the proposed neural net should indeed be capable of exploiting the spectral content of the pattern.

3. Multichannel neural net

Since each triad of the LCTV consists of three RGB

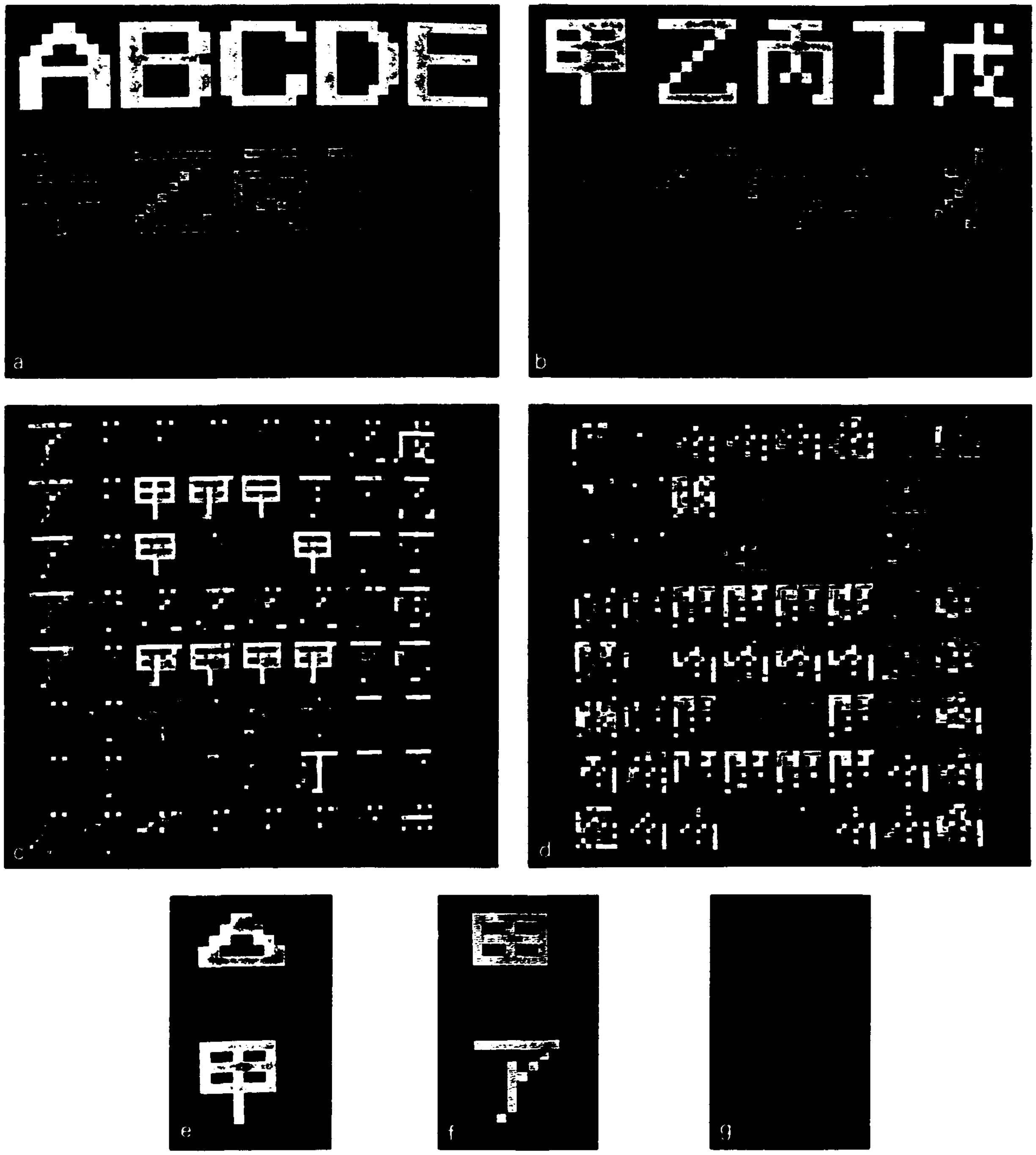

Fig. 6. Character translations. (a) Input training sets, (b) output training sets, (c) positive part of the IWM, (d) negative part of the IWM, (e), (f) and (g) partial inputs and the corresponding translated outputs.

pixel elements, the storage capacity of the polychromatic neural net can be increased three times. For example, three disjoint sets of black-and-white training patterns can be encoded into the RGB primary colors. The $(\mathrm{IWM})_R$, $(\mathrm{IWM})_G$, and $(\mathrm{IWM})_B$ are constructed by each set of training patterns. It is apparent that if a pattern belongs to any of the training sets, only the precise primary color IWM would effectively respond to the input pattern. In other words, the neurons of the encoded $(\mathrm{IWM})_R$, $(\mathrm{IWM})_G$, and $(\mathrm{IWM})_B$ will be properly connected to produce a matching pattern originally encoded in one of the primary colors. By thresholding the output signals detected by the CCD array detector, i.e.,

$$[U'_{lk}(n+1)]_S = f\left(\sum_{i=1}^{N}\sum_{j=1}^{N}\{[T_{lkij}]_S\,[U'_{ij}(n)]_S\}\right),\quad \text{for } S=\mathrm{R},\mathrm{G},\mathrm{B}\,, \tag{4}$$

a recalled (i.e., recognition) pattern with a specific primary color is reproduced.

To demonstrate the implementation of the multi channel neural net, we extend the IPA model to hetero associative memory for exhibiting conversions from one set of functions to another, in our example, alphabet translation. The input–output training sets are given in figs. 6a, b, respectively. The real input English letters (upper row) will translate into red Chinese characteres, the green color Chinese characteres (second row) will translate into green Japanese Katakanas, and the blue color Japanese Katakanas (third row) will translate into blue English letters. Applying the heteroassociation model [14], the positive and the negative parts of the multichannel IWM are shown in figs. 6c, d, respectively. If a partial pattern of A is fed to the neural net, a translated Chinese character in red is produced as shown in fig. 6e. Similarly, a partial pattern of a Chinese character translates to a green color Japanese Katakana, and a partial Katakana translates back to English letters as shown in figs. 6g, f. Thus we see that the polychromatic LCTV neural net can probably be extended to multichannel operation.

4. Experimental demonstration

The experimental demonstration of the wavelength multiplexed multichannel neural net has been conducted. The same input–output training sets are used in the experiment for which the polychromatic IWM is shown in fig. 6. When a red color A is represented to the neural net, the translated Chinese character is produced, as shown in fig. 7a. Similarly, when a blue color Japanese Katakana is fed into the neural net, a blue color A is transmitted as shown in fig. 7b. There is, however, some degree of color crosstalk among the channels as observed in the experiments. The crosstalk is caused by the leakage of the LCTV pixels, the misalignment of the system and the mismatch between the quasi triangular (RGB) pixel structure and the square shape of IWM submatrices. Further efforts will be made, in our subsequent research, to alleviate and eventually eliminate the crosstalk.

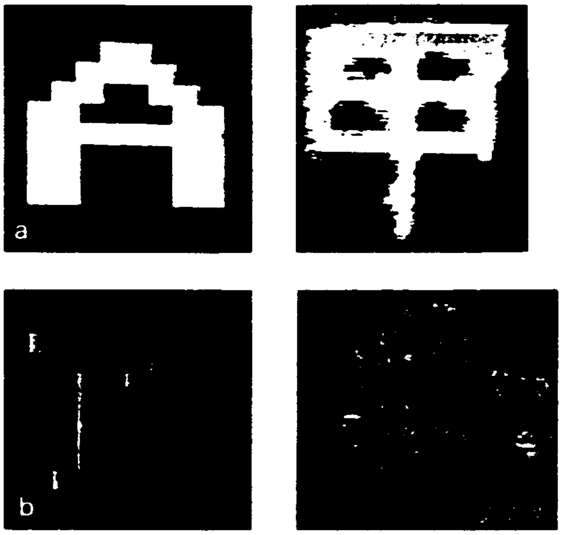

Fig. 7. Experimental results. (a) Translation using red channel. (b) translation using blue channel.

5. Conclusion

We have presented a polychromatic optical neural network simulation using models of cascaded LCTVs. This allows the spectral content of the patterns to be exploited. Since the training set can be decomposed into primary colors, the polychromatic IWM can be synthesized by simply combining the primary color

IWMs of the training set. Computer simulated and experimental results show that a color neural net can most likely be constructed using color LCTVs. Furthermore, using the RGB pixel elements of the LCTVs, multichannel neural net operations should also be possible.

Acknowledgements

We acknowledge the support of the U.S. Army Missile Command through the U.S. Army Research Office under contract DAALO3-87-0147.

References

[1] D. Psaltis and N.H. Farhat, Optics Lett. 10 (1985) 98.

[2] N.H. Farhat, D. Psaltis, A. Prata and E. Peak, Appl. Optics 24 (1985) 1469.

[3] R.A. Athale and C.W. Stirk, Opt. Eng. 28 (1989) 447.

[4] T. Lu, S. Wu, X. Xu and F.T.S. Yu, Appl. Optics 28 (1989) 4908.

[5] F.T.S. Yu, T. Lu, X. Yang and D.A. Gregory, Optics Lett. 15 (1990) 863.

[6] X. Yang, T. Lu and F.T.S. Yu, Appl. Optics 29 (1990) 5223.

[7] T. Lu, F.T.S. Yu and D.A. Gregory, Opt. Eng. 29 (1990) 1107.

[8] C. Peterson, S. Redfield, J.D. Keeler and E. Hartman, Opt. Eng. 29 (1990) 359.

[9] C.H. Wang and B.K. Jenkins, Appl. Optics 29 (1990) 2171.

[10] K. Hsu, H. Li and D. Psaltis, Proc. IEEE 78 (1990) 1637.

[11] R.C. Gonzalez and P. Wintz, Digital image processing (Addison-Wesley, Reading, 1987) p. 190.

[12] T. Lu, X. Su, S. Wu and F.T.S. Yu, Appl. Optics 29 (1[illegible] 284.

[13] X. Yang, T. Lu and F.T.S. Yu, Appl. Optics (to be published).

[14] F.T.S. Yu, T. Lu and X. Yang, Int. J. Opt. Comput. (to be published.

APPENDIX 10.11

Optical Implementation of Hamming Net

a reprint from Applied Optics

Optical implementation of the Hamming net

Xiangyang Yang and Francis T. S. Yu

We present an optical implementation of the Hamming net that can be used as an optimum image classifier or an associative memory. We introduce a modified Hamming net, in which the dynamic range requirement of the spatial light modulator can be relaxed and the number of iteration cycles in the second layer (or maxnet) can be reduced. Experimental demonstrations of the optical implementation of the Hamming net are also given.

I. Introduction

In recent years there has been increasing interest in the optical implementation of artificial neural networks. A number of optical neural network architectures have been proposed and demonstrated.[1–13] The Hopfield model and the Perceptron are the most frequently used neural network models in these optical implementations. The Hopfield model is a fully interconnected network that requires interconnection weights in amounts that equal the square of the pixel number of the input patterns. For example, if a group of 32 × 32 pixel patterns are stored there will be more than one million interconnections in the Hopfield network. The capability of optics for implementing such a huge interconnection is limited by the low resolution of the currently available spatial light modulators (SLM's). Although a space–time sharing scheme may alleviate this limitation[13] it reduces the processing speed significantly. Furthermore the number of stored patterns in the Hopfield network is severely limited. In addition, if a great number of patterns are stored in the neural net it would produce spurious results in the form of a no-match pattern.[14] Even though the Perceptron is trained by the error-back-propagation algorithm, it needs a long training time and requires precise detection of the analog output signals; this is not strong optical use.

Since the Hamming net does not suffer from these limitations[14,15] it would work like an optimum image classifier. The output is generated by selecting the class (or exemplar) that has the minimum Hamming distance with respect to the input pattern. The Hamming distance is defined as the number of bits of the input pattern that does not match the exemplar. The number of interconnections in a Hamming net is proportional to the number of input pixels and the number of exemplars, and it uses fewer interconnections than the Hopfield model. Referring to the above *10 32 × 32 pixel stored exemplars, we find* that the Hamming net requires about ten thousand interconnections, instead of one million, as for Hopfield model. Since the output is selected from the stored exemplars the Hamming net would not produce any spurious or no-match results. In fact, the Hamming net is a K-nearest-neighbor network. In comparison with the Perceptron, the Hamming net can be rapidly trained[16] and does not need precise analog detection at the output domain during the training process.

Because of all these features the Hamming net is particularly suitable for large-scale optical implementation. Here we present a modified Hamming net model that reduces the dynamic range requirement of the SLM's. The optical implementation of the modified Hamming net is presented and the experimental demonstrations are given.

II. Hamming Net Model

A Hamming net is essentially a two-layer neural network, as shown in Fig. 1, that can be used as a maximum-likelihood image classifier.[14] The first layer is known as the Hamming layer and calculates the Hamming distances between the input pattern and each exemplar (i.e., each class), whereas the second layer is known as maxnet, or winner take all, and selects the maximum output node.[17–19]

Let M be the number of the bipolar exemplars

When the research was performed the authors were with the Department of Electrical and Computer Engineering, Pennsylvania State University, University Park, Pennsylvania 16802. X. Yang is now with Quantex Corporation, 2 Research Court, Rockville, Maryland 20850.

Received 6 November 1990

0003-6935/92/203999-05$05.00/0.

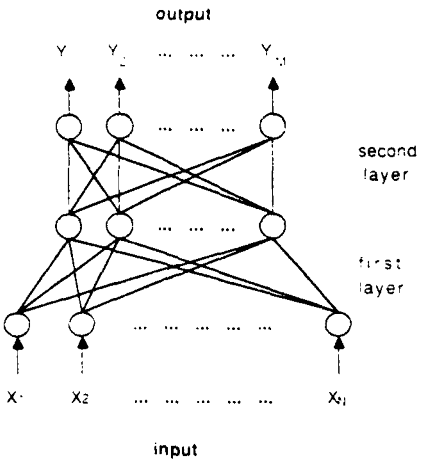

Fig. 1. Hamming net.

stored in the neural network, for which each exemplar has N pixels. The first layer (i.e., the Hamming layer) has N input and M output neurons corresponding to N pixels and M classes, respectively. The interconnection weights in the first layer are determined by

$$W_{ij} = \frac{X_i^{(j)}}{2} \quad (1 \leq i \leq N, \quad 1 \leq j \leq M), \tag{1}$$

where W_{ij} is the interconnection weight from ith input neuron to the jth output neuron, and $X_i^{(j)}$ (which can be either $+1$ or -1) is the value of the ith pixel in the jth exemplar. The threshold value can be set as

$$\theta_j = \frac{N}{2} \quad (1 \leq j \leq M). \tag{2}$$

Thus, when an unknown input pattern is presented at the input, the output of the first layer is given by

$$U_j(0) = \sum_{i=1}^{N} (W_{ij}X_i) + \theta_j \quad (1 \leq j \leq M). \tag{3}$$

When an exemplar matches the input exactly, the output of the neuron representing that exemplar will reach the maximum value N. In contrast, when all the pixels in an exemplar are different from the corresponding pixels of the input pattern, the output of the neuron representing the exemplar will be zero. In general, the output $U_j(0)$ has a value between 0 and N, which is equal to the number of bits of the input pattern that match the bits of the jth exemplar, i.e.,

$$U_j(0) = N - \mathrm{HD} \quad (1 \leq j \leq M), \tag{4}$$

where HD is the Hamming distance.

Although the Hamming net is theoretically sound, the second layer requires a high dynamic range and successive iterations for producing a maximum output node. However, if the Hamming distance between an exemplar and the input pattern is larger than a certain value, (e.g., $N/2$, which is more than half of the different bits), it is not necessary to send a nonzero signal to the second layer. By referring to this argument, we develop a modified Hamming net model below.

Let us introduce a parameter α $(0 < \alpha < 1)$ such that αN is the maximum Hamming distance that gives rise to a nonzero output signal from the first layer. The modified interconnection weights in the Hamming layer can be written as

$$W_{ij} = \frac{X_i^{(j)}}{2\alpha} \quad (1 \leq i \leq N, \quad 1 \leq j \leq M), \tag{5}$$

for which the threshold value is set at

$$\theta_j = N\left(1 - \frac{1}{2\alpha}\right) \quad (1 \leq j \leq M). \tag{6}$$

The output of the Hamming layer therefore can be expressed as

$$\begin{aligned} U_j(0) &= f\left(\sum_{i=1}^{N} W_{ij}X_i + \theta_j\right) \\ &= \begin{cases} N - \dfrac{\mathrm{HD}}{\alpha} & \text{when } \mathrm{HD} < \alpha N \\ 0 & \text{otherwise} \end{cases} \\ &(1 \leq j \leq M), \end{aligned} \tag{7}$$

where $f(\cdot)$ is a thresholding function that is defined as

$$f(x) = \begin{cases} 1 & X > 0 \\ 0 & X \leq 0 \end{cases}. \tag{8}$$

By using the proposed scheme, the Hamming distance between the input and an exemplar can be enlarged by a factor of $1/\alpha$ such that the dynamic range requirement of the SLM's and the number of iterative cycles in the maxnet can be reduced. Thus the overall performance of the modified Hamming net can be improved.

However, in practice, parameter α cannot be small. It should be larger than the input noise tolerance of the network, otherwise the Hamming layer would produce a zero output at the matching neuron. In our experiment, we set $\alpha = 0.5$ in order to adapt to the dynamic range of a practical SLM in which we assume that the input noise is ~20%. In this case, the interconnection weights of the Hamming layer are given by

$$W_{ij} = X_i^{(j)}, \tag{9}$$

the threshold level is

$$\theta_j = 0. \tag{10}$$

and the output of the Hamming layer is

$$U_j(0) = f\left(\sum_{i=1}^{N} W_{ij}X_i\right) = \begin{cases} N - 2\mathrm{HD} & \mathrm{HD} < \dfrac{N}{2} \\ 0 & \text{otherwise} \end{cases} . \qquad (11)$$

Since the maxnet or winner-take-all layer has M input and M output neurons, the interconnection weight between the jth input and kth output neurons can be written as

$$t_{jk} = \begin{cases} 1, & j = k \\ -\epsilon, & j = k \end{cases} \quad \left\{\epsilon < \frac{1}{M}, \quad 1 \leq j, \quad k \leq M\right\}, \qquad (12)$$

where ϵ is known as the inhibition constant.

If the output signal of the Hamming layer is fed to the maxnet layer, iterations can be carried out, as given by

$$\begin{aligned} U_k(n+1) &= g\left[\sum_{j=1}^{M} t_{jk}U_j(n)\right] \\ &= g\left[U_k(n) - \epsilon \sum_{j \neq k} U_j(n)\right] \quad (1 \leq j, k \leq M), \end{aligned} \qquad (13)$$

where $g(\cdot)$ is a nonlinear operator, which assumes a sigmoid function that represents the input–output transfer characteristic of the CCD detector.

By successive iterations of the maxnet, one of the output nodes would have a higher intensity value while all the other nodes eventually go to zero. It has been proven that the maxnet will always converge if $\epsilon < (1/M)$ (see Ref. 15). Thus a maximum output node can always be found. As a K-nearest-neighbor classifier, the Hamming net gives rise to only the best match among all the stored exemplars. However, the selected match exemplar may not be the same as the input pattern. In other words, if the input pattern does not belong to one of the training exemplars, the output will be one of the exemplar that has the least Hamming distance with respect to the input.

Furthermore the Hamming net can also be used as an associative memory, if the exemplar can be represented at the output of the maxnet instead of using the intensity value.

III. Optical Implementation

Figure 2 shows a schematic diagram of an adaptive optical neural network for a Hamming net implementation. The detailed design of the system can be found in one of our recent publications.[10] In brief, an 80-W xenon arc lamp is used as the light source. The interconnection weight matrix (IWM) is partitioned into an array of submatrices and is displayed on a liquid-crystal television panel (LCTV1). A diffuser is placed in front of the LCTV1 such that each pixel can be treated as a secondary source. The input pattern is displayed on the LCTV2, and the lenslet array is used to establish the optical interconnection between the LCTV1 and the LCTV2. In other words, the submatrices of the LCTV1 will be angularly multiplexed onto the LCTV2. From Fig. 2 we see that the light beam emerging from each of the IWM submatrices will be superimposed onto the input pattern. An imaging lens (with a 100-mm diameter and a 75-mm focal length) is used for focusing at the lenslet array and imaging onto the CCD camera, for which the array of output signals can be detected. These array of signals are then thresholded, and they can be fed back to LCTV2 for the next iteration.

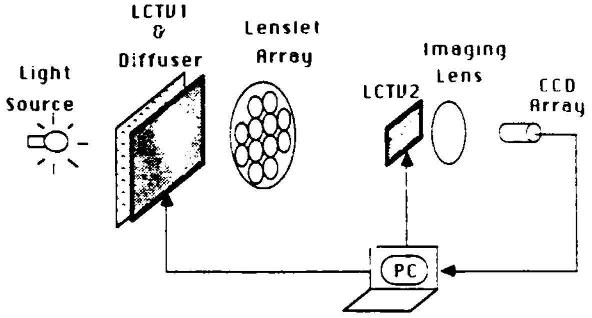

Fig. 2. Hybrid optical Hamming net. The output signal is fed back for a multilayer operation.

For demonstrations, we use 12 8 × 8 pixel exemplars for the experiments. Since the number of submatrices in the IWM equals the number of the stored exemplars, a circular lenslet array that comprises 12 plano–convex lenses (with 6-mm diameters and 72-mm focal lengths) sandwiched by two pieces of optical flat glass is used, as shown in Fig. 3. This circular lenslet array is, in fact, matched with the aperture of the imaging lens so that the primary aberration can be minimized.

In Section II we noted that the IWM is a bipolar matrix in the first layer of the Hamming net. To realize the bipolar multiplication in the optical system, the IWM can be area modulated before being displayed on the LCTV1. As illustrated in Fig. 4, each pixel can be divided into the upper and the lower parts. For example, the value +1 can be encoded with transparent and opaque regions, as shown in Fig. 4(a), for a positive IWM. Similarly, the value −1 can be encoded, as shown in Fig. 4(b), for a negative IWM.

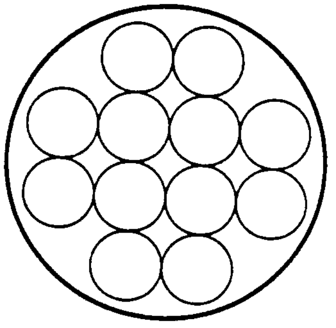

Fig. 3. Circular lenslet array.

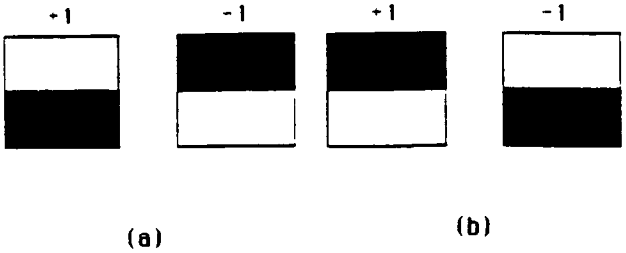

Fig. 4. Area-modulation-encoded IWM in the Hamming layer: (a) transparent and opaque encoding for +1 and −1 in the positive IWM. (b) encoded pixel in the negative IWM.

Needless to say, this input pattern can be encoded in the same manner as the positive IWM. Let us assume that an encoded input pattern is fed to the LCTV2, and encoded positive and negative IWM's are sequentially displayed on the LCTV1; output intensities representing the positive part and the negative part results would then be sequentially collected by the CCD detector. These two sets of signals are then sent to the microcomputer for subtraction and thresholding. This array of thresholded signals can be fed back to the LCTV2 for the maxnet (i.e., the second-layer) operation.

Figure 5(a) shows a set of 8 × 8 pixel English letters that are used as the exemplars in the Hamming net. The positive and negative encoded parts of the IWM are shown in the Figs. 5(b) and (c), respectively, in which the IWM's are partitioned into 12 submatrices and each submatrix is represented by an 8 × 8 pixel array.

Since the number of input and output neurons in the maxnet are equal to the number of the exemplars, the IWM for the maxnet is partitioned into 12 submatrices and each submatrix contains 12 pixels. Area modulation again can be used to encode the bipolar IWM. As illustrated in Fig. 6(a), the transparent pixel represents the value +1 in the positive IWM, whereas the pixel of the value $-\epsilon = -1/16$ has only 1/16 of the transmitted area in the negative IWM. The encoded positive and negative IWM's are shown in Figs. 6(b) and 6(c), respectively.

We stress that the modified Hamming net increases the Hamming distance at the input of the maxnet, which can relax the dynamic range requirement of the SLM and reduce the iteration cycles for the maxnet. The sigmoid function representing the input–output transfer characteristic of the CCD detector would further reduce the number of iterative cycles. Since the dynamic range of the input signal to the maxnet is rather large, low-intensity signals would be suppressed by the CCD detector. We further note that the iteration cycles for a conventional maxnet algorithm require ~10 cycles (see Ref. 12), whereas the use of this proposed hybrid optical system takes only 2–3 iterations.

IV. Experimental Demonstrations

Demonstrations of the optical Hamming net are illustrated in Fig. 7, in which Figs. 7(a) and 7(e) represent two English letter examplars A and H embedded in 20% random noise. The encoded patterns are depicted in Figs. 7(b) and 7(f). The output from the first layer are shown in Figs. 7(c) and 7(g). Figure 7(d) shows the output result of A from the maxnet after 2 iterations, while Fig. 7(h) represents the output of H after 3 iterations. We refer to these results with respect to the exemplars shown in Fig. 5(a) to show that the Hamming net can be used for pattern classification. Compared with the Hopfield model that uses the same optical architecture[9,10] the Hopfield model becomes unstable when storing more

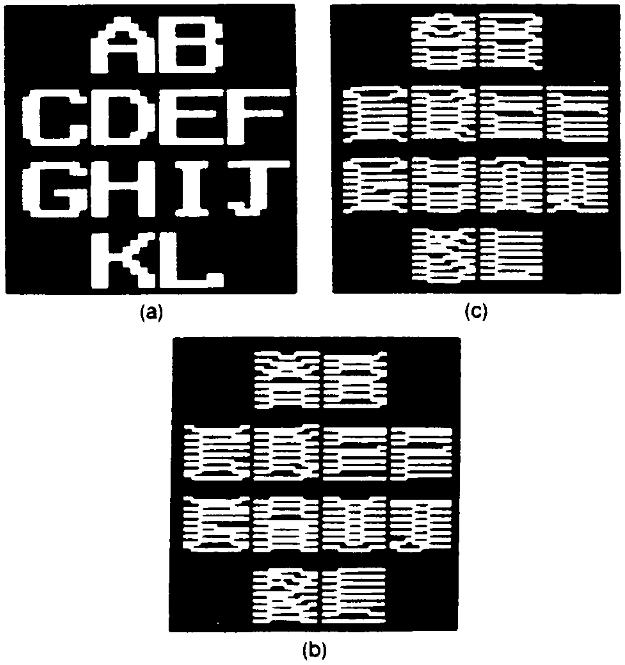

(a) (c)

(b)

Fig. 5. Exemplar set and encoded IWM's in the Hamming layer: (a) 12 exemplars, (b) encoded positive IWM, and (c) encoded negative IWM.

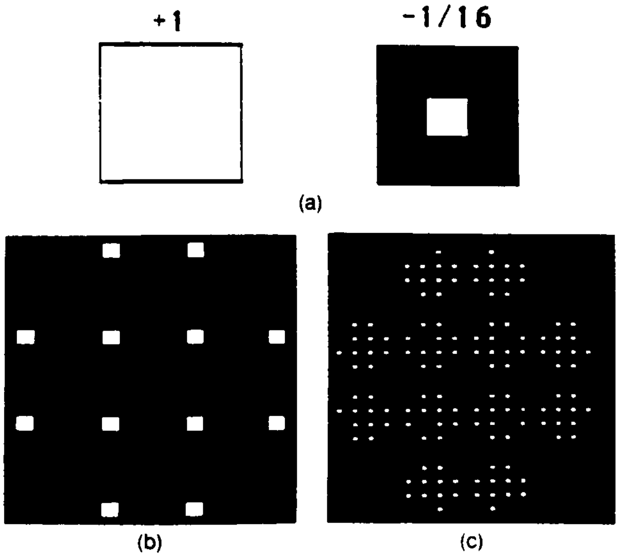

(a)

(b) (c)

Fig. 6. Encoded IWM's in the maxnet: (a) pixel encoding for +1 and −1/16, (b) encoded positive IWM, and (c) encoded negative IWM.

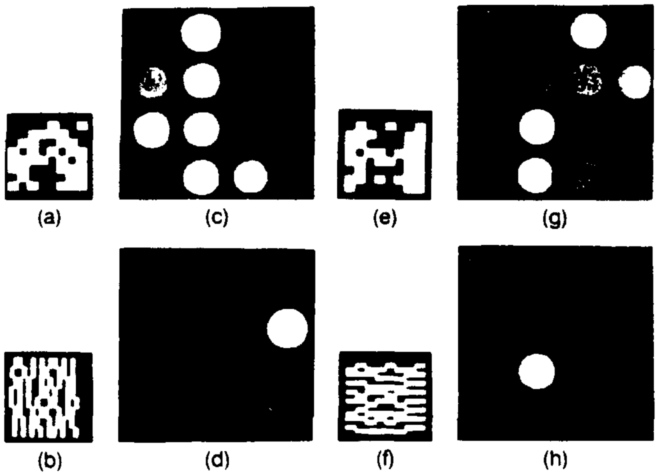

Fig. 7. Experimental demonstrations: (a), (e) Input patterns embedded in 20% random noise; (b), (f) encoded input patterns; (c), (g) outputs from the first layer; (d), (h) output results obtained from maxnet after two iterations for A and three iterations for H, respectively.

than four examplars. In these experimental demonstrations we show that the optical Hamming net has a larger processing capacity compared with the Hopfield net.

We further note that the converged result from the maxnet can also be used to recall the corresponding exemplar. If this recalled exemplar is displayed on an SLM as a final result, the Hamming net obviously can be used as an associative memory. We also note that the maxnet used in the optical unsupervised learning model[11] is carried out primarily with a computer, whereas the maxnet in the optical Hamming net is partially carried out by optics.

V. Conclusion

We have shown that the Hamming net requires fewer interconnections than the fully interconnected Hopfield neural net. As a K-nearest-neighbor neural network model the Hamming net can be rapidly trained, which requires no analog detection during the training process. These features make Hamming net particularly suitable for large-scale optical implementation. We have also shown that the optical Hamming net can be used as a pattern classifier or an associative memory, if the convergent result is used to recall the examplar. One of the important aspects of the modified Hamming net is enlarging the Hamming distance of the output patterns at the first layer. This modification relaxes the dynamic range requirement of the SLM's and also reduces the number of iteration cycles in the maxnet. In order to realize the bipolar nature of the IWM the area-modulation scheme is utilized. Experimental demonstrations have shown that optical implementation of Hamming net has a larger processing capacity compared with the optical Hopfield net.

We acknowledge the support of the U.S. Army Missile Command through the U.S. Army Research Office under contract DAAL03-87-0147.

References

1. D. Psaltis and N. H. Farhat, "Optical information processing based on an associative-memory model of neural nets with thresholding and feedback," Opt. Lett. **10,** 98–100 (1985).
2. N. H. Farhat, D. Psaltis, A. Drata, and E. Paek, "Optical implementation of the Hopfield model," Appl. Opt. **24,** 1459–1475 (1985).
3. N. H. Farhat and D. Psaltis, "Optical implementation of associative memory based on models of neural networks," in *Optical Signal Processing,* J. L. Horner, ed. (Academic, New York, 1987), pp. 129–162.
4. R. A. Athale and C. W. Stirk, "Compact architecture for adaptive neural net," Opt. Eng. **28,** 447–455 (1989).
5. G. J. Dunning, Y. Owechko, and B. H. Soffer, "Hybrid optoelectronic neural networks using a mutually pumped phase-conjugate mirror," Opt. Lett. **16,** 928–930 (1991).
6. L. Zhang, M. G. Robinson, and K. M Johnson, "Optical implementation of a second-order neural network," Opt. Lett. **16,** 45–47 (1991).
7. C.-H. Wang and B. K. Jenkens, "Subtracting incoherent optical neuron model: analysis, experiments, and applications," Appl. Opt. **29,** 2171–2186 (1990).
8. J. Hong, S. Campbell, and P. Yeh, "Optical pattern classifier with perceptron learning," Appl. Opt. **29,** 3019–3025 (1990).
9. T. Lu, S. Wu, X. Xu, and F. T. S. Yu, "Two-dimensional programmable optical neural network," Appl. Opt. **28,** 4908–4913 (1989).
10. F. T. S. Yu, T. Lu, X. Yang, and D. A. Gregory, "Optical neural network with pocket size liquid-crystal televisions," Opt. Lett. **15,** 863–865 (1990).
11. T. Lu, F. T. S. Yu, and D. A. Gregory, "Self-organizing optical neural network for unsupervised learning," Opt. Eng. **29,** 1107–1113 (1990).
12. X. Yang, T. Lu, and F. T. S. Yu, "Compact optical neural network using cascaded liquid-crystal televisions," Appl. Opt. **29,** 5223–5225 (1990).
13. F. T. S. Yu, X. Yang, and T. Lu, "Space-time sharing optical neural network," Opt. Lett. **16,** 247–249 (1991).
14. R. P. Lippmann, "Introduction to computing with neural nets," IEEE Trans. Acoust. Speech Signal Process. **4,** 4–12 (1987).
15. R. P. Lippmann, B. Gold, and M. L. Malpass, "A comparison of Hamming and Hopfield neural nets for pattern classification," Tech. Rep. TR. 769 (MIT Lincoln Laboratory, Cambridge, Mass., 1987).
16. R. P. Lippmann, "Pattern classification using neural networks," IEEE Trans. Commun. **27,** 47–64 (1989).
17. P. Lazzaro, M. Ryckebusch, and C. Mead, "Winner take all networks of O(n) complexity," Tech. Rep. CALTECH-CS-TR-21-88 (California Institute of Technology, Pasadena, Calif., 1988)
18. X. Yang, W. Seidermann, R. A. Athale, and M. Astor, "Optical Winner-Take-All neural network based on electron trapping materials," in *Image Storage and Retrieval Systems,* A. A. Jamberdino and W. Niblack, eds., Proc. Soc. Photo-Opt Instrum. Eng. **1662** (to be published).
19. S. Grossberg, "Studies of mind and brain neural principles of learning, perception, development, cognition and motor control," in *Boston Studies in Philosophy of Science,* S. Grossberg ed. (Reidel, Dordrecht, The Netherlands, 1982), Chap 8.

APPENDIX 10.12

Optical Novelty Filter

Optics Communications 92 (1992) 205–208
North-Holland

OPTICS
COMMUNICATIONS

Optical novelty filter with phase carrier

Francis T.S. Yu, Shudong Wu, Sumati Rajan, Andy Mayers
Department of Electrical and Computer Engineering, The Pennsylvania State University, University Park, PA 16802, USA

and

Don A. Gregory
U.S. Army Missile Command, Redstone Arsenal, AL 35898, USA

Received 28 August 1991; revised manuscript received 13 April 1992

The use of a phase carrier to perform novelty filtering is proposed and experimentally demonstrated.

In this Communication, we present a novelty filter implementation using a photorefractive BSO crystal in a four-wave mixing architecture in conjunction with an object phase carrier modulation. The four-wave mixing technique is advantageous as it does not require a high intensity laser. The novelty filter is simple to implement since it is recorded in the Fourier plane. In addition, a phase carrier modulation is used to separate the higher orders of the object spectrum from the noisy dc component. Using this modification, the output noise can be suppressed and the moving object observed at the output plane. System analysis and experimental verification will be provided.

Techniques for using photorefractive crystals for novelty filtering in two-wave mixing [1], beam fanning [2], and four-wave mixing [3,4] architectures have recently been suggested by several investigators. The two-wave mixing method uses the depletion of the object beam by the reference beam to construct the novelty filter. For an object moving at speeds higher than the response time of the photorefractive crystal, depletion of the object beam is not achieved. Thus, the moving object will be displayed at the output plane of the system. This method requires a high intensity laser beam to obtain the necessary depletion and has been shown to suffer from a low response time. The beam fanning technique is also based on the depletion of the object beam. In this method, the depletion is due to the fanout of the object beam, thus eliminating the need for a reference beam. However, this method suffers from the same drawbacks as the two-wave mixing.

The four-wave mixing interferometric method uses a phase conjugate mirror to generate two phase conjugate beams which form a two-arm interferometer. In principle, the phase distortion in the interferometer due to any stationary object will be compensated by the phase conjugation and hence, only moving objects will be displayed at the output of the interferometer. However, because of the nonuniformity of the photorefractive material, no phase distortion can be completely compensated by phase conjugation. In addition, the nonuniform intensity distribution of the incident light may also produce phase distortion in conjugated beams. Also, in practice, it is rather difficult to construct a two-arm phase conjugate interferometric configuration and extremely difficult to obtain a null output field from the interferometer.

In this Communication we present a novelty filter implementation using a four-wave mixing architecture with an additional phase carrier modulation. Since the filter is located in the Fourier plane, this configuration is easier to implement than the previous interferometric techniques and due to the focusing of the energy, requires lower laser power. In an ideal four-wave mixing set up, a phase object will be compensated by the phase conjugate beam, and only a dc component will be reconstructed by the filter. Thus a high pass filter blocking the dc term at the Fourier plane, will result in a null output for a stationary object. However, if the object is in motion, the high frequency component from the moving object will be observed at the output plane. The low frequency contents of the moving object, as well as its dc component are blocked by the high pass filter. To overcome this problem, a phase carrier grating is added to the input signal to shift the spectrum of the moving object away from the origin and the dc components. For a stationary object, the phase grating formed by the object at the crystal will be compensated by the phase beam and a constant field is obtained at the output of the interferometer. This can be blocked by a dc filter at the Fourier plane, resulting in a null output signal. For a moving object however, the phase grating will not be completely compensated and the resulting modulated spectrum will not be eliminated by the dc filter. Thus by using one of the higher diffraction orders, the moving object can be observed at the output plane.

Two implementations of the phase carrier modulation will be discussed in this Communication. In the first method, we assume that a phase object is moving in front of a stationary phase grating. Let $\Phi_0(x, y, t)$ be the moving phase object, where (x, y) are the spatial coordinates at the input plane. Then the light field exiting the object phase grating pair is given by

$$A_0 = \exp[\mathrm{i}\Phi_0(x, y; t)\sin(2\pi f_0 x)]\,, \tag{1}$$

where f_0 is the carrier frequency of the phase grating. Thus the corresponding phase conjugate beam derived from the phase conjugate mirror arriving at the object plane, is given by

$$A_c = \exp[-\mathrm{i}\Phi_c(x, y; t)\sin(2\pi f_0 x)]\,, \tag{2a}$$

where Φ_c is the conjugated phase distribution due to four-wave mixing. For a stationary object, there is no time dependence, and the beam from the phase conjugate mirror is ideally the conjugate of the object beam, and hence

$$A_c = kA_0^*\,, \tag{2b}$$

where k is a proportionality constant. For a nonstationary object, moving faster than the response time of the crystal, the conjugate beam cannot compensate for the object beam. We model this inability to compensate for the motion as a time delay, Δt, on the conjugate beam,

$$\begin{aligned}\Phi_c(x, y, t) &= \Phi_0^*(x, y, t-\Delta t)\\ &= -\Phi_0(x, y, t-\Delta t)\end{aligned} \tag{2c}$$

The time difference Δt consists of two terms, the first being the path difference between the conjugate beam and the object beam, which is extremely small, and the second being the time delay that is observed between the conjugate beam and the object beam due to the finite response time of the crystal.

Thus, for a nonstationary object, the phase conjugate beam passes through the object again, and the beam exiting the input plane can then be written as

$$\begin{aligned}B = \exp\{\mathrm{i}[\Phi_0(x, y; t)\\ - \Phi_0(x, y; t-\Delta t)]\sin(2\pi f_0 x)\}\end{aligned} \tag{3}$$

If we assume that the phase carrier frequency f_0 is much higher than the bandwidth of the object, then, using the Jacobi–Anger formula, eq. (3) can be expressed as

$$B \approx \sum_{m=-\infty}^{m=+\infty} J_m(\Delta\Phi(x, y; t))\exp(\mathrm{i}2\pi m f_0 x)\,, \tag{4}$$

where $\Delta\Phi(x, y; t) = \Phi_0(x, y; t) - \Phi_0(x, y; t-\Delta t)$. From this result we see that each diffraction order contains the $\Delta\Phi(x, y; t)$ distribution. Notice that when $\Delta\Phi(x, y; t) = 0$, i.e. for a stationary object, the dc component is the only nonzero term in eq. (4). Therefore, by blocking all but one of the diffraction orders, a null output is expected.

For the second implementation, we assume that the phase carrier modulation is superimposed on the object and that they are moving at a constant velocity v. The output light field can be written as

$$\begin{aligned}B = \exp\{\mathrm{i}[\Phi_0(x-vt, y, t)\sin[2\pi f_0(x-vt)]\\ - \Phi_0(x, y, t)]\sin(2\pi f_0 x)\}\,.\end{aligned} \tag{5}$$

By assuming that the carrier frequency is much greater than the bandwidth of the object, eq. (5) can be written as

$$B \approx \sum_m \{J_m[\Phi_0(x-vt,y,t)\cos[2\pi f_0(x-vt)] - \Phi_0(x,y,t)] - \mathrm{i}J_m[\Phi_0(x-vt,y,t) \times \sin(2\pi f_0 vt)]\}\exp(\mathrm{i}2\pi m f_0 x) \,. \tag{6}$$

Thus the average intensity for the mth order term would be

$$I_m \approx \langle J_m^2[\Phi(x-vt,y)\cos(2\pi f_0 vt) - \Phi(x,y)]\rangle + \langle J_m^2[\Phi(x-vt,y)\sin(2\pi f_0 vt)]\rangle \,, \tag{7}$$

where $\langle\ \rangle$ denotes the ensemble time average. Thus we see that each of the diffraction orders contains the information content of the moving object. Furthermore for $v=0$, i.e. a stationary object, $I_m=0$ (except for the zeroth order). Therefore, by imaging one of the higher diffraction orders, the moving object can be observed.

For the experimental demonstration, we used the configuration shown in fig. 1. An argon laser beam is divided into three beams, A, B, and C using two beam splitters. A BSO crystal biased with a 6 kV/cm transverse electric field is used as a phase conjugate mirror. Beams B and C serve as the pump beams. Beam A illuminates the input object and is transformed by the Fourier transform lens L_1 onto the crystal. A phase conjugate beam (shown by broken lines in fig. 1), is generated by the crystal, and passes through the object transparency. The resultant output light field is imaged by lens L_2 onto the CCD camera in which a small aperture is incorporated to select the specific diffraction order. The input object encoded with a grating structure is shown in fig. 2, where the grating frequency f_0 is approximately 4 lines/mm. The phase carrier encoded object was obtained using a conventional bleaching process.

The spectrum of a stationary object at the Fourier plane is shown in fig. 3a. The high diffraction orders appear very weak. This demonstrates that the input phase object (with the phase grating) was compensated by the phase conjugation. However, as the ob-

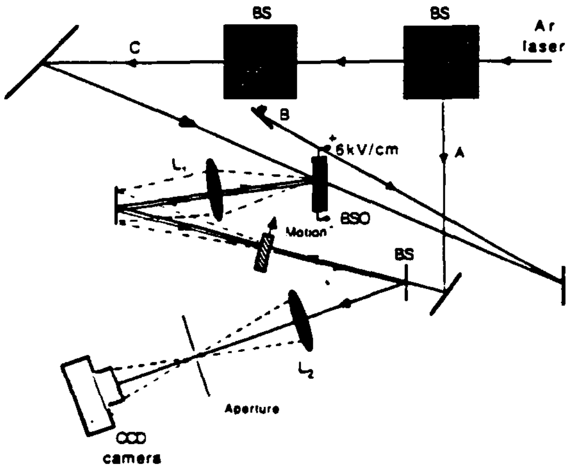

Fig. 1. Experimental setup for novelty filtering with phase carrier frequency.

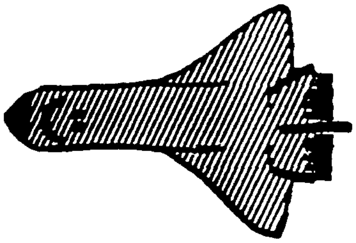

Fig. 2. The phase carrier frequency encoded object.

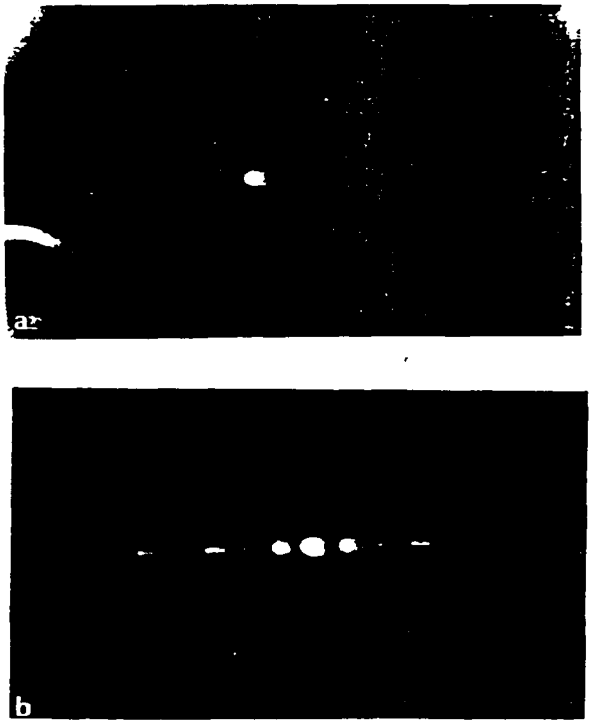

Fig. 3. The spectral distribution of the novelty filter, (a) for a stationary object and (b) for a moving object.

ject moves, the high diffraction orders appear much brighter as shown in fig. 3b. If one of the upper or lower non-zero diffraction orders is selected, the output image of the moving object can be captured by the CCD camera. Figure 4a shows the resulting output image obtained of the moving phase object. From this result, we have shown that a moving object can be reconstructed at the output plane.

The frequency of the phase carrier is mainly limited by the nonuniformity of the photorefractive crystal. The use of the transform lens L_1 minimizes the effect of the nonuniformity of the crystal, since only a small conical region within the crystal is used. In our experiments the crystal thickness is 10 mm, and a carrier frequency of up to 10 lines/mm were used. For gratings of higher frequency, the phase compensation can not be fully accomplished resulting in residual high diffraction orders of the spectrum which can be seem in fig. 3a.

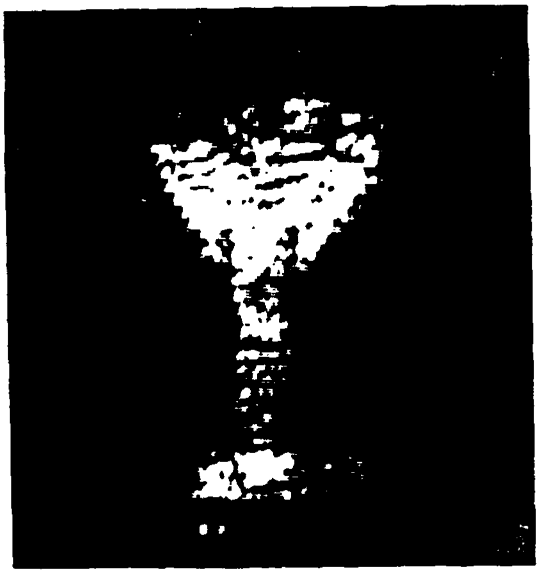

Fig. 4. The output image distributions using the filter for a moving object.

In summary we have implemented a novelty filter using a four-wave mixing architecture which employs a photorefractive BSO crystal and a phase carrier modulation. Due to the use of this architecture, the configuration has a lower laser power requirement than the two-wave mixing and beam fanning techniques. In addition, fast response speeds can be achieved using the BSO crystal. To reduce the effects of the output noise of the system, a phase carrier was used enabling movement in the input scene to be detected. Using an encoded carrier frequency, this technique can be used for tracking a moving object.

We acknowledge the support of the U.S. Army Missile Command through the U.S. Army Research Office under contract DAAL03-91-0112.

References

[1] M. Cronin-Golomb, A.M. Brenacki, C. Lin and H. Kong, Optics Lett. 12 (1987) 1029.
[2] J.E. Ford, Y. Fainman and S.H. Lee, Optics Lett. 13 (1988) 1856.
[3] D.Z. Anderson, D.M. Liniger and J. Feinberg, Optics Lett. 12 (1987) 123.
[4] D.Z. Anderson and J. Feinberg, IEEE J. Quantum Electron. 25 (1989) 635.

APPENDIX 10.13

PR Compact JTC

a reprint from Applied Optics

Compact joint transform correlator with a thick photorefractive crystal

Francis T. S. Yu, Shundong Wu, Sumati Rajan, and Don A. Gregory

D. A. Gregory is with the U.S. Army Missile Command, Redstone Arsenal, Alabama 35898. The other authors are with the Department of Electrical Engineering, Pennsylvania State University, University Park, Pennsylvania 16802.

Received 26 June 1991.
0003-6935/92/142416-03$05.00/0.

A compact joint transform correlator with a thick photorefractive crystal is presented. We demonstrate that Bragg diffraction severely limits the correlation performance in a thick crystal. To relax the Bragg limitation of the crystal a Galilean telescopic beam compression technique is used in the joint transform correlator.

The ability to process a large quantity of information at high speed makes the optical correlator an attractive candidate for applications to machine vision, target tracking, object detection, etc. Although conceptually simple, the VanderLugt correlator,[1] which employs a holographic spatial filtering technique, has inherent filter synthesis and alignment problems that prevent its widespread practical application. On the other hand the joint transform correlator (JTC)[2,3] is a simple and practical processor that overcomes these two major disadvantages. Since photorefractive materials can be continuously updated for processing they are good candidates for real-time operations.[4-6] Unlike spatial light modulators (SLM's) some photorefractive materials have very high spatial resolution (of the order of 7000 lines/mm) and have a sensitivity approaching that of photographic film.

Using a photorefractive crystal to construct a spatial filter is similar to recording a volume hologram. The readout process of a crystal hologram is severely limited by Bragg diffraction.[7] Since the angular selectivity of the photorefractive crystal increases with the thickness of the crystal, we discuss a two-beam compression technique for alleviating the Bragg diffraction limitation.

Let us begin with a general expression for Bragg diffraction:

$$\mathbf{G} = \mathbf{k}_0 - \mathbf{k}_1, \quad (1)$$

where $\mathbf{G}$ represents the grating vector within the crystal and $\mathbf{k}_0$ and $\mathbf{k}_1$ are wave vectors of the writing beams.

If the recorded hologram is read out by vector $\mathbf{k}_2$, as shown in Fig. 1, and the scattered wave vector is denoted by $\mathbf{k}_3$, then the phase difference (PD) of the light that is scattered from two points within the crystal can be written as

$$\mathrm{PD} = \mathbf{G} \cdot \mathbf{r} - (\mathbf{k}_2 - \mathbf{k}_3) \cdot \mathbf{r}, \quad (2)$$

where $\mathbf{r}$ denotes the displacement vector between the two points. From Eqs. (1) and (2) we obtain

$$\mathrm{PD} = \Delta\mathbf{k} \cdot \mathbf{r}, \quad (3)$$

where

$$\Delta\mathbf{k} = (\mathbf{k}_0 - \mathbf{k}_1 - \mathbf{k}_2 + \mathbf{k}_3) \quad (4)$$

is known as the dephasing vector.

The normalized intensity of scattered light from the entire volume of the crystal can be expressed as

$$I(\mathbf{k}_3) = \left| \int_v \exp(j\Delta\mathbf{k} \cdot \mathbf{r}) dv \right|^2 . \quad (5)$$

This expression is valid only under weak diffraction conditions in which the multiple diffractions within the crystal are considered negligible. With reference to a JTC with a photorefractive crystal, shown in Fig. 2, the wave vectors $\mathbf{k}_0$, $\mathbf{k}_1$, and $\mathbf{k}_3$ can be expressed as

$$\mathbf{k}_0 = -\frac{x_0}{\lambda}\mathbf{u} + \frac{\eta}{\lambda}\left(1 - \frac{{x_0}^2}{2\eta^2}\right)\mathbf{z}, \quad (6)$$

$$\mathbf{k}_1 = -\frac{x_1}{\lambda}\mathbf{u} + \frac{\eta}{\lambda}\left(1 - \frac{{x_1}^2}{2\eta^2}\right)\mathbf{z}, \quad (7)$$

$$\mathbf{k}_3 = -\frac{x_3}{\lambda}\mathbf{u} + \frac{\eta}{\lambda}\left(1 - \frac{{x_3}^2}{2\eta^2}\right)\mathbf{z}, \quad (8)$$

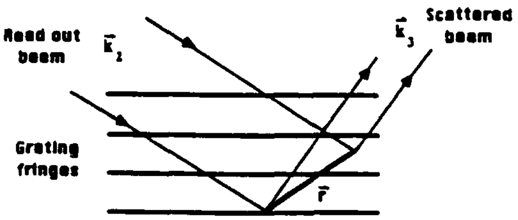

Fig. 1. Bragg diffraction in a thick photorefractive crystal.

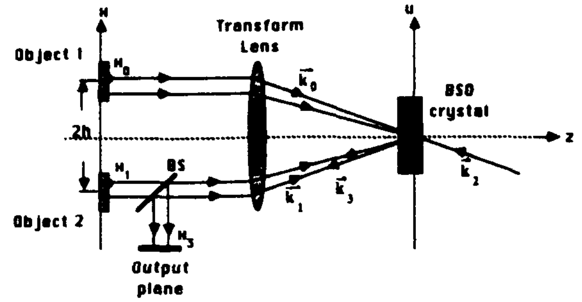

Fig. 2. JTC with a BSO crystal. BS, beam splitter.

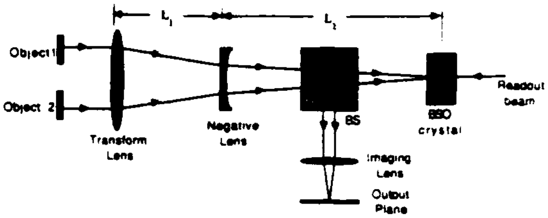

Fig. 3. Two-dimensional beam compression technique with a Galilean telescope.

where x_0, x_1, and x_3 are normalized coordinates of objects 1 and 2 and the output plane, respectively, η represents the refractive index of the crystal, and λ is the wavelength of the light source. The normalized coordinates x_0, x_1, and x_3 are obtained by dividing the respective coordinates by the focal length of the transform lens system f. If the crystal hologram is read out by the $\mathbf{k}_2$ vector, the output correlation intensity can be calculated by

$$I(x_3) = \left| \iiiint q_0{}^*(x_0 - h) q_1(x_1 + h) \exp(j\Delta\mathbf{k}\cdot\mathbf{r})\mathrm{d}x_0 \mathrm{d}x_1 \mathrm{d}u \mathrm{d}z \right|^2, \quad (9)$$

where q_0 and q_1 are the object functions and (u, z) represents the coordinate system of the crystal. The separation of objects $2h$ is normalized in the same manner as coordinates x_0, x_1, and x_3.

For simplicity we assume that the crystal is infinitely extended in the transverse direction. The resulting Bragg diffraction condition of the crystal in the transverse direction is $(\Delta\boldsymbol{k})_u = 0$. Equation (9) can be reduced to the following form:

$$I(x_3) = \left| \int_{-z/2}^{z/2} q_0(x_0 - h) q_1(x_0 - x_3) \mathrm{sinc}(\pi D \Delta k_z] \mathrm{d}x_0 \right|^2, \quad (10)$$

where

$$\Delta k_z = \frac{(x_0 - h)\,(x_3 - h)}{\eta\lambda}. \quad (11)$$

Thus we see that the output correlation peak is diffracted at x_3 = h. The maximum peak intensity occurs when the object $q_0(x_0)$ and the sinc factor are both centered at $x_0 = h$. In order to obtain a high correlation intensity the width of the sinc factor should be wider than the width of the object. We note that the Bragg diffraction of the crystal severely limits the width of the object and the shift invariance property of the JTC.

In order to alleviate the Bragg diffraction limitation a method that uses beam compression in a JTC is discussed. Since the width of the object and the shifted distance are both normalized by the focal length of the transform lens these values, in effect, represent the angles subtended by the writing beams in the crystal. Thus, by simply reducing these angles, the Bragg diffraction limitation can be relaxed.

In order to achieve a two-dimensional beam compression in a JTC a Galilean telescope can be used as shown in Fig. 3. Note that the use of a Galilean telescope to alleviate low resolution in SLM's has been reported recently by Davis *et al.*[8] For the JTC system shown in Fig. 3 the beam compression ratio is

$$M = \frac{L_2}{f - L_1}. \quad (12)$$

Thus the effective focal length of the JTC is approximately Mf, by which the scale of the object spectrum is enlarged by a factor of M. To preserve the space–bandwidth product of the JTC the transverse size of the crystal should also be increased by a factor of M.

For experimental demonstration a compact JTC with a bismuth silicon oxide (BSO) photorefractive crystal is shown in Fig. 3. The 10-mm-thick BSO crystal is operating under a 6-kV/cm transverse electric field. In our experiments English letters O and X approximately 2.5 mm in size are used as input objects for autocorrelation and cross-correlation operations. The separation between input objects varies from 6 to 17 mm. The crystal holograms are recorded with an Ar$^+$ laser lasing at 488 nm. The output correlation peak is detected by a CCD camera and then digitized for three-dimensional display. The correlation performances of the proposed JTC are plotted in Fig. 4. Figure 4 shows the output autocorrelation peaks obtained from the letter O with increasing separation between the input objects. From these figures we see that the autocorrelation peak decreases as the object separation increases.

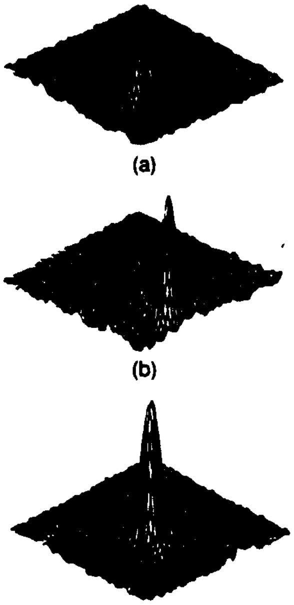

Fig. 4. Output autocorrelation distributions of the letter O with a two-dimensional compression technique for various object separations: (a) $2h$ = 11 mm, (b) $2h$ = 13 mm, (c) $2h$ = 17 mm.

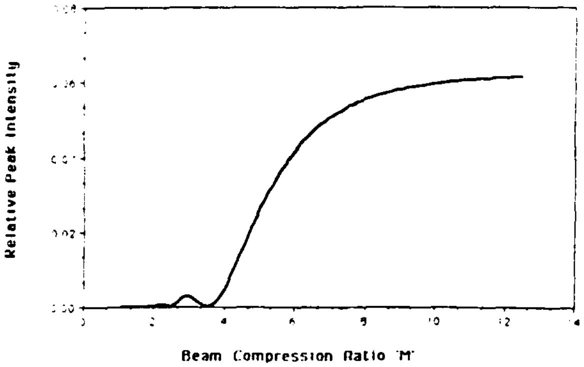

Fig. 5. Variation of the relative peak intensity with the beam compression ratio.

It should also be mentioned that, without the introduction of a negative lens in the JTC, the correlation peaks were not observed. This is due primarily to the Bragg limitations of the crystal. Introducing a negative lens (coupled with a transform lens) forms the well-known Galilean telescope. We have observed that the correlation peaks are greatly enhanced.

In view of Eqs. (10) and (11) the correlation peak intensity occurs when the sinc factor is centered at $x = h$. To compute the correlation peak intensity as a function of M, which is given in Eq. (12), we assume that the focal length of the transform lens $f = 10$ cm, the wavelength of the light source $\lambda = 488$ nm, the input objects are rectangular shapes of ~2.5-mm width separated by a distance of 15 mm, and the refractive index of the BSO crystal is 2.54 with a thickness of 1 cm. The beam compression ratio M represents the magnitude of compression of the angles by the writing beams in the crystal. As these angles are decreased, the Bragg diffraction limitation is relaxed. Hence by increasing the beam compression ratio M the peak intensity should increase. Figure 5 is a plot of the relative peak intensity computed for increasing values of M. From this figure we see that the peak intensity increases rapidly as M increases from 4 to 8 and then saturates for $M > 8$. This indicates that the output correlation performance in a JTC system can be improved beyond the Bragg diffraction limitations of the original system by using this compact object beam compression technique.

In conclusion, we have demonstrated that the Bragg diffraction limitation in a thick photorefractive crystal can be relaxed by using a Galilean telescope in a JTC. However to preserve the space–bandwidth product of the system an increase of the beam compression ratio M requires a larger transverse size of the crystal. Also the increased size of the Fourier spectrum may decrease the light intensity at the crystal and result in slower response times. Nevertheless this beam compression can be used to design a compact real-time JTC with a photorefractive crystal.

We acknowledge the support of the U.S. Army Missile Command through U.S. Army Research Office contract DAAL03-87-K-0147.

References

1. A. B. VanderLugt, "Signal detection by complex spatial filtering," IEEE Trans. Inf. Theory **IT-10**, 139–148 (1964).
2. F. T. S. Yu and X. J. Lu, "A real-time programmable joint transform correlator," Opt. Commun. **52**, 10–16 (1984).
3. F. T. S. Yu and J. E. Ludman, "Microcomputer-based programmable optical correlator for automatic pattern recognition and identification," Opt. Lett. **11**, 395–397 (1986).
4. C. S. Secton and W. H. Steir, "Accuracy of real-time correlations via degenerate optical four-wave mixing," in *Digest of Conference on Lasers and Electro-Optics* Optical Society of America, Washington, D.C., 1983), paper TUB4.
5. B. Loiseaux, G. Illiaquer, and J. P. Huignard, "Dynamic optical cross-correlator using a liquid crystal light valve and a bismuth silicon oxide crystal in the Fourier plane," Opt. Eng. **24**, 144–149 (1985).
6. M. G. Nicholson, I. R. Cooper, M. W. McCall, and C. R. Petts, "Simple computational model of image correlation by four-wave mixing in photorefractive semiconductor materials," Appl. Opt. **26**, 278–285 (1987).
7. G. Gheen and L. J. Cheng, "Optical correlators with fast updating speed using photorefractive semiconductor materials," Appl. Opt. **27**, 2756–2761 (1988).
8. J. A. Davis, M. A. Waring, G. W. Bach, R. A. Lilly, and D. M. Cotrell, "Compact optical correlator design," Appl. Opt. **28**, 10–11 (1989).